

UC San Diego

Research Theses and Dissertations

Title

Nearshore Circulation

Permalink

<https://escholarship.org/uc/item/1jf5k6k8>

Author

Feddersen, Falk

Publication Date

1999

Peer reviewed

INFORMATION TO USERS

This manuscript has been reproduced from the microfilm master. UMI films the text directly from the original or copy submitted. Thus, some thesis and dissertation copies are in typewriter face, while others may be from any type of computer printer.

The quality of this reproduction is dependent upon the quality of the copy submitted. Broken or indistinct print, colored or poor quality illustrations and photographs, print bleedthrough, substandard margins, and improper alignment can adversely affect reproduction.

In the unlikely event that the author did not send UMI a complete manuscript and there are missing pages, these will be noted. Also, if unauthorized copyright material had to be removed, a note will indicate the deletion.

Oversize materials (e.g., maps, drawings, charts) are reproduced by sectioning the original, beginning at the upper left-hand corner and continuing from left to right in equal sections with small overlaps.

Photographs included in the original manuscript have been reproduced xerographically in this copy. Higher quality 6" x 9" black and white photographic prints are available for any photographs or illustrations appearing in this copy for an additional charge. Contact UMI directly to order.

**ProQuest Information and Learning
300 North Zeeb Road, Ann Arbor, MI 48106-1346 USA
800-521-0600**

UMI[®]

UNIVERSITY OF CALIFORNIA, SAN DIEGO

Nearshore Circulation

**A dissertation submitted in partial satisfaction of the
requirements for the degree Doctor of Philosophy
in Oceanography**

by

Falk Feddersen

Committee in charge:

**Professor R. T. Guza, Chairperson
Professor R. E. Davis
Professor L. D. Talley
Professor B. D. Cornuelle
Professor Thomas O'Neil**

1999

UMI Number: 3035923

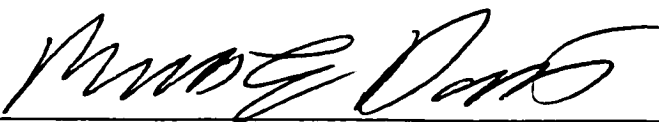
UMI[®]


UMI Microform 3035923


**Copyright 2002 by ProQuest Information and Learning Company.
All rights reserved. This microform edition is protected against
unauthorized copying under Title 17, United States Code.**


**ProQuest Information and Learning Company
300 North Zeeb Road
P.O. Box 1346
Ann Arbor, MI 48106-1346**

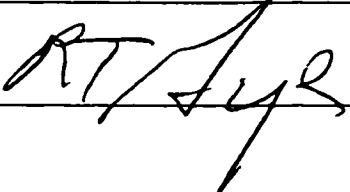
The dissertation of Falk Feddersen is approved, and it is acceptable in quality and form for publication on micro-film:










_____ Chair

University of California, San Diego

1999

TABLE OF CONTENTS

	Signature Page	iii
	Table of Contents	iv
	List of Figures	vi
	List of Tables	x
	Acknowledgements	xi
	Vita, Publications, and Fields of Study	xiii
	Abstract	xv
I	Introduction	1
II	Alongshore Momentum Balances in the Nearshore	9
	A. Abstract	9
	B. Introduction	10
	C. Observations	13
	D. Alongshore Momentum Balances	21
	E. Discussion	30
	F. Summary	32
	G. Appendix A: Barotropic Pressure Gradient Estimates	34
	H. Appendix B: Surf Zone Width (x_b) Estimates	34
	I. Appendix C: Cross-Shore Integration Method	35
	J. References	37
III	Alongshore Bottom Stress Parameterizations	40
	A. Abstract	40
	B. Introduction	41
	C. Bottom Stress Parameterizations	42
	D. Field Observations	47
	E. Parameterizations	49
	1. Linear Parameterization	49
	2. Joint-Gaussian Parameterization	52
	3. Nonlinear Parameterizations	54
	4. Empirical Nonlinear Parameterizations	58
	F. Discussion	60
	G. Conclusions	64
	H. Appendix A. Evaluation of $E[\vec{u} v]$	65
	I. Appendix B. Weak-current Approximations	67

J. Appendix C. Small-Angle Parameterization	70
K. References	72
IV Weakly Nonlinear Shear Waves	75
A. Abstract	75
B. Introduction	76
C. Theory	79
D. Calculations for ANH96 base-state conditions	89
E. Analytic and numerical model comparison	96
F. Discussion and Conclusions	105
G. Appendix A: The Adjoint Operator	107
H. Appendix B: Asymptotics	108
I. References	110
V Numerical Models for Nearshore Circulation: A progress report	112
A. Introduction	112
B. Governing Equations	113
C. The Staggered C-Grid and discretization	113
D. Velocity Boundary Conditions	115
E. Time Stepping and Numerical Stability	116
F. The Pressure Equation	118
G. Relaxing the Rigid Lid	124
H. Future Model Development	124
I. Model Tests	125
1. Rotating Channel Flow	125
2. ANH96 Shear Waves Tests	126
3. Slinn Tests	129
J. References	132

LIST OF FIGURES

I.1	The coordinate system used. Planar beach bathymetry ($h = \beta x$) is shown.	2
II.1	Plan view of the beach at Duck. A solid circle represents a colocated pressure sensor, current meter, and sonar altimeter. The open circles represent the Field Research Facility pressure sensor array. Bathymetry from October 20 is contoured in units of meters below mean sea level. Wind speed was measured about 500 m from the shoreline at alongshore location 500 m.	14
II.2	The cross-shore location of colocated current meters, pressure sensors, and sonar altimeters (triangles); bathymetry observed on August 25 (solid curve) and October 26 (dashed curve). An additional colocated pressure sensor and current meter in 8-m water depth, 750 m from the shoreline, is not shown.	15
II.3	Hourly values of (a) significant wave height H_{sig} and (b) mean incident wave angle [Kuik <i>et al.</i> 1985] in 8-m depth (zero corresponds to normal incidence and positive angles to waves from the northern quadrant). (c) Absolute value of the maximum hourly averaged alongshore current $ \bar{v}_{max} $ and (d) cross-shore location of the bar crest (dashed) and of \bar{v}_{max} . The 572 values of $ \bar{v}_{max} $ shown correspond to hours with at least five active current meters and $ \bar{v}_{max} \geq 0.25$ m/s. The few maxima occurring > 250 m from shore are not shown in Figure 3d.	17
II.4	The radiation stress $-S_{yx}/\rho$ in 8-m depth versus the alongshore current maximum \bar{v}_{max} ($r^2 = 0.76$). An observation is shown only if at least five sensors were active.	19
II.5	(a) Hourly averaged alongshore current \bar{v} versus distance from the shoreline and (b) depth observed at 1300 eastern standard time September 21. Arrows pointing toward the bottom of the figure indicate southward flow.	20
II.6	Hourly integrated (from the shoreline to 8-m depth) wave ($-S_{yx}/\rho _{x_{8m}}$ solid curve) and wind ($\int_0^{x_{8m}} (\tau_y^{wind}/\rho) dx$ dashed curve) forcing versus time. Positive corresponds to northward forcing. The means are -0.0085 and -0.0278 m^3/s^2 , and the standard deviations are 0.1296 and 0.0616 m^3/s^2 for wave and wind forcing, respectively.	23
II.7	Hourly total forcing (wind and wave, $-S_{yx}/\rho _{x_{8m}} + \int_0^{x_{8m}} (\tau_y^{wind}/\rho) dx$ solid curve) and bottom stress ($c_f \int_0^{x_{8m}} < \bar{u} v> dx$ dashed curve) integrated from the shoreline to 8-m depth with a best fit $c_f = 0.0015$ versus time. Gaps occur when the bottom stress integral could not be computed because of inactive sensors. The correlation coefficient squared $r^2 = 0.87$	24

II.8	Hourly total forcing (wind and wave, $-S_{yx}/\rho _{x_{sm}} + \int_0^{x_b} (\tau_y^{wind}/\rho) dx$ solid curve) and bottom stress ($c_{f1} \int_0^{x_b} \langle \vec{u} v \rangle dx$ with $c_{f1} = 0.0035$ dashed curve) integrated over the surf zone versus time. The correlation coefficient squared $r^2 = 0.79$	27
II.9	Hourly wind forcing ($\int_{x_b}^{x_{sm}} (\tau_y^{wind}/\rho) dx$ solid curve) and bottom stress ($c_{f2} \int_{x_b}^{x_{sm}} \langle \vec{u} v \rangle dx$ with $c_{f2} = 0.00055$ dashed curve) integrated seaward of the surf zone versus time. The correlation coefficient squared $r^2 = 0.36$	29
II.10	(a) Significant wave height, (b) alongshore current \bar{v} , and (c) depth versus distance from the shoreline observed at 0500 eastern standard time October 16.	33
III.1	Locations of the 13 Duck94 (x) and 26 SandyDuck (o) current meters used in this study. The U. S. Army Corps of Engineers Field Research Facility (FRF) coordinate system is used. Bathymetry from October 2, 1997 is contoured in units of meters below mean sea level.	48
III.2	(a) Observed $\langle \vec{u} v \rangle$ versus $\sigma_T \bar{v}$. The solid line is the least-squares best-fit (slope $a = 1.62$ and skill $r^2 = 0.94$). (b) Observed $\langle \vec{u} v \rangle$ versus \bar{v} . The solid line is the least-squares best-fit (slope = 0.99 m/s and skill $r^2 = 0.88$). Each panel has 70,099 data points.	50
III.3	Observed $\langle \vec{u} v \rangle / \sigma_T \bar{v}$ versus $ \bar{v} /\sigma_T$. (a) All data points in the region $0 < (\langle \vec{u} v \rangle / \sigma_T \bar{v}) < 4$. (b) The subset of data where $ \langle \vec{u} v \rangle > 0.2 \text{ m}^2/\text{s}^2$ (7857 data points).	51
III.4	(a) Observed $\langle \vec{u} v \rangle$ versus the expected value $E[\vec{u} v]$ assuming a joint-Gaussian velocity field with observed means, variances, and ρ_{uv} . The slope is 1.00, and the skill is $r^2 = 1.00$. (b) The ratio $\langle \vec{u} v \rangle / E[\vec{u} v]$ versus $ \bar{v} /\sigma_T$	53
III.5	The joint-Gaussian based $E[\vec{u} v]/\sigma_T \bar{v}$ versus $ \bar{v} /\sigma_T$. (a) $\bar{u}/\sigma_u = 0$, $\rho_{uv} = 0$, and $\sigma_v/\sigma_u = 0.0$ (solid), 0.35 (dotted), 0.7 (dashed), and 1.0 (dash-dot). (b) $\bar{u} = 0$, $\sigma_v/\sigma_u = 0.41$ (the observed mean value), and $ \rho_{uv} = 0.9$ (dash-dot), 0.45 (dashed), and 0 (solid). (c) $\sigma_v/\sigma_u = 0.41$, $\rho_{uv} = 0$, and $ \bar{u} /\sigma_T = 1.0$ (solid), 0.5 (dashed), and 0 (dash-dot). (d) $\sigma_v/\sigma_u = 0.41$, $\rho_{uv} = 0.5$, and $\bar{u}/\sigma_T = -0.6$ (dashed), -0.3 (dotted), 0.3 (dash-dot), and 0.6 (solid). Note the axes scales of (a) and (c) are different than (b) and (d).	55
III.6	Observed $\langle \vec{u} v \rangle$ versus the closed form small-angle parameterization (III.2) with the observed \bar{v} and σ_T . The best-fit slope is 1.06 and the skill $r^2 = 0.98$. Plots for all the nonlinear parameterizations (sections 4.3 and 4.4) are similar.	56

III.7 Means (\diamond) and standard deviations (vertical bars) of the ratio of the observed to the parameterized $\langle \vec{u} v \rangle$. (a) The joint-Gaussian $E[\vec{u} v]$, (b) TG86 with $\tan(\theta) = \sigma_v/\sigma_u$, (c) TG86 with $\theta = 0$, and (d) closed form small-angle (III.2).	57
III.8 Means (\diamond) and standard deviations (vertical bars) of the ratio of the observed to the parameterized $\langle \vec{u} v \rangle$. (a) WT83 with the weak-current $\alpha(\sigma_v/\sigma_u, \rho_{uv})$, (b) WT83 with the weak-current unidirectional wave $\alpha(\sigma_v/\sigma_u)$, (c) WT83 with the best-fit constant $\alpha = 1.16$, and (d) SL with best-fit constants $a_1 = 0.66$ and $a_2 = 0.87$	59
III.9 The means and standard deviations of the ratio $\langle \vec{u} v \rangle / E_r[\vec{u} v]$ versus $ \vec{v} /\sigma_T$. The observed $\langle \vec{u} v \rangle$ is used, and $E_r[\vec{u} v]$ is based on the observed \bar{u} , \bar{v} , and ρ_{uv} , but with 80% of the observed σ_u and σ_v . The corresponding result using the observed σ_u and σ_v is shown in Figure III.7a.	61
III.10 Alongshore current solutions versus distance from the shoreline with four parameterizations for the bottom stress: weak-current (III.15) (solid), Rayleigh (dotted), WT83 (dash-dot), and SL (dashed). Solutions are shown for different values of the drag coefficient c_f . (a) $c_f = 0.01$, (b) $c_f = 0.001$, and (c) with c_f adjusted to yield the same \bar{v}_{\max} as SL with $c_f = 0.001$. The c_f values for the weak-current, Rayleigh, WT83, and SL parameterizations are 1.66, 2.04, 1.03, and 1.00 (all $\times 10^{-3}$) respectively. The flow is forced by waves (offshore $H_{\text{rms}} = 1$ m, $\theta = 10^\circ$, and peak period $T = 10$ s) that are transformed using <i>Church and Thornton [1993]</i> over the barred bathymetry shown in (d).	63
III.11 Observed $\langle \vec{u} u \rangle$ versus $E[\vec{u} u]$. The skill $r^2 = 0.95$ and $N = 70,099$. The scale is the same as in Figure III.4.	68
IV.1 The coordinate system used. x is the cross-shore coordinate and y is the alongshore coordinate.	80
IV.2 The base state nondimensional longshore current $V(x)$ (IV.33a) and potential vorticity $Q(x)$ (IV.33b).	89
IV.3 Real and imaginary parts of (a) the eigenvalues of (IV.8) at $\alpha_c = 0.201189$ and $k_c = 1.363262549$. (b) The spectrum enlarged to show the region $-0.030 < c_i < 0.005$	91
IV.4 The critical dispersion curve for $\omega_c(k) + i\sigma_c(k) = kc$ near the critical wavenumber k . The circles represent calculated values. The solid lines are the best fit parabolas from the coefficients of Table IV.1. The upper panel and lower panel are the curves for $\sigma_c(k)$ and $\omega_c(k)$ respectively.	94
IV.5 The real (solid) and imaginary (dashed) parts of (a) ϕ_1 , (b) ϕ_1^\dagger , (c) $\phi_2^{(0)}$, (d) $\phi_2^{(1)}$, and (e) $\phi_2^{(2)}$	95

IV.6	Nondimensional spectra of u at $x = 1$ from ANH96 model with $\alpha = 0.17$ (thin line) and 0.18 (bold line).	97
IV.7	(a) The ANH96 model peak amplitude at the primary frequency at $x = 1$ versus ϵ for $\alpha = 0.18$ (*) and $\alpha = 0.17$ (o). The inferred $\alpha_c = 0.18564$. (b) The amplitude of the second harmonic versus ϵ^2 . The inferred $\alpha_c = 0.18741$.	98
IV.8	The ANH96 derived versus the theoretical change in peak frequency between $\alpha = 0.18$ and $\alpha = 0.17$. Results for the primary frequency (*), second (o), third (◊), and fourth (Δ) harmonic are shown with $\alpha_c = 0.20119$. The error bars (± 0.003) indicate the frequency resolution of the spectrum. The solid line represents perfect ANH96 model-theory agreement. The dashed line is the best fit through the symbols.	99
IV.9	(a) $ \phi_1(x) $ versus nondimensional cross-shore coordinate, x . (b) $ \phi_1(x) $ normalized (to a maximum magnitude of 1.0) versus x . (c) The phase of $\phi_1(x)$ versus x . In each panel, theory is a solid line, and ANH96 model $\phi_1(x)$ are inferred with $\alpha_c = 0.20119$, and are shown with $\alpha = 0.18$ (dash-dot) and $\alpha = 0.17$ (dashed). The phases are offset so that they are equal at $x = 0.582$.	101
IV.10(a)	$ \phi_2^{(2)}(x) $ normalized (to the maximum theory magnitude) versus x . (b) The phase of $\phi_2^{(2)}(x)$ versus x . Shown in each panel: theory (solid) and ANH96 model for $\alpha = 0.18$ (dash-dot) and $\alpha = 0.17$ (dashed). The phases are offset so that they are equal at $x = 0.561$.	102
IV.11	The normalized (to have the same maximum magnitude) correction to the mean alongshore current from theory (solid) and ANH96 model for $\alpha = 0.18$ (dash-dot) and $\alpha = 0.17$ (dashed).	104
V.1	The locations of u (\bullet), v (\diamond), and η (\times) on the C-grid. The depth and η points are colocated. The solid line represents a boundary to cross-shore flow. The relative indexing scheme used is shown.	114
V.2	Time series of cross-shore velocities at $x = 90$ m at different values of μ . Compare this with Figure 3 of ANH96.	128
V.3	Time series of u at $x = 90$ m, $\mu = 0.001$, and $L^{(y)} = 1350$ m. Compare to Figure 7, bottom panel of ANH96.	129
V.4	Contour plots of vorticity at $t = 2$, $t = 10$, and $t = 16$ hours. The shoreline is at the bottom of each panel, and the alongshore current is maximum at approximately cross-shore coordinate 90 m.	130
V.5	Vorticity after 8 hours for barred beach bathymetry for the equilibrated shear wave case $\mu = 0.00546$. The region offshore of 160 m is not shown. Compare to Figure 7 first panel of <i>Slinn et al.</i> [1999].	131

LIST OF TABLES

III.1 Statistics of the velocity field and the associated wave directional properties. Positive u and v correspond to onshore and southerly flow, respectively.	47
III.2 Best-fit slopes between the observed $\langle \vec{u} v \rangle$ and the TG86, ED80, and the $E[\vec{u} v]$ with $ \rho_{uv} = 1$ (III.21) parameterizations (all with $\bar{u} = 0$) using three different wave angles. The <i>Kuik et al.</i> [1988] angle is a principal axes angle calculated from the velocity covariance matrix. The $\theta = 0$ entry for the $ \rho_{uv} = 1$ $E[\vec{u} v]$ is the SA (III.2) parameterization (Figure III.6). For all parameterizations the skill $r^2 \geq 0.98$	56
III.3 Statistics of $\alpha(\sigma_v/\sigma_u, \rho_{uv})$ (III.4) and $\alpha(\sigma_v/\sigma_u)$ (III.5) based on the observed σ_v/σ_u and ρ_{uv}	58
IV.1 The quadratic coefficients for the growth rate and frequency, $\omega_c(k) + i\sigma_c(k) = a_2(k - k_c)^2 + a_1(k - k_c) + a_0$ where $k_c = 1.36326254916$. .	90
IV.2 Coefficients for the complex Ginzburg-Landau equation and solution values.	93

ACKNOWLEDGEMENTS

I would like to thank my advisor Bob Guza, who gave me the freedom to blossom, taught me to focus and give attention to detail, and stabilized me when I drifted off course. I appreciate all he has done for me. I would also like to thank my co-authors and colleagues Steve Elgar and Tom Herbers. They also played significant mentoring roles during my time at SIO. I would also like to thank the staff at the Center for Coastal Studies, especially the folks who built, installed, and maintained the many instruments deployed at Duck over the past few years which led to the two excellent data sets used here. Thanks Bill Boyd, Brian Woodward, Kimball Millikan, Kent Smith, Dennis Darnell, Mike Clifton, Steve Gavino, Chuck Worley, Jerry Wanetick, Shannon Scott, Andre Merritt, Ina Hendricks, and Terri Hughes. In addition to their tireless efforts in the field, Bob's elder students Britt Raubenheimer and Edie Gallagher helped me tremendously when I first began working at CCS.

I would also like to thank many folks elsewhere in the nearshore community, Steve Lentz, John Allen, Ed Thornton, Rob Holman, Tony Bowen, John Trowbridge, and many others for their comments and encouragements. I would also like to thank my committee and the physical oceanographic faculty at SIO. My first year of graduate school was both challenging and inspiring intellectually. In particular, Glenn Ierley gave me sage advice and patient feedback throughout graduate school. Finally, I would also like to thank my family and friends at SIO and around the world, and acknowledge the genius of LongPig.

Financial support for this research was given by the ONR Coastal Dynamics and AASERT programs, the NSF CooP program, and California Sea Grant. Their support is gratefully acknowledged. The Field Research Facility, Coastal Engineering Research Center, Duck, North Carolina, provided excellent logistical support for the two Duck field experiments.

Chapter 2 of this dissertation is, in full, a reprint of Feddersen, F., R. T.

Guza, S. Elgar, T. H. C. Herbers, Alongshore momentum balances in the nearshore, *J. Geophys. Res.*, **103**, 15667–15676, 1998. Chapter 3 is, in full, a reprint of Feddersen, F., R. T. Guza, S. Elgar, T. H. C. Herbers, Alongshore bottom stress parameterizations, in preparation, 1999. Chapter 4 is, in full, a reprint of Feddersen, F., Weakly nonlinear shear waves, *J. Fluid Mech.*, **372**, 71–91, 1998. I was the primary researcher and author, and the co-authors directed and supervised the research which forms the basis of this dissertation.

VITA

April 28, 1971	Born, St. Thomas, Virgin Islands
1993	B.S. New York University, New York
1993	B.E. Stevens Institute of Technology, New Jersey
1993–1999	Research Assistant, University of California, San Diego
1999	Doctor of Philosophy University of California, San Diego

PUBLICATIONS

Feddersen, F., R. T. Guza, S. Elgar, and T. H. C. Herbers, Cross-shore structure of longshore currents during Duck94, in *Proc. 25th Int. Coastal Engineering Conf.*, pp. 3666–3679, Am. Soc. of Civ. Eng., New York, 1996.

Feddersen, F., R. T. Guza, S. Elgar, Investigating nearshore circulation using inverse methods, in *Proc. Coastal Dynamics '97*, pp. 973–982, Am. Soc. of Civ. Eng., New York, 1997.

Feddersen, F., R. T. Guza, S. Elgar, and T. H. C. Herbers, Alongshore momentum balances in the nearshore, *J. Geophys. Res.*, **103**, 15,667–15,676, 1998.

Feddersen, F. Finite amplitude shear waves, *J. Fluid Mech.*, **372**, 71–91, 1998.

Lentz, S. J., R. T. Guza, S. Elgar, F. Feddersen, and T. H. C. Herbers, Momentum Balances on the North Carolina inner shelf, *J. Geophys. Res.*, in press, 1999.

FIELDS OF STUDY

Major Field: Oceanography

Studies in Mathematics.

Professors W. R. Young, P. Cessi, G. R. Ierley

Studies in Physical and Dynamical Oceanography

Professors L. D. Talley and M. C. Hendershott

Studies in Data Analysis

Professors R. E. Davis, D. Rudnick, and R. Pinkel

Studies in Fluid Mechanics

Professor W. K. Melville

Studies in Linear and Nonlinear Waves

Professors R. Salmon, R. T. Guza, and W. K. Melville

Studies in Numerical Methods

Professor G. R. Ierley

Studies in Computational Fluid Mechanics

Professor R. Somerville

Studies in Theoretical Mechanics

Professors Fredkin and Grinstein

Studies in Inverse Methods

Professor R. Parker

Studies in Coastal Oceanography

Professors R. T. Guza, C. D. Winant, D. Rogers

Studies in Marine Chemistry

Professors J. Gieskes and R. F. Keeling

ABSTRACT OF THE DISSERTATION

Nearshore Circulation

by

Falk Feddersen

Doctor of Philosophy in Oceanography

University of California, San Diego, 1999

Professor R. T. Guza, Chair

Nearshore circulation is the mean flow in the region from the shoreline to about a kilometer offshore. An understanding of nearshore circulation is important to understanding sediment transport, pollution dispersion, and the distribution of various marine invertebrates. This thesis addresses the following question. Are the dynamics of the alongshore current described by a 1-D balance (neglecting alongshore variations) between wave and wind forcing against bottom stress and lateral mixing? Observations are used to close integrated momentum balance, suggesting that a 1-D balance is appropriate. The alongshore bottom stress must be parameterized in models. Various parameterizations are examined in detail and it is found that most nonlinear parameterizations are adequate for modeling purposes. The alongshore current may also be unstable. For marginally unstable Reynolds numbers, the instability of the alongshore current is investigated analytically, and an amplitude equation for a weakly nonlinear shear wave is derived. The characteristics of a equilibrated shear wave (obtained from a 2-D numerical model) are well described by the theory. Future work will involve numerical modeling of nearshore circulation, and a nearshore circulation model I have implemented is described.

Chapter I

Introduction

The nearshore extends from the beach to roughly a kilometer offshore, encompassing the region of wave shoaling and the surf zone, the region of wave breaking. Nearshore circulation, the time-averaged (over many surface gravity wave periods), includes processes such as alongshore currents, shear instabilities, rip currents, and undertow. The ultimate scientific goal pursued here is to understand the dynamics of and successfully model nearshore circulation. However, nearshore circulation is very complicated. It is three-dimensional, highly nonlinear, spans a region with order of magnitude depth variation, and depends critically on wave and turbulence (generated by both wave breaking and the bottom boundary layer) dynamics. Simplification is necessary to begin understanding nearshore circulation, but must be done in a rational manner, with each simplification tested and determined valid or invalid. In this thesis, I test some fundamental simplifying assumptions (chapters 2 and 3) regarding nearshore circulation. In addition, theoretical work on the stability of the alongshore current (chapter 4) and numerical model development (chapter 5) is described. While this stage of my investigation is complete, much work remains.

A common simplification is to depth-integrate and time-average the three-dimensional Navier-Stokes equations, reducing the equations to two dimensions. With the assumptions of (i) constant density, (ii) hydrostatic time-averaged vertical

balance, and (iii) no rotation, the resulting forced and dissipative shallow water equations are,

$$\frac{\partial \bar{\eta}}{\partial t} + \nabla \cdot [(h + \bar{\eta})\bar{\mathbf{u}}] = 0 \quad (\text{I.1a})$$

$$\rho(\bar{\eta} + h) \left(\frac{\partial \bar{\mathbf{u}}}{\partial t} + \bar{\mathbf{u}} \cdot \nabla \bar{\mathbf{u}} \right) = -\rho g(\bar{\eta} + h)\nabla \bar{\eta} + \tau^s - \tau^b - \nabla \cdot \mathbf{S} - \nabla \cdot \mathbf{F}. \quad (\text{I.1b})$$

where $\bar{\mathbf{u}} = [\bar{u}, \bar{v}]$ represents the mean (depth and time-averaged) cross-shore and alongshore velocities, and $\bar{\eta}$ is the time-averaged sea surface elevation (setup), x and y are the the cross- and alongshore coordinates, h is the water depth (Figure I.1), and ρ is the water density. This coordinate system is used throughout the dissertation. The surface (i.e. wind) and bottom stresses are represented by τ^s and τ^b . The momentum flux due to waves is given by the radiation stress tensor \mathbf{S} and that due to turbulence and shear dispersion (interaction of depth-varying currents) is given by the depth-integrated Reynolds stress tensor \mathbf{F} . Two other common simplifications, convenient for theoretical analysis and numerical modeling, are the rigid-lid ($\partial \bar{\eta} / \partial t = 0$) assumption and $\bar{\eta} \ll h$ allowing $\bar{\eta} + h$ to be replaced with h .

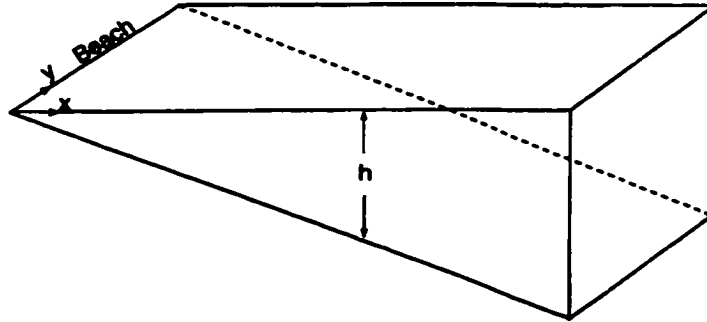


Figure I.1: The coordinate system used. Planar beach bathymetry ($h = \beta x$) is shown.

The equations (I.1) are believed to represent well the depth- and time-averaged flow, and describe a variety of processes such as edge-waves [Eckart, 1951] swash motions [Raubenheimer *et al.*, 1995], steady flow [Wu *et al.*, 1985], shear-instabilities [Allen *et al.*, 1996], and topographically controlled rip currents [Arthur, 1962; Sancho *et al.*, 1995]. Important processes not described include undertow (depth variation of the mean cross-shore current), instabilities of undertow [e.g. Li *et al.*, 1998], and the bottom boundary layer crucial to the understanding of bottom stress and sediment transport.

The radiation and Reynolds stresses can be exactly written as depth- and time-integrated functions of the wave and turbulent velocities respectively. However, these quantities are not resolved by (I.1), and are also poorly understood and difficult to measure. For closure, both a wave and turbulence model are required to parameterize the two stresses. The radiation stress is often related to the frequency-directional wave energy spectrum via linear theory, although other models that incorporate nonlinear or breaking-wave roller effects are also used. The various models for the depth-averaged Reynolds stresses are usually based on an eddy-viscosity concept.

The bottom stress depends on the details of both the bottom boundary layer and the breaking wave generated turbulence which transport momentum to the bottom. These processes also are not resolved in a 2-D model, therefore an instantaneous stress dependence that is a quadratic in the instantaneous velocities is often adopted, in analogy to steady open-channel flow. The time-averaged alongshore bottom stress τ_y^b is

$$\tau_y^b = \rho c_f \langle |\vec{u}|v \rangle, \quad (\text{I.2})$$

where $\langle \cdot \rangle$ represents a time average over many wave periods, c_f is a nondimensional drag coefficient, $|\vec{u}|$ is the magnitude of the total instantaneous horizontal velocity vector, and v the instantaneous alongshore velocity. Both mean and wave velocities contribute to the nonlinear term $\langle |\vec{u}|v \rangle$. This quadratic bottom stress

representation is not verified because direct measurements of the bottom stress in the nearshore are lacking.

Parameterizations of radiation, Reynolds, and bottom stresses are tested implicitly by examining their effect on a more easily measured quantity, the alongshore current. However, due to the number of free coefficients in the parameterizations, model-data comparison becomes little more than an exercise in curve fitting. Constraints on either the parameterizations or the coefficients that go into them are essential to further understanding of nearshore circulation.

There is great interest in modeling the alongshore current, which transports sand, causing beach erosion and blocking of harbor entrances. The depth-integrated and time-averaged alongshore momentum equation often is simplified further by invoking two assumptions, that the flow is steady ($\partial_t = 0$), and that all variables are alongshore homogeneous ($\partial_y = 0$). Immediate simplification follows due to the continuity equation (I.1a) which, with the shoreline boundary condition of no mass flux, implies $\bar{u} = 0$ everywhere, decoupling the cross- and alongshore momentum equations. The cross-shore momentum balance is between cross-shore (wave or wind) forcing and cross-shore pressure gradients [*Longuet-Higgins and Stewart, 1964*]. The alongshore momentum equation schematically simplifies to

$$\text{Forcing} = \text{Bottom Stress} + \text{Mixing},$$

where the forcing is due to both waves and wind, and can be written more formally as

$$\tau_y^{\text{wind}} - \frac{dS_{yx}}{dx} = \rho c_f \langle |\bar{u}|v \rangle + \frac{dF_{yx}}{dx}. \quad (\text{I.3})$$

One-dimensional models based on (I.3) have had both success [*Thornton and Guza, 1986*] and failure [*Church and Thornton, 1993*] describing the alongshore current. An outstanding question is whether 1-D models contain the proper dynamics of the alongshore current on a natural beach. No beach is truly alongshore

homogeneous (i.e. $\partial_y \neq 0$), and so processes such as alongshore pressure gradients may be important in the dynamics of the alongshore current. However, it is hard to verify (I.3) locally (at a single point) because, as mentioned earlier, it is difficult to measure the individual terms that comprise (I.3).

Chapter 2 [Feddersen *et al.*, 1998] suggests that 1-D models based on (I.3) can describe the alongshore current on a natural beach. A cross-shore integrated (from the shoreline to 8-m water depth) 1-D momentum balance is evaluated using data from the two-month long Duck94 field experiment. With some judicious assumptions, it is possible to estimate the cross-shore integrated terms in (I.3). Other cross-shore integrated momentum balances which separate the dynamics of the surf zone from the region seaward of the surf zone are also evaluated. There are several findings:

- The cross-shore integrated momentum balance holds, suggesting that (I.3) holds locally.
- The alongshore bottom stress is represented well by (I.2).
- There is significant cross-shore variation of the drag coefficient c_f , with a higher c_f in the surf zone.
- Alongshore wind forcing plays a significant role in the nearshore region.

An alongshore current model cannot use (I.2) to represent the bottom stress because the wave velocities are not resolved. Therefore, the term $\langle |\vec{u}|v \rangle$ must also be parameterized. Many parameterizations exist, both linear and nonlinear, which are based on various assumptions. Although it is fairly straightforward, none of the parameterizations had previously been tested with observations. In chapter 3 [Feddersen *et al.*, 1999], various parameterizations of $\langle |\vec{u}|v \rangle$ are examined using data from the Duck94 and SandyDuck field experiments. The principal findings are that:

- Linear parameterizations do not adequately reproduce $\langle |\vec{u}|v \rangle$.

- The expected value $E[|\vec{u}|v]$ based on assuming the wave velocities are joint-Gaussian random variables with the observed flow statistics is an excellent parameterization of $\langle |\vec{u}|v \rangle$.
- Various other nonlinear parameterizations (both empirical and non-empirical) work well.
- The mean alongshore current and the total wave velocity variance are the most important factors determining $\langle |\vec{u}|v \rangle$.

In the past decade it has been realized that the alongshore current on natural beaches are often unstable. Low frequency, approximately nondispersive, alongshore propagating waves with periods of $O(100 \text{ s})$ and wavelengths of $O(100 \text{ m})$, first observed by *Oltman-Shay et al.* [1989], are much shorter than the wavelengths of edge waves of the same frequency. The motions (called shear waves) are related to the intensity and direction of the mean alongshore current, and are the result of a shear-instability [*Bowen and Holman*, 1989].

The nonlinear evolution of the shear instabilities were studied numerically by *Allen et al.* [1996], who found that the shear wave behavior (from equilibrated shear waves to fully turbulent flow) is a function of an inverse Reynolds number α . At values greater than a critical value ($\alpha > \alpha_c$), the flow is stable. *Allen et al.* [1996] did not study the near critical (i.e. at α just below α_c) behavior of shear waves. An issue complicating such study is that numerical effects can alter the near critical behavior, for example inducing a false stability. In the *Allen et al.* [1996] model, finite numerical resolution and biharmonic friction (added for numerical stability) might significantly distort the solutions near α_c . Finite alongshore domain lengths also prevent potential side-band instabilities and motions on scales longer than the domain length from developing.

In Chapter 4 [*Feddersen*, 1998], the theory for weakly nonlinear shear waves at small $\alpha_c - \alpha$ is developed, using perturbation expansion techniques. At first order, linear stability is recovered. At third order, a complex Ginzburg-

Landau equation is derived for the shear wave amplitude. Solutions to the complex Ginzburg-Landau equation can exhibit a wide range of behaviors. For the conditions used in *Allen et al.* [1996] a side-band stable equilibrated shear wave is found. The agreement between theory and the model of *Allen et al.* [1996] confirms that the numerical model correctly reproduces the near-critical shear wave behavior.

A numerical model of the forced and dissipative shallow water equations (I.1) is a valuable tool for nearshore research. Investigations can range from idealized process studies (e.g. the dynamics of shear waves [*Allen et al.*, 1996]) to quantitative comparison with field observations on complex natural bathymetry. I've developed a numerical model based on (I.1) with the rigid-lid and $\bar{\eta} \ll h$ assumptions, which is similar to the model used by *Allen et al.* [1996]. Chapter 5 contains a description of the numerical implementation and validation of the rigid-lid, forced and dissipative shallow water equations.

For the future, there is need for well-tested, accurate, and robust parameterizations of both the radiation and Reynolds stress. Little is known about these terms, for example their magnitude and spatial distribution. In addition, it is, in my opinion, an open question whether turbulent mixing is dynamically significant in the surf zone. If it is, what length and time scales are doing this mixing? Is the mixing due to shear-instabilities (with a longer time scale than surface gravity waves) or due to breaking wave generated turbulence (with a shorter time scale). In addition, a better understanding of how the drag coefficient c_f depends on bed roughness, waves, and currents is required for the alongshore bottom stress. Understanding these processes in a 1-D, alongshore homogeneous context is crucial before moving to 2-D and/or full 3-D modeling. In the immediate future, I plan to use inverse methods combining the comprehensive Duck94 and SandyDuck field data and a 1-D model, to develop an increased understanding and better parameterizations of these processes.

References

- Allen, J. S., P. A. Newberger, and R. A. Holman, Nonlinear shear instabilities of alongshore currents on plane beaches, *J. Fluid Mech.* **310**, 181–213, 1996.
- Arthur, R. S., A note on the dynamics of rip currents, *J. Geophys. Res.*, **67**, 2777–2779, 1962.
- Bowen, A. J., and R. A. Holman, Shear instabilities of the mean longshore current, 1. Theory, *J. Geophys. Res.*, **94**, 18,023–18,030, 1989.
- Eckart, C., Surface waves on water of variable depth, *Wave Rep.* **100**, 99 pp., Scripps Inst. of Oceanogr., Univ. of Calif., La Jolla, 1951.
- Feddersen, F., Weakly nonlinear shear waves, *J. Fluid Mech.*, **372**, 71–91, 1998.
- Feddersen, F., R. T. Guza, S. Elgar, and T. H. C. Herbers, Alongshore momentum balances in the nearshore, *J. Geophys. Res.*, **103**, 15,667–15,676, 1998.
- Feddersen, F., R. T. Guza, S. Elgar, and T. H. C. Herbers, Alongshore bottom stress parameterizations, in preparation, 1999.
- Li, L. and R. A. Dalrymple, Instabilities of the undertow, *J. Fluid Mech.*, **369**, 175–190, 1998.
- Longuet-Higgins, M. S., and R. W. Stewart, Radiation stress in water waves: A physical discussion with application, *Deep Sea Res.*, **11**, 529–563, 1964.
- Oltman-Shay, J., P. A. Howd, and W. A. Birkemeier, Shear instabilities of the mean longshore current, 2. Field data, *J. Geophys. Res.*, **94**, 18,031–18,042, 1992.
- Raubenheimer, B., R. T. Guza, S. Elgar, and N. Kobayashi, Swash on a gently sloping beach, *J. Geophys. Res.*, **100**, 8751–8760, 1995.
- Sancho, F. E., I. A. Svendsen, A. R. Van Dongeren, and U. Putrevu, Longshore nonuniformities of nearshore currents, in *Coastal Dynamics '95*, pp. 425–436, Am. Soc. of Civ. Eng., New York, 1995.
- Wu, C. S., E. B. Thornton, and R. T. Guza, Waves and longshore currents: comparison of a numerical model with field data, *J. Geophys. Res.*, **90**, 4951–4958, 1985.

Chapter II

Alongshore Momentum Balances in the Nearshore

II.A Abstract

The one-dimensional, time-averaged (over many wave periods) alongshore momentum balance between forcing by wind and breaking waves and the bottom stress is examined with field observations spanning a wide range of conditions on a barred beach. Near-bottom horizontal currents were measured for 2 months at 15 locations along a cross-shore transect extending 750 m from the shoreline to 8-m water depth. The hourly averaged bottom stress was estimated from observed currents using a quadratic drag law. The wave radiation stress was estimated in 8-m depth from an array of pressure sensors, and the wind stress was estimated from an anemometer at the seaward end of a nearby pier. The combined wind and wave forcing integrated over the entire cross-shore transect is balanced by the integrated bottom stress. The wind stress contributes about one third of the forcing over the transect. Analysis of the momentum balances in different cross-shore regions shows that in the surf zone, wave forcing is much larger than wind forcing and that the bottom drag coefficient is larger in the surf zone than farther seaward, consistent with earlier studies.

II.B Introduction

Alongshore currents in the surf zone have been investigated extensively within the framework of steady, one-dimensional (1-D) models (*Bowen* [1969], *Longuet-Higgins* [1970], *Thornton* [1970], and others). If the topography, forcing, and alongshore current are steady and uniform in the alongshore direction, the time-averaged and vertically averaged alongshore momentum equation reduces to a 1-D balance between forcing, bottom stress, and mixing,

$$\tau_y^{\text{wind}} - \frac{\partial S_{yx}}{\partial x} = \tau_y^b + \frac{\partial F_{yx}}{\partial x} \quad (\text{II.1})$$

where x and y are the cross-shore and alongshore coordinates, respectively. The forcing is the sum of the alongshore wind stress τ_y^{wind} , which although often ignored is sometimes important in the surf zone [*Whitford and Thornton*, 1993, 1996], and wave forcing, represented by the cross-shore gradient of the radiation stress component $-S_{yx}$ [*Longuet-Higgins and Stewart*, 1964]. Linear theory is used often to relate S_{yx} to the frequency-directional wave spectrum $E(f, \theta)$ [e.g. *Battjes*, 1972] or in bulk wave transformation models to the wave height H_{rms} , mean wave angle $\bar{\theta}$, and the mean wave frequency \bar{f} [e.g. *Thornton and Guza*, 1983]. The mean alongshore bottom stress is often parameterized as [*Longuet-Higgins*, 1970]

$$\tau_y^b = \rho c_f \langle |\vec{u}| v \rangle \quad (\text{II.2})$$

where ρ is the water density, c_f is a drag coefficient, $|\vec{u}|$ is the magnitude of the total velocity vector above the bottom boundary layer, v is the alongshore velocity component, and $\langle \rangle$ represents a time average over many wave periods. This quadratic form for the bottom stress has been used widely in steady channel flows [e.g. *Henderson*, 1966] but has not been verified directly in the surf zone. Mixing is given by the cross-shore gradient of the depth-integrated turbulent momentum flux F_{yx} . Although F_{yx} can be written exactly in terms of depth-integrated Reynolds stresses

and the interaction of depth-varying currents [Svendsen and Putrevu, 1994], there is no accepted turbulence closure scheme, so F_{yx} is parameterized typically as proportional to the mean alongshore current shear $\partial\bar{v}/\partial x$, where \bar{v} is the time-averaged alongshore current.

The alongshore momentum equation (II.1) with the quadratic bottom stress (II.2) is difficult to solve for \bar{v} . If a weak mean current and small wave angle are assumed, the bottom stress can be approximated as a linear function of \bar{v} [e.g. Longuet-Higgins, 1970]

$$\tau_y^b \propto \sigma_u \bar{v} \quad (\text{II.3})$$

where σ_u^2 is the cross-shore orbital wave velocity variance. Given this approximation and parameterized forms for the wave transformation and mixing, solutions for \bar{v} can be found. However, in the surf zone the linearizing assumptions for the bottom stress often are violated [Thornton and Guza, 1986], and the general relationship between $\langle |\vec{u}|v \rangle$ and $\sigma_u \bar{v}$ is not understood well.

Alongshore currents predicted by (II.1) using a random wave transformation model for S_{yx} , a linearized bottom stress (II.3), and neglecting mixing ($\partial F_{yx}/\partial x = 0$) agree well with mean alongshore currents observed on a nearly plane beach with a small range of incident wave angles [Thornton and Guza, 1986]. However, there are large discrepancies between 1-D model predictions and observations on a barred beach near Duck, North Carolina acquired during the DELILAH field experiment [Church and Thornton, 1993; Smith et al., 1993]. The beach at Duck is complex, with a wide range of wind and wave conditions [Long, 1996] and complicated bathymetry that includes prominent sandbars and sometimes pronounced alongshore inhomogeneities [Lippmann and Holman, 1990]. During DELILAH a broad alongshore current often was observed, with a single maximum shoreward of the crest of the sandbar, whereas 1-D models predict a flow with two narrow jets, one slightly seaward of the bar crest and one near the shoreline (i.e. in the regions

where the predicted wave breaking causes large gradients in S_{yx}), with weak flow in between the jets.

The reasons for this discrepancy are unclear, but possible model deficiencies fall into two general classes. First, the 1-D momentum balance (II.1) may be correct, but the parameterization of wave forcing, bottom stress, or mixing may be either incorrect or not robust over the wide range of conditions at Duck (*Svendsen* [1984], *Church and Thornton* [1993], *Svendsen and Putrevu* [1994], *Dally and Brown* [1995], *Slinn et al.* [1998], *Garcez Faria et al.* [1998], and many others). Alternatively, the 1-D momentum balance (II.1) may be missing important two-dimensional (2-D) terms such as nonlinear advection and alongshore pressure gradients associated with alongshore depth variations. Model simulations suggest that these terms may be significant on natural beaches [*Putrevu et al.*, 1995; *Sancho et al.*, 1995; *Reniers et al.*, 1995].

Here the 1-D momentum balance (II.1) is tested with field observations (discussed in section 2) collected over a wide range of conditions on the barred beach near Duck, North Carolina. The alongshore momentum balance, integrated over the instrumented cross-shore transect, is examined in section 3. This integrated balance spanning the entire surf zone (as opposed to the local balance examined by *Whitford and Thornton* [1996]) is independent of the poorly understood gradients of the turbulent momentum flux F_{yx} and radiation stress S_{yx} appearing in the local 1-D balance (II.1). The cross-shore integrated total (wind and wave) forcing is shown to be balanced approximately by the cross-shore integrated bottom stress, using the quadratic friction formulation (II.2). The closure of the cross-shore integrated momentum balance suggests that the dynamics of the alongshore current are on average described by the 1-D momentum balance (II.1). However, there are cases in which 2-D effects are important, as discussed in section 4. The results are summarized in section 5.

II.C Observations

The data were collected during September and October of 1994 near Duck, North Carolina on a barrier island exposed to the Atlantic Ocean. The U.S. Army Corps of Engineers Field Research Facility (FRF) coordinate system, with x increasing offshore and y increasing in the northerly direction, is used. Directional properties of sea and swell were estimated from a two-dimensional array of 15 bottom-mounted pressure sensors in 8-m water depth (Figure II.1), operated by the FRF [Long, 1996]. Hourly radiation stresses were estimated accurately using linear theory and a directional-moment-estimation technique that minimizes a weighted sum of the bias and statistical variability of the estimate [Elgar *et al.*, 1994]. Errors in the S_{yx} estimates are small compared to uncertainties in other terms of the integrated momentum balances investigated here. Wind speed and direction measured 19.5 m above mean sea level at the end of the nearby FRF pier were used to estimate wind stress (S. Lentz, personal communication, 1995) using the algorithm of *Large and Pond* [1981]. No corrections were made for the possibly significant, but poorly understood, effect of waves on the wind stress [e.g. *Rieder et al.*, 1996]. Observations from a 60-km-long five-element alongshore array of pressure sensors in 6-m water depth [Alessi *et al.*, 1996] were used to obtain hourly estimates of the alongshore pressure gradient near the shore associated with shelf-scale barotropic motions (Appendix A).

Colocated sonar altimeters [Gallagher *et al.*, 1996], pressure sensors, and bidirectional electromagnetic current meters (sampled at 2 Hz) were deployed on a cross-shore transect extending 750 m from near the shoreline to 8-m water depth (Figures II.1 and II.2). Sonar altimeters measure acoustically the distance from the altimeter (mounted on a fixed frame) to the bed. Altimeter data were used to estimate depth profiles on the instrument transect [Gallagher *et al.*, 1998]. Current meter offset drift was accounted for by regularly rotating the current meters 180 deg and assuming a stationary mean current during approximately 10-min periods

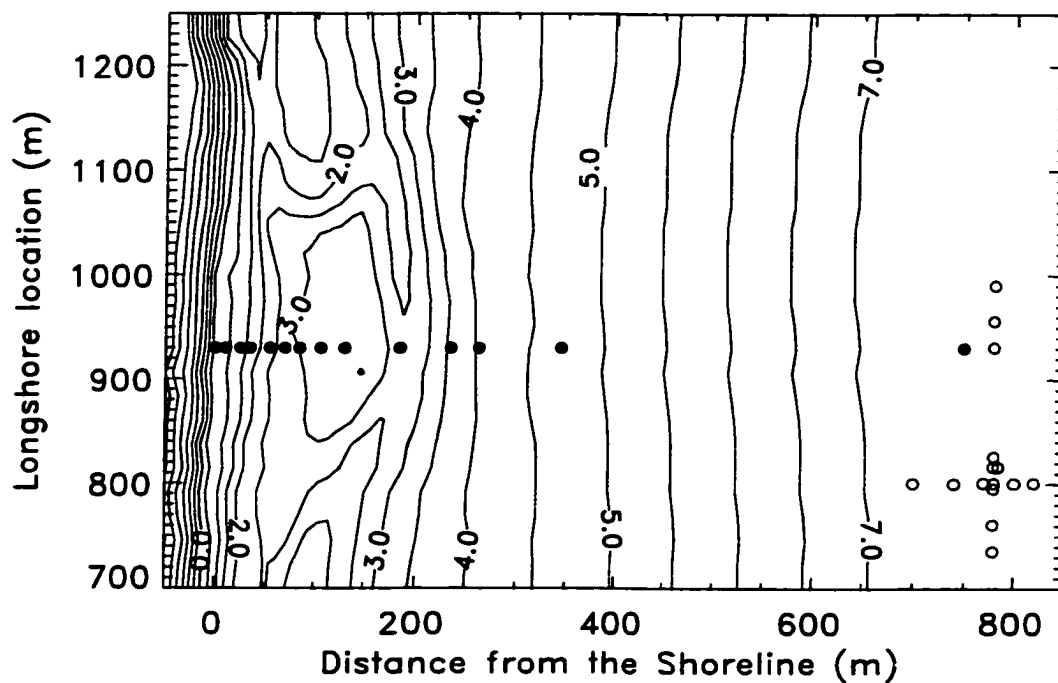


Figure II.1: Plan view of the beach at Duck. A solid circle represents a colocated pressure sensor, current meter, and sonar altimeter. The open circles represent the Field Research Facility pressure sensor array. Bathymetry from October 20 is contoured in units of meters below mean sea level. Wind speed was measured about 500 m from the shoreline at alongshore location 500 m.

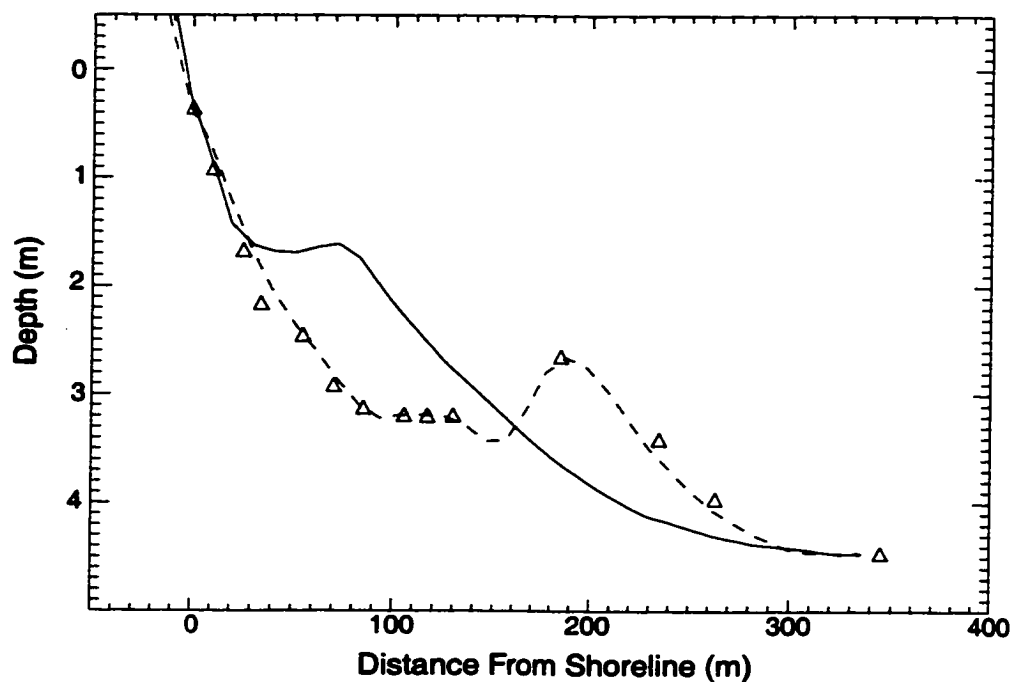


Figure II.2: The cross-shore location of colocated current meters, pressure sensors, and sonar altimeters (triangles); bathymetry observed on August 25 (solid curve) and October 26 (dashed curve). An additional colocated pressure sensor and current meter in 8-m water depth, 750 m from the shoreline, is not shown.

before and after the rotation. Biofouling required repeated cleaning of the current meter probes. Data from heavily biofouled current meters or with possibly large offset-drift-induced errors were discarded. Estimated errors in the measured mean alongshore flows are 0.05 m/s (arising primarily from offset drift) plus 5% of the true mean flow speed owing to inaccuracy in the current meter gain and orientation. The most nearshore sensor was often exposed at low tide and therefore inactive. The 15 current meters were raised or lowered as the bed level changed to maintain an elevation of 0.4-1.0 m above the seafloor.

Conditions during the experiment are summarized in Figure II.3. In 8-m water depth the significant wave height (H_{sig}) ranged between 0.2 and 4.0 m (Figure II.3a), and the mean wave angle ranged between ± 50 deg (Figure II.3b). The mean (e.g. centroidal) wave frequency ranged between 0.08 and 0.2 Hz (not shown). The maximum mean alongshore current $|\bar{v}_{\text{max}}|$ (in each hour-long record) ranged from 0.1 to 1.4 m/s (Figure II.3c). The bar crest, originally located 80 m from the shoreline, migrated 120 m farther offshore (Figure II.3d and Figure II.2). The observed locations of \bar{v}_{max} spanned the entire instrumented region, but were usually located within 150 m of the shoreline, and shoreward of the bar crest (Figure II.3d). The few maxima located well seaward of the bar crest ($400 \text{ m} < x \leq 750 \text{ m}$) were weak ($|\bar{v}_{\text{max}}| \sim 0.3 - 0.4 \text{ m/s}$) and approximately correspond to times of strong buoyancy-driven flows [Rennie, 1998]. The stronger alongshore currents ($|\bar{v}_{\text{max}}| \geq 0.8 \text{ m/s}$) were often wave driven (e.g. associated with large S_{yz} in 8-m water depth, Figure II.4) and occurred near the bar crest. Maxima near the shoreline were weaker (0.25-0.7 m/s). Many of the larger $|\bar{v}_{\text{max}}|$ (0.4-0.7 m/s) near the shoreline occurred in mid to late October after the sandbar migrated offshore (Figure II.3d). The alongshore component of the wind ranged between 15 m/s from the north and 10 m/s from the south (not shown). The surf zone width (estimated as described in Appendix B) ranged from 10 to 750 m. Spring tides were about 1 m, and the slope of the beach foreshore was about 1/10 (Figure II.2), so tidal fluctuations in the mean shoreline location were about 10 m. Alongshore

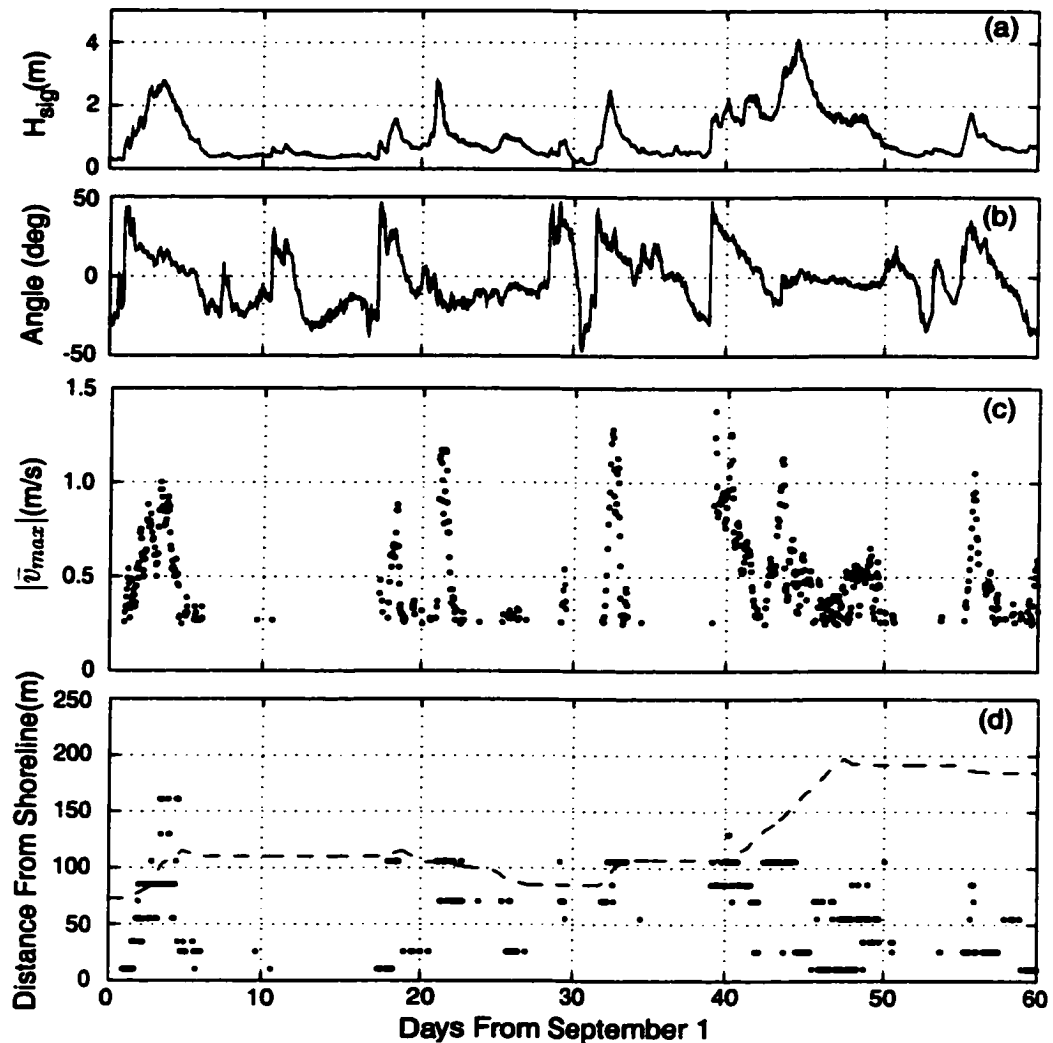


Figure II.3: Hourly values of (a) significant wave height H_{sig} and (b) mean incident wave angle [Kuik *et al.* 1985] in 8-m depth (zero corresponds to normal incidence and positive angles to waves from the northern quadrant). (c) Absolute value of the maximum hourly averaged alongshore current $|\bar{v}_{max}|$ and (d) cross-shore location of the bar crest (dashed) and of \bar{v}_{max} . The 572 values of $|\bar{v}_{max}|$ shown correspond to hours with at least five active current meters and $|\bar{v}_{max}| \geq 0.25$ m/s. The few maxima occurring > 250 m from shore are not shown in Figure 3d.

barotropic tidal currents in water depths < 8 m were less than roughly 0.03 m/s (S. Lentz, personal communication, 1996).

Spatially extensive bathymetric surveys (e.g. Figure II.1) were obtained several times during the data collection period with the CRAB (Coastal Research Amphibious Buggy). The orientations of the 1-, 2-, 3-, 4-, and 5-m depth contours over an alongshore span of 300 m that included the instrumented transect were determined by least squares fits of each depth contour to a straight line. The orientation angle of a particular depth contour changed over time, and the orientation of different depth contours varied $O(5^\circ)$ within a given survey. Particular depth contours sometimes were fit poorly by the surveys, indicating that the bathymetry was alongshore inhomogeneous (e.g. Figure II.1). However, mean (averaged over all depths for a single survey) contour orientations varied by no more than $\pm 2^\circ$ from the FRF coordinate system. The results in section 3 are not altered significantly by $\pm 2^\circ$ rotation of the coordinate frame.

Guza et al. [1986] reported a strong correlation ($r^2 = 0.94$) between an empirical orthogonal function-derived \bar{v}_{\max} and $-S_{yx}$ estimated outside the surf zone on a nearly plane beach with a smaller range of incident wave angles than those observed here. The lower correlation between \bar{v}_{\max} and $-S_{yx}$ ($r^2 = 0.76$) at Duck (Figure II.4) reflects a greater complexity of bathymetric, wave, and wind conditions. Wind stress, buoyancy forcing, the effect of alongshore inhomogeneities, and flow acceleration all contribute to the scatter between $-S_{yx}$ and \bar{v}_{\max} and dominate cases in which $-S_{yx}$ and \bar{v}_{\max} have opposite sign. The overall importance of terms other than S_{yx} to the alongshore momentum balance is unknown.

Wind is sometimes a substantial momentum source in the nearshore [*Whitford and Thornton*, 1993] and is included in the momentum balances investigated here. The sometimes significant effect of wind forcing and the dynamical separation between the surf zone and the wind-driven region seaward of the surf zone is illustrated in Figure II.5 for a case where wind and wave forcing have opposite sign.

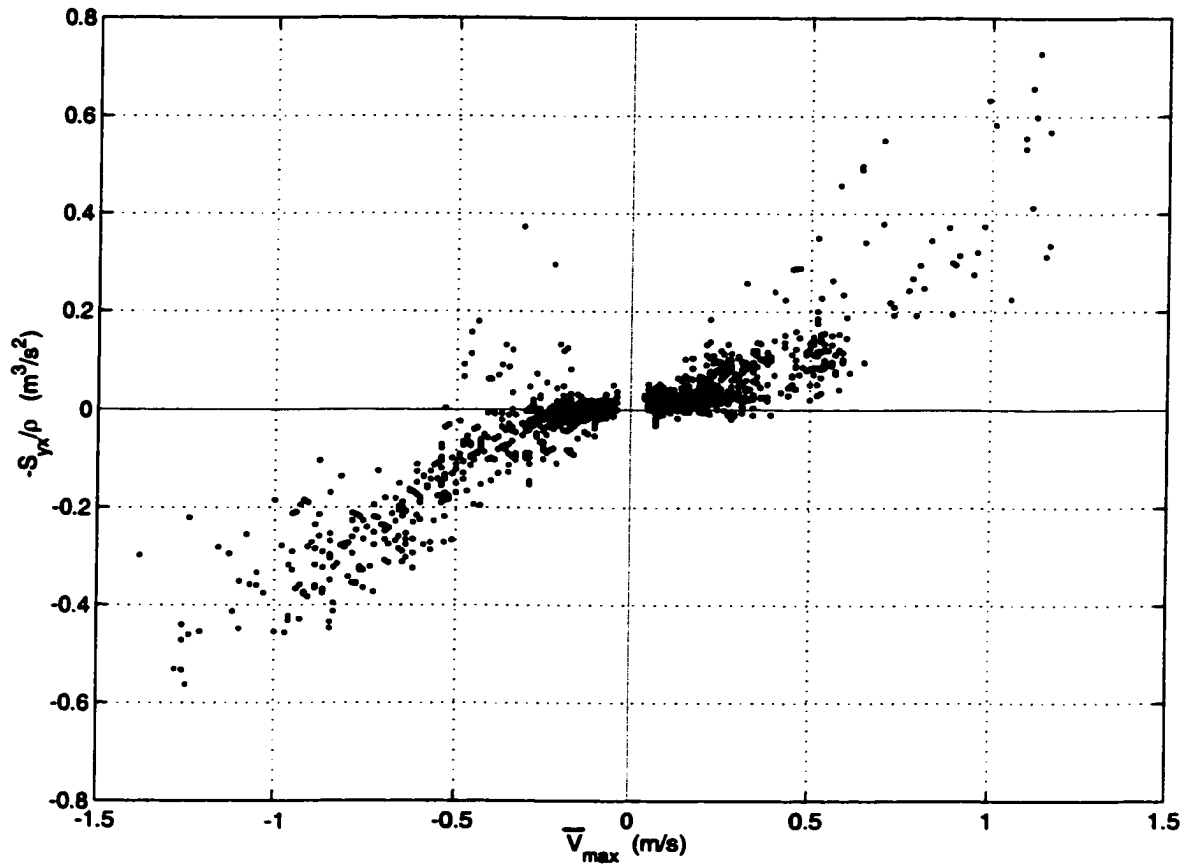


Figure II.4: The radiation stress $-S_{yx}/\rho$ in 8-m depth versus the alongshore current maximum \bar{v}_{\max} ($r^2 = 0.76$). An observation is shown only if at least five sensors were active.

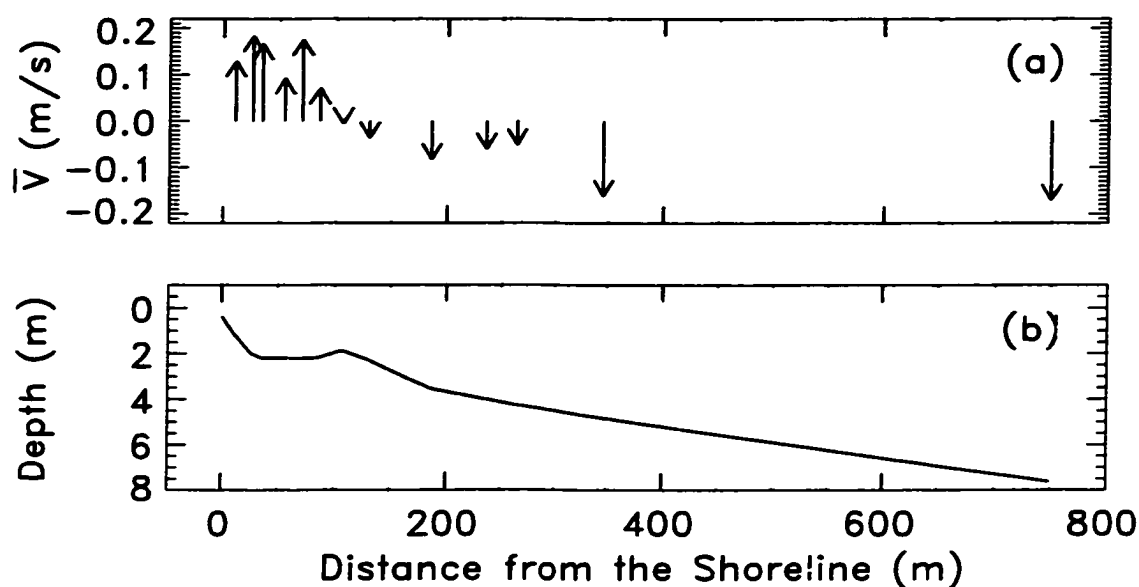


Figure II.5: (a) Hourly averaged alongshore current \bar{v} versus distance from the shoreline and (b) depth observed at 1300 eastern standard time September 21. Arrows pointing toward the bottom of the figure indicate southward flow.

Moderately energetic waves ($H_{\text{sig}} \approx 1$ m in 8-m water depth) approached from the south while the 4 m/s wind was from the north. The wind-driven current flowed toward the south seaward of the bar crest, and a wave-driven current flowed toward the north shoreward of the bar crest (where wave breaking began). The observed sign change in \bar{v} highlights the transition from wind- to wave-driven flow. Even though the alongshore currents were weak, the division between the wind- and the wave-driven regimes was observable for the entire 48-hour period (September 20-21) when wind and wave forcing had opposite sign, and the location of current reversal fluctuated as the surf zone width was modulated by tidal changes in water depth. See *Feddersen et al.* [1996] for further discussion of case studies.

II.D Alongshore Momentum Balances

The depth-integrated and time-averaged alongshore momentum equation is [e.g. *Mei*, 1989]

$$\rho(\bar{\eta} + h) \left(\frac{\partial \bar{v}}{\partial t} + \bar{u} \frac{\partial \bar{v}}{\partial x} + \bar{v} \frac{\partial \bar{v}}{\partial y} \right) = -\rho g(h + \bar{\eta}) \frac{\partial \bar{\eta}}{\partial y} - \frac{\partial S_{yx}}{\partial x} - \frac{\partial S_{yy}}{\partial y} - \tau_y^b + \tau_y^{\text{wind}} - \left(\frac{\partial F_{yx}}{\partial x} + \frac{\partial F_{yy}}{\partial y} \right) \quad (\text{II.4})$$

where \bar{u} and \bar{v} are the depth- and time-averaged (over many wave cycles) cross-shore and alongshore velocities, h is the water depth, $\bar{\eta}$ is the mean free surface displacement, S_{yx} and S_{yy} are components of the radiation stress tensor, F_{yx} and F_{yy} are components of the depth-integrated turbulent momentum flux tensor, and τ_y^{wind} is the alongshore component of the wind stress. The alongshore bottom stress τ_y^b is represented by a quadratic drag law (II.2). Earth rotation and variation of the water density ρ are neglected.

The assumptions of a steady state and no alongshore (y) variation, coupled with the continuity equation and a no mass flux boundary condition at the shoreline, yield $\bar{u} = 0$. The nonlinear terms and alongshore gradients of S_{yy} , F_{yy} , and $\bar{\eta}$ in (II.4) therefore vanish, and the alongshore momentum equation (II.4) simplifies to the one-dimensional balance (II.1).

The 1-D momentum balance (II.1) is not verified locally (e.g. at a single location) because gradients of the radiation stress S_{yx} and the turbulent momentum flux F_{yx} cannot be estimated well from these observations. However, if S_{yx} and F_{yx} are known at two cross-shore locations x_1 and x_2 , the cross-shore integral of (II.1) between x_1 and x_2 can be estimated as

$$\int_{x_1}^{x_2} \frac{\tau_y^{\text{wind}}}{\rho} dx - \frac{S_{yx}}{\rho} \Big|_{x_2} + \frac{S_{yx}}{\rho} \Big|_{x_1} = \int_{x_1}^{x_2} c_f \langle |\bar{u}|v \rangle dx + \frac{F_{yx}}{\rho} \Big|_{x_2} - \frac{F_{yx}}{\rho} \Big|_{x_1} \quad (\text{II.5})$$

Here this integrated balance is tested statistically for several cross-shore regions. The spatial structure of the alongshore current is not addressed by the analysis.

The first integration region spans the entire 750-m-long transect, from near the shoreline ($x_1 = 0$) to 8-m water depth ($x_2 = x_{8m}$). Pressure array data in 8-m water depth are used to estimate S_{yx} at x_{8m} . The turbulent momentum flux F_{yx} is assumed negligible in 8-m water depth ($F_{yx}|_{x_{8m}} = 0$) because the surf zone (where mixing is believed strongest) rarely extended to x_{8m} . Assuming that S_{yx} and F_{yx} are zero at the shoreline and that c_f and τ_y^{wind} are spatially homogeneous, (II.5) becomes

$$\frac{\tau_y^{\text{wind}}}{\rho} x_{8m} - \frac{S_{yx}}{\rho} \Big|_{x_{8m}} = c_f \int_0^{x_{8m}} \langle |\vec{u}|v \rangle dx \quad (\text{II.6})$$

where the only unknown is c_f . The integral is estimated from the observations as described in Appendix C.

Wind ($\tau_y^{\text{wind}} x_{8m} / \rho$) and wave ($-S_{yx} / \rho|_{x_{8m}}$) forcing terms integrated across the 750-m region during the 2-month experiment are shown in Figure II.6. The rms wind forcing is about half the rms wave forcing and thus cannot be neglected. The wind and wave forcing are visually correlated but occasionally have opposite signs (e.g. September 20-21, days 19-20, and October 14, day 43, in Figure II.6).

The integrated total (wind and wave) forcing and bottom stress are highly correlated ($r^2 = 0.87$), and linear regression gives a best fit $c_f = 0.0015$ ($\pm 1.2 \times 10^{-4}$, the 95% confidence limits on c_f) (Figure II.7). The linear relationship suggests that the current meter array adequately resolved the cross-shore structure of the flow, the bottom stress is represented well by (II.2), and the integrated 1-D momentum balance holds.

The integrated wind forcing is not negligible, but because the wind and wave forcing terms are correlated (Figure II.6) it is possible that a balance between integrated wave forcing and bottom stress (i.e. neglecting wind forcing) closes equally well. However, the correlation between wave forcing and bottom stress

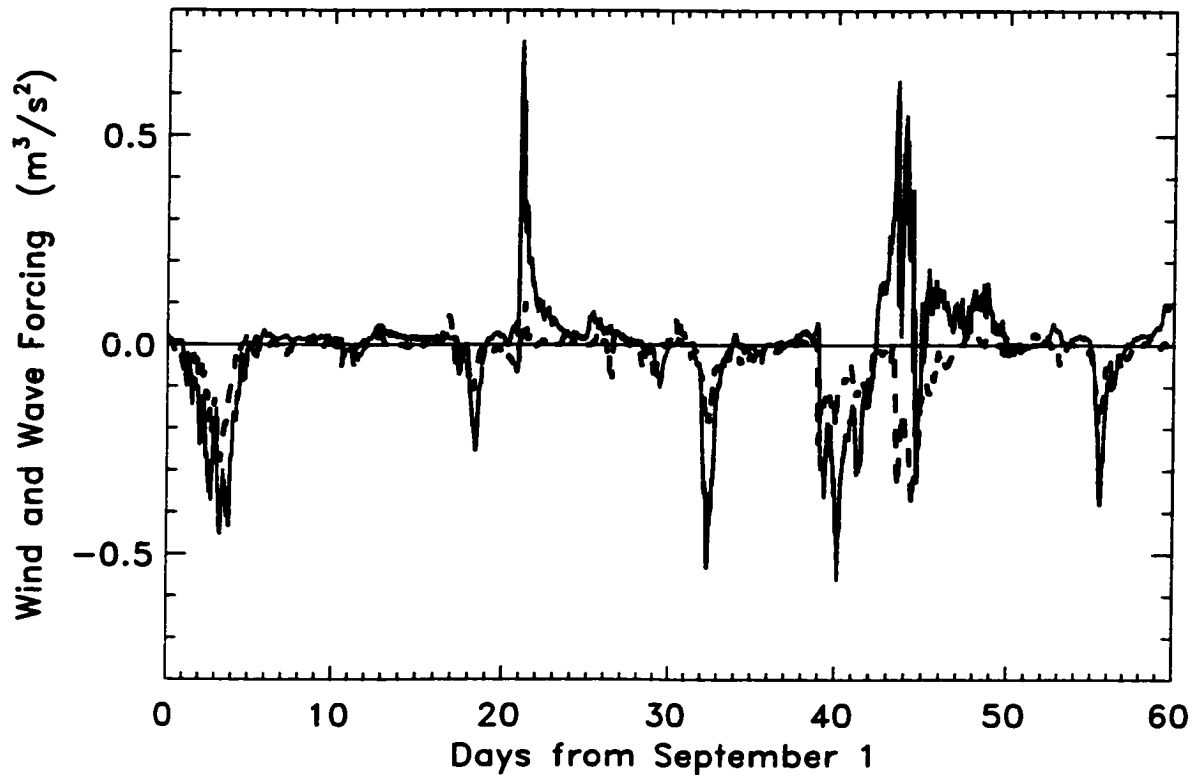


Figure II.6: Hourly integrated (from the shoreline to 8-m depth) wave ($-S_{yx}/\rho|_{x_{8m}}$ solid curve) and wind ($\int_0^{x_{8m}} (\tau_y^{\text{wind}}/\rho) dx$ dashed curve) forcing versus time. Positive corresponds to northward forcing. The means are -0.0085 and -0.0278 m^3/s^2 , and the standard deviations are 0.1296 and 0.0616 m^3/s^2 for wave and wind forcing, respectively.

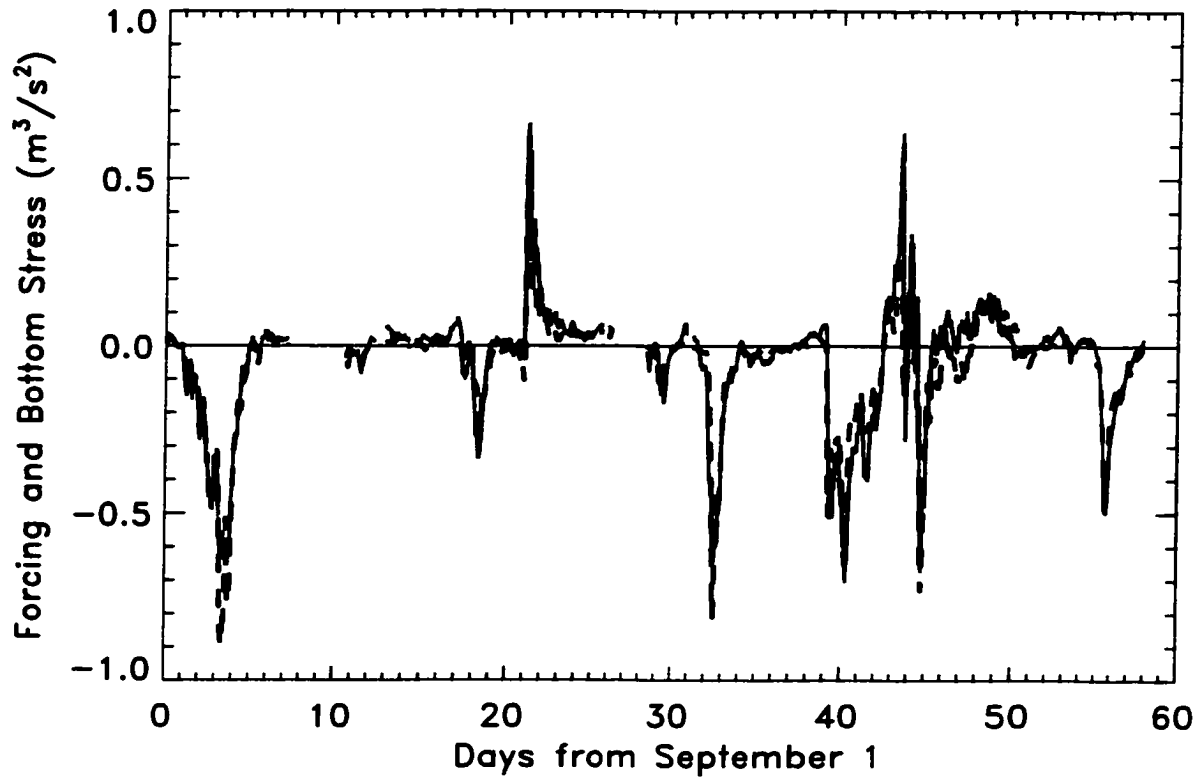


Figure II.7: Hourly total forcing (wind and wave, $-S_{yx}/\rho|_{x_{8m}} + \int_0^{x_{8m}} (\tau_y^{\text{wind}}/\rho) dx$ solid curve) and bottom stress ($c_f \int_0^{x_{8m}} \langle |\vec{u}|v \rangle dx$ dashed curve) integrated from the shoreline to 8-m depth with a best fit $c_f = 0.0015$ versus time. Gaps occur when the bottom stress integral could not be computed because of inactive sensors. The correlation coefficient squared $r^2 = 0.87$.

($r^2 = 0.73$) is significantly (at the 95% confidence level) lower than the correlation including wind forcing ($r^2 = 0.87$), demonstrating the importance of wind forcing over this region. The drag coefficient estimate is reduced from $c_f = 0.0015$, when wind stress is included, to $c_f = 0.0010$, when it is neglected.

To investigate possible spatial variation in c_f , the instrumented cross-shore transect was divided into regions within and seaward of the surf zone. Without assumptions about the evolution of S_{yx} and introducing friction coefficients c_{f1} and c_{f2} within and seaward of the surf zone, respectively, the momentum balances in each region are

$$\frac{\tau_y^{\text{wind}}}{\rho} x_b - \frac{S_{yx}}{\rho} \Big|_{x_b} = c_{f1} \int_0^{x_b} \langle |\vec{u}|v \rangle dx + \frac{F_{yx}}{\rho} \Big|_{x_b} \quad (\text{II.7})$$

and

$$\frac{\tau_y^{\text{wind}}}{\rho} (x_{8m} - x_b) - \frac{S_{yx}}{\rho} \Big|_{x_{8m}} + \frac{S_{yx}}{\rho} \Big|_{x_b} = c_{f2} \int_{x_b}^{x_{8m}} \langle |\vec{u}|v \rangle dx - \frac{F_{yx}}{\rho} \Big|_{x_b} \quad (\text{II.8})$$

where x_b is the location of the border between the two regions. Adding (II.7) and (II.8) yields a balance over the entire region similar to (II.6) (but with a variable drag coefficient) given by

$$\frac{\tau_y^{\text{wind}}}{\rho} x_{8m} - \frac{S_{yx}}{\rho} \Big|_{x_{8m}} = c_{f1} \int_0^{x_b} \langle |\vec{u}|v \rangle dx + c_{f2} \int_{x_b}^{x_{8m}} \langle |\vec{u}|v \rangle dx \quad (\text{II.9})$$

The location of x_b is determined from estimated changes in wave energy flux as described in Appendix B. Only cases with several sensors both within and seaward of the surf zone are included (Appendix C) in determining, using multiple linear regression, best fit values for the drag coefficients. For the subset of data used to find c_{f1} and c_{f2} the correlation with a varying c_f ($r^2 = 0.82$) is significantly higher (at 95% confidence limits) than with a constant c_f ($r^2 = 0.76$). The regression yields $c_{f1} = 0.0033 (\pm 6.9 \times 10^{-4})$ and $c_{f2} = 0.0010 (\pm 2.3 \times 10^{-4})$.

The closure of the integrated-to-8-m-depth momentum balances (II.6) and (II.9) suggests that the quadratic form (II.2) does represent well the mean along-shore bottom stress. *Cox et al.* [1996] recently demonstrated in a laboratory surf zone that the instantaneous cross-shore bottom stress inferred from logarithmic oscillating boundary layer theory is related to the instantaneous product $|u|u$ outside the boundary layer over most phases of a wave cycle. The utility of the quadratic bottom stress parameterization is thus supported by observations at different temporal and spatial scales.

The surf zone drag coefficient $c_{f1} = 0.0033$ is similar to the c_f values inferred by *Whitford and Thornton* [1996] and (for low bed roughness) *Garcez Faria et al.* [1998]. The larger inferred c_f in the surf zone is consistent with the hypothesis that breaking-wave-induced turbulence enhances vertical mixing and thus increases the bottom stress for the same free stream velocity [*Church and Thornton*, 1993] and is consistent with the magnitude of c_f variations observed by *Cox et al.* [1996].

Assuming S_{yx} is conserved seaward of x_b (e.g. $S_{yx}|_{x_b} = S_{yx}|_{x_{8m}}$) and the turbulent momentum flux at x_b is negligible (e.g. $F_{yx}|_{x_b} = 0$), the momentum balances within (II.7) and seaward (II.8) of the surf zone can be considered separately. In the surf zone the balance is between wind and wave forcing and bottom stress

$$\frac{\tau_y^{\text{wind}}}{\rho} x_b - \frac{S_{yx}}{\rho} \Big|_{x_{8m}} = c_{f1} \int_0^{x_b} \langle |\vec{u}|v \rangle dx \quad (\text{II.10})$$

whereas seaward of x_b , the balance is between wind forcing and bottom stress

$$\frac{\tau_y^{\text{wind}}}{\rho} (x_{8m} - x_b) = c_{f2} \int_{x_b}^{x_{8m}} \langle |\vec{u}|v \rangle dx \quad (\text{II.11})$$

For the surf zone momentum balance (II.10) $r^2 = 0.79$, and the best fit drag coefficient is $c_{f1} = 0.0035 (\pm 4.1 \times 10^{-4})$ (Figure II.8). On average, the wind forcing is small, roughly 10% of the wave forcing in the surf zone (although in some

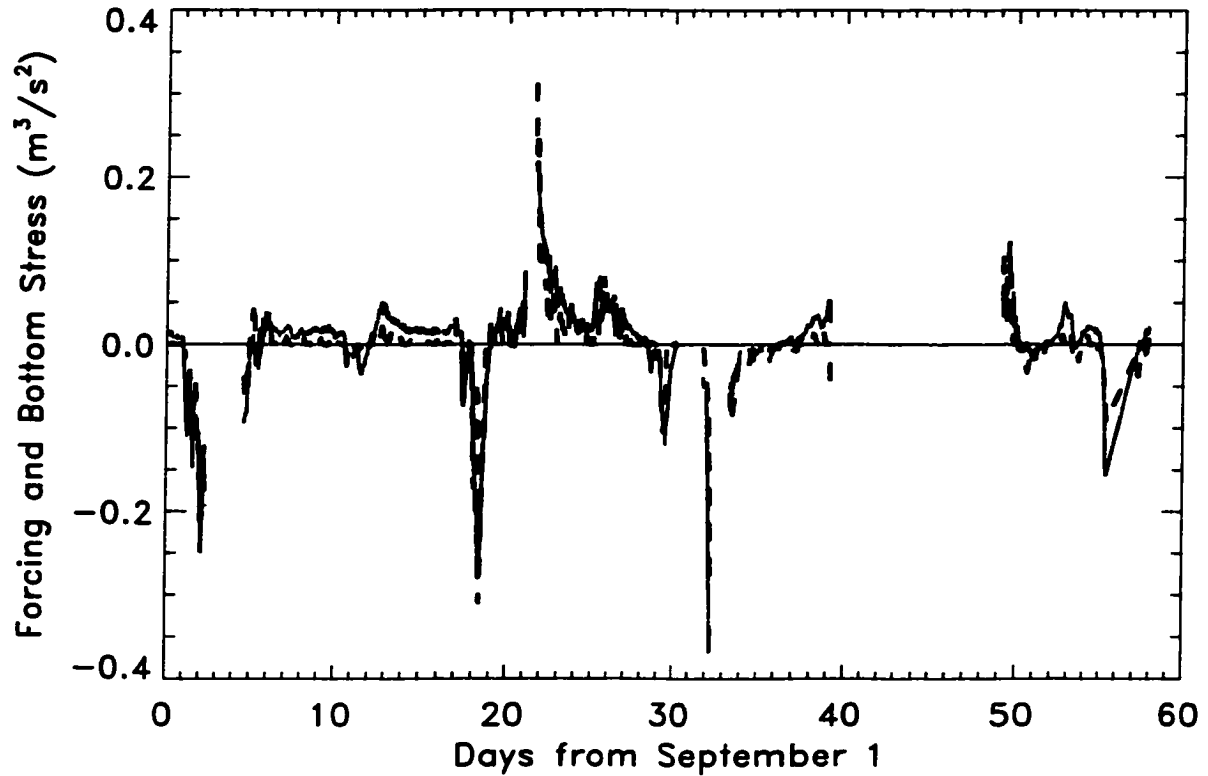


Figure II.8: Hourly total forcing (wind and wave, $-S_{yx}/\rho|_{x_{sm}} + \int_0^{x_b} (\tau_y^{\text{wind}}/\rho) dx$ solid curve) and bottom stress ($c_{f1} \int_0^{x_b} \langle |\vec{u}|v \rangle dx$ with $c_{f1} = 0.0035$ dashed curve) integrated over the surf zone versus time. The correlation coefficient squared $r^2 = 0.79$.

cases, the wind stress is important). The similarity between the surf zone drag coefficients inferred from (II.10) and (II.9) suggests that the turbulent momentum flux across x_b , $F_{yx}|_{x_b}$ (neglected in (II.10)) is either uncorrelated with (which seems unlikely) or is small relative to the surf zone bottom stress.

The momentum balance (II.11) between wind forcing and bottom stress seaward of the surf zone ($r^2 = 0.36$, Figure II.9) does not close as well as the surf zone momentum balance (II.10). If the errors causing the low correlation result solely from (Gaussian, zero mean) estimation error of the wind forcing or bottom stress, the drag coefficient would be similar to the one estimated by (II.9). However, the drag coefficients are different. The reduced estimate of $c_f = 0.00055 (\pm 2.0 \times 10^{-4})$ from the seaward of the surf zone balance (II.11) versus $c_f = 0.0010 (\pm 2.3 \times 10^{-4})$ from (II.9) suggests that the balance (II.11) does not account for sources of momentum important to the region seaward of the surf zone, which are implicitly included in (II.9). For example, S_{yx} may not be conserved seaward of the estimated x_b . Alternatively, the turbulent momentum flux F_{yx} across x_b may be significant relative to the bottom stress seaward of the surf zone, and thus the surf zone may be a substantial source of momentum to the region seaward of the surf zone. The present observations cannot be used to separate these two possible sources of momentum.

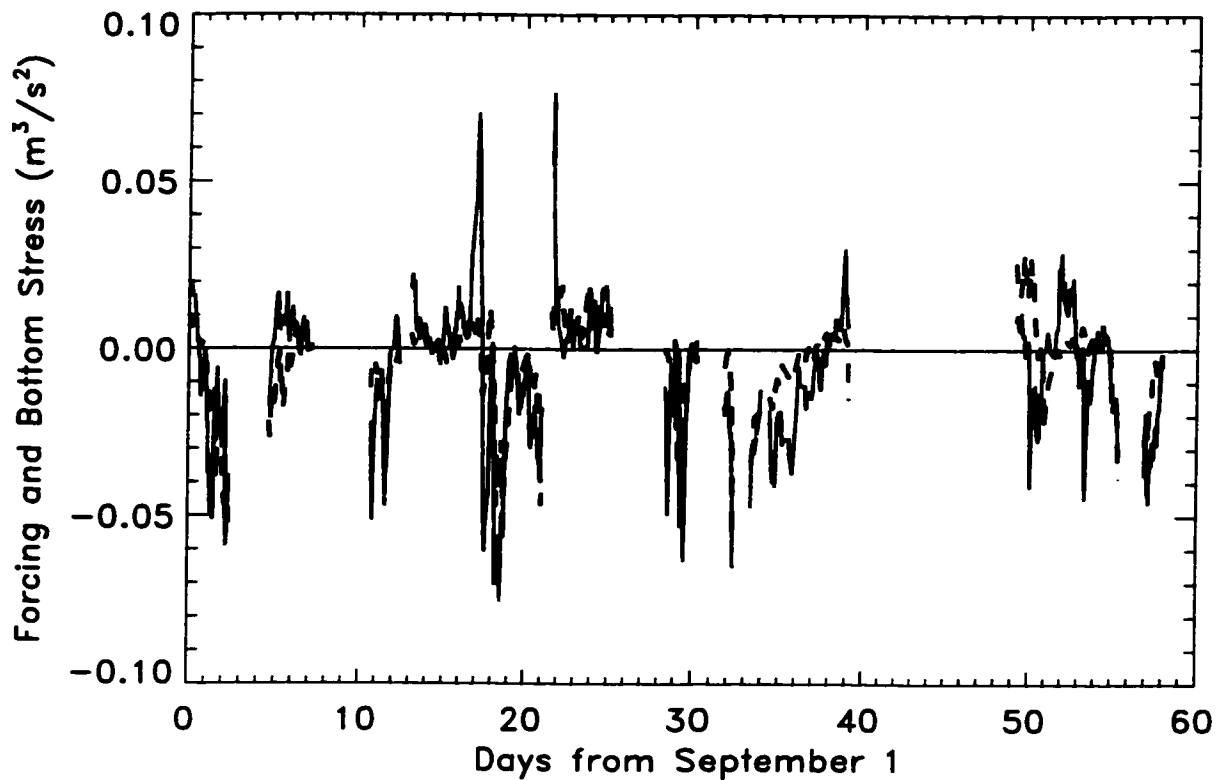


Figure II.9: Hourly wind forcing ($\int_{x_b}^{x_{sm}} (\tau_y^{\text{wind}} / \rho) dx$ solid curve) and bottom stress ($c_{f2} \int_{x_b}^{x_{sm}} \langle |\vec{u}|v \rangle dx$ with $c_{f2} = 0.00055$ dashed curve) integrated seaward of the surf zone versus time. The correlation coefficient squared $r^2 = 0.36$.

II.E Discussion

Other terms appearing in (II.4), but not in steady 1-D models (II.1), can be estimated in their integrated form with these data. The integration region extends to 8-m water depth, usually well seaward of the surf zone, and thus larger-scale inner shelf dynamics may be important over the instrument transect. For example, in 30-m water depth on the inner shelf of northern California, the alongshore barotropic pressure gradient (e.g. $-gh\partial\bar{\eta}/\partial y$) is an $O(1)$ term in the alongshore momentum balance [Lentz, 1994], and varies on alongshore length scales of $O(10-100 \text{ km})$. These gradients were estimated here using observations in 6-m water depth [Alessi *et al.*, 1996] as described in Appendix A. Assuming $\bar{\eta} \ll h$ and that $\partial\bar{\eta}/\partial y$ does not vary across the integration region, the cross-shore integral from shore to 8-m water depth of the pressure gradient is estimated as

$$-g\frac{\partial\bar{\eta}}{\partial y}\int_0^{x_{8m}} h dx$$

This barotropic pressure gradient is not dynamically important over the 750-m-long transect. It is usually a factor of 3 smaller than the wind forcing and is uncorrelated with any other dynamical terms. Alongshore baroclinic pressure gradients (not included in (II.4)) caused by Chesapeake Bay outflow can be significant on the inner shelf [Rennie, 1998] and might be important at times in the present momentum balances but cannot be quantified with this data set.

The integral of the acceleration term in (II.4) was also estimated. Using the continuity equation and assuming $\bar{\eta} \ll h$ and weak vertical variation of the alongshore current [Garcez Faria *et al.*, 1998], the term $(\bar{\eta} + h)\partial\bar{v}/\partial t$ can be transformed to $\partial[h\bar{v}]/\partial t$. The acceleration, estimated by finite differencing the hourly transport

$$\int_0^{x_{8m}} h\bar{v} dx$$

is uncorrelated ($r^2 = -0.0018$) with and has one fifth the rms value of the total forcing. The lack of correlation with forcing suggests that the acceleration estimate is contaminated by noise, but the low rms values imply that the acceleration

term is usually small. When the forcing changes rapidly (i.e. on September 21 in Figure II.7) the hourly averaged flow responds within about an hour (e.g. the current lags the forcing by no more than 1 temporal sample). This rapid response to large changes in forcing further suggests that the alongshore current is nearly always in frictional balance and that flow accelerations are negligible.

The statistical analysis in section 3 demonstrates that the 1-D integrated momentum balance from the shoreline to 8-m water depth (II.6) closes, indicating that over the entire instrumented transect the combined wind and wave forcing is balanced by the bottom stress. The closure does not necessarily imply that the 1-D momentum balance (II.1) holds locally, because 2-D terms in (II.4) (e.g. non-linear and alongshore pressure gradient) could be locally strong but change sign with cross-shore location such that their cross-shore integrals cancel. However, consistent cancellation seems unlikely to occur over the wide range of bathymetric and forcing conditions encountered during the 2-month experiment. Therefore the closure of the integrated momentum balance suggests that 2-D terms are typically small.

There are cases when the flow appears to be dominated by 2-D effects such as alongshore pressure gradients. For example, on October 16 (Figure II.10) the waves were energetic ($H_{sig} = 3$ m in 8-m water depth) but nearly normally incident (mean wave angle of 2°), so $-S_{yx}$ in 8-m water depth was small (-0.023 m³/s²). Wave breaking extended to 8-m water depth and was most intense about 150-200 m from shore (Figure II.10a), well offshore of the strongest currents ($\bar{v}_{max} = -0.49$ m/s near the shoreline, Figure II.10b). In contrast to the observations, 1-D models predict weak currents everywhere ($|\bar{v}| \leq 0.05$ m/s) for the small wave angles observed. Time-elapsed video images (R.A. Holman, personal communication, 1996) suggest the presence of strong alongshore depth variations, and the poststorm (October 18) bathymetry was two-dimensional with a large gap in the sandbar (e.g. Figure II.1). The observed alongshore current may have been feeding a rip current visually observed during the storm (E.B. Thornton, personal communica-

tion, 1997). In addition, numerical model results with bathymetry similar to that measured on October 18 demonstrate that 2-D effects can be important to the local alongshore momentum balance [*Sancho et al.*, 1995].

II.F Summary

The 1-D alongshore momentum balance, with a quadratic parameterization of the bottom stress, integrated from the shoreline to 8-m water depth closes ($r^2 = 0.87$) over a wide range of conditions. The closure suggests that the quadratic form (II.2) represents well the alongshore bottom stress and that on average the dynamics of the alongshore current are described by the 1-D momentum balance (II.1). Including the wind forcing statistically improves the integrated-to-8-m-depth momentum balance, demonstrating the importance of wind to nearshore circulation.

A spatially variable drag coefficient statistically improves the integrated-to-8-m-depth momentum balance. The surf zone drag coefficients inferred here are similar to those obtained by *Whitford and Thornton* [1996] and (for low bed roughness) *Garcez Faria et al.* [1998]. The cross-shore variation of c_f (0.0033 and 0.0010 within and seaward of the surf zone, respectively) may be associated with increased turbulence from breaking waves inside the surf zone [*Church and Thornton*, 1993] or cross-shore variations in time-averaged bed roughness [*Garcez Faria et al.*, 1998]. The cross-shore variation of c_f also is consistent with laboratory studies [*Cox et al.*, 1996].

In the surf zone, wind and wave forcing are balanced by the bottom stress. The wind forcing is statistically unimportant within the surf zone relative to the wave forcing but is an $O(1)$ term seaward of the surf zone. The seaward of the surf zone momentum balance between wind forcing and bottom stress does not close as well ($r^2 = 0.36$) as the surf zone momentum balance ($r^2 = 0.79$). Momentum balances on the inner shelf at Duck will be considered in detail elsewhere.

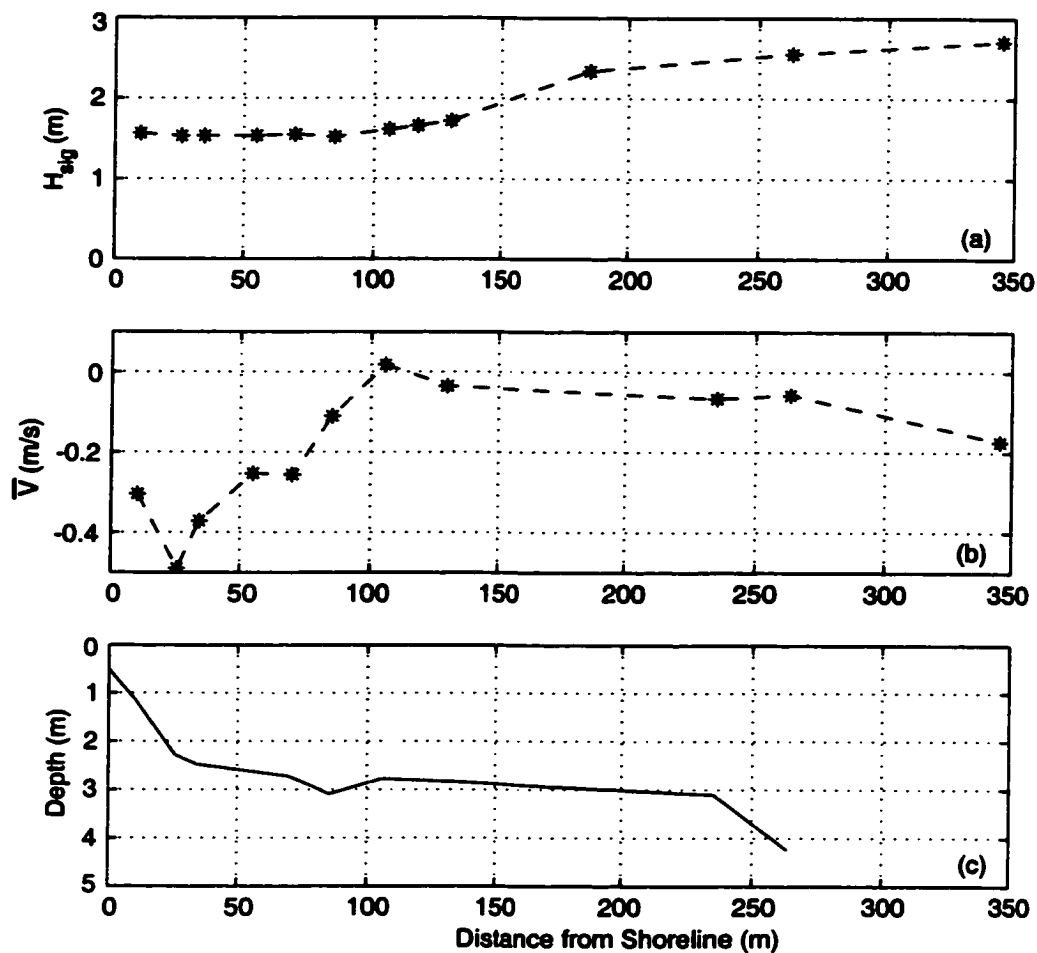


Figure II.10: (a) Significant wave height, (b) alongshore current \bar{v} , and (c) depth versus distance from the shoreline observed at 0500 eastern standard time October 16.

II.G Appendix A: Barotropic Pressure Gradient Estimates

The hourly averaged bottom pressure data acquired with a five-element, 60-km-long array in 6-m water depth centered at the FRF pier [Alessi *et al.*, 1996] was converted to sea surface elevation and demeaned with the 2-month average of each instrument. For each hour, the mean of the five sensors (a spatial mean) was removed, suppressing the large tidal signal with zero phase lag. An empirical orthogonal function decomposition was used to extract the dominant nonzero gradient mode of sea surface elevation from the remaining signal. The first eigenfunction contains 89% percent of the variance and represents a linear tilt in sea surface elevation. The gradient of this first eigenfunction multiplied by its temporal amplitude yields estimates of hourly alongshore sea surface gradients $\partial\eta/\partial y$.

II.H Appendix B: Surf Zone Width (x_b) Estimates

At each pressure sensor along the cross-shore transect the linear energy flux integrated from 0.04 to 0.3 Hz was calculated for each hour assuming shore-normal wave propagation. According to linear theory, on parallel depth contours the energy flux is conserved seaward of x_b , where wave breaking begins. However, measurement errors, inadequacies of linear theory, reflected wave energy, directional spreading, and irregular bathymetry cause considerable scatter in the energy flux estimates. Therefore a heuristic algorithm based on a combination of the decrease in energy flux relative to 8-m water depth, the local energy flux gradient, and time-elapsd video images (R.A. Holman, personal communication, 1996) was used to approximately define the location of the seaward edge of the surf zone x_b . Results that depend on x_b are insensitive to moving all estimates of x_b one sensor closer to shore but, in some cases, vary substantially when the x_b estimates are moved one sensor farther seaward.

II.I Appendix C: Cross-Shore Integration Method

Hourly cross-shore integrals such as

$$\int_{x_1}^{x_2} h\bar{v}dx \quad \int_{x_1}^{x_2} \langle |\bar{u}|v \rangle dx$$

where x_1 and x_2 represent cross-shore instrument locations, were estimated using the trapezoid rule between active sensors. When an instrument at the endpoint (i.e. at $x = x_1$ or $x = x_2$) was inactive, the integral was not computed, with one exception. If the starting point for the integration was the shoreline and the shallowest instrument was inactive, its value was set equal to that of the next offshore sensor. The transect-wide integral to 8-m water depth was estimated for 1176 of the 1440 hour-long records collected during the 2-month experiment. Integrals over the surf zone or the seaward of the surf zone region were estimated only when the outer edge of the surf zone x_b was < 230 m from the shoreline, to ensure sufficient coverage for the seaward of the surf zone integral. The above criteria were satisfied within the surf zone for 858 hours and outside the surf zone for 686 hours. A different current meter (displaced 40 m in the horizontal) was used for the integrations to x_{8m} after October 13, when the 8-m water depth sensor failed. The results are insensitive to which current meter was used when both were active. The degrees of freedom for computing confidence intervals were calculated by dividing the number of hours in the balance by the integral timescale (the time period over which observations are independent [Davis, 1976]). This timescale ranged from 12 to 15 hours, depending on the balance.

Acknowledgements

The array of current meters, sonar altimeters, and pressure sensors was deployed and maintained by staff from the Center for Coastal Studies. Britt Raubenheimer and Edith Gallagher helped collect the data. Excellent logistical support was provided by the U.S. Army Corps of Engineers Field Research Facility. We

thank Steve Lentz for providing the wind stress and the alongshore pressure array data, Rob Holman for providing video images, and Ed Thornton for constructive comments. This research was funded by the Office of Naval Research (Coastal Sciences Program) and the National Science Foundation (CooP Program). F.F. received a traineeship from the National Sea Grant College Program, National Oceanic and Atmospheric Administration, U.S. Department of Commerce, under grant NA36RG0537, project R/OE-31 through the California Sea Grant College, and the California State Resources Agency. The views expressed herein are those of the authors and do not necessarily reflect the views of NOAA or any of its subagencies.

This chapter, in full, is a reprint of Feddersen, F., R. T. Guza, S. Elgar, T. H. C. Herbers, Alongshore momentum balances in the nearshore. *J. Geophys. Res.*, **103**, 15667–15676, 1998. I was the primary researcher and author, and the co-authors listed in this publication directed and supervised the research which forms the basis of this chapter.

II.J References

- Alessi, C.A., S.J. Lentz, and J. Austin, Coastal ocean processes inner-shelf study: Coastal and moored physical oceanographic measurements. *Woods Hole Oceanogr. Inst. Tech. Rep. WHOI-96-6*, 154 pp., Woods Hole Oceanogr. Inst., Woods Hole, Mass., 1996.
- Battjes, J.A., Radiation stresses in short-crested waves, *J. Mar. Res.*, **30**, 56–64, 1972.
- Bowen, A.J., The generation of longshore currents on a plane beach, *J. Mar. Res.*, **27**, 206–215, 1969.
- Church, J.C., and E.B. Thornton, Effects of breaking wave induced turbulence within a longshore current model, *Coastal Eng.*, **20**, 1–28, 1993.
- Cox, D.T., N. Kobayashi, and A. Okayama, Bottom stress in the surf zone, *J. Geophys. Res.*, **101**, 14,337–14,348, 1996.
- Davis, R.E., Predictability of sea surface temperature and sea level pressure anomalies over the North Pacific Ocean, *J. Phys. Oceanogr.*, **6**, 249–266, 1976.
- Dally, W.R., and C.A. Brown, A modeling investigation of the breaking wave roller with application to cross-shore currents, *J. Geophys. Res.*, **100**, 24,873–24,883, 1995.
- Elgar, S., T.H.C. Herbers, and R.T. Guza, Reflection of ocean surface gravity waves from a natural beach, *J. Phys. Oceanogr.*, **24**, 1503–1511, 1994.
- Feddersen, F., R.T. Guza, S. Elgar, and T.H.C. Herbers, Cross-shore structure of longshore currents during Duck94, in *Proc. 25th Int. Coastal Engineering Conf.*, pp. 3666–3679, Am. Soc. of Civ. Eng., New York, 1996.
- Gallagher, E.L., W. Boyd, S. Elgar, R.T. Guza, and B. Woodward, Performance of a sonar altimeter in the nearshore, *Mar. Geol.*, **133**, 241–248, 1996.
- Gallagher, E.L., S. Elgar, and R.T. Guza, Observations of sand bar evolution on a natural beach, *J. Geophys. Res.*, **103**, 3203–3215, 1998.
- Garcez Faria, A.F., E.B. Thornton, T.P. Stanton, C.V. Soares, and T.C. Lippmann, Vertical profiles of longshore currents and related bed shear stress and bottom roughness, *J. Geophys. Res.*, **103**, 3217–3232, 1998.
- Guza, R.T., E.B. Thornton, and N. Christensen Jr., Observations of steady longshore currents in the surf zone, *J. Phys. Oceanogr.*, **16**, 1959–1969, 1986.

- Henderson, F.M., *Open Channel Flow*, Macmillan, Indianapolis, Indiana, 1966.
- Kuik, A.J., G.P. van Vledder, and L.H. Holthuijsen, A method for the routine analysis of pitch-and-roll buoy wave data, *J. Phys. Oceanogr.*, **18**, 1020–1034, 1988.
- Large, W.G., and S. Pond, Open ocean momentum flux measurements in moderate to strong winds, *J. Phys. Oceanogr.*, **11**, 324–36, 1981.
- Lentz, S.J., Current dynamics over the northern California inner shelf, *J. Phys. Oceanogr.*, **24**, 2461–2478, 1994.
- Lippmann, T.C., and R.A. Holman, The spatial and temporal variability of sand bar morphology, *J. Geophys. Res.*, **95**, 11,575–11,590, 1990.
- Long, C.E., Index and bulk parameters for frequency-direction spectra measured at CERC Field Research Facility, June 1994 to August 1995, *Misc. Pap. CERC-96-6*, U.S. Army Eng. Waterw. Exp. Stn., Vicksburg, Miss., 1996.
- Longuet-Higgins, M.S., Longshore currents generated by obliquely incident sea waves, 1, *J. Geophys. Res.*, **75**, 6778–6789, 1970.
- Longuet-Higgins, M.S., and R.W. Stewart, Radiation stress in water waves: A physical discussion with application, *Deep Sea Res.*, **11**, 529–563, 1964.
- Mei, C.C., *The Applied Dynamics of Ocean Surface Waves*, World Sci., River Edge, N.J., 1989.
- Putrevu, U., J. Oltman-Shay, and I.A. Svendsen, Effect of alongshore nonuniformities on longshore current predictions, *J. Geophys. Res.*, **100**, 16,119–16,130, 1995.
- Reniers, A., E.B. Thornton, and T.C. Lippmann, Longshore currents over barred beaches. in *Coastal Dynamics '95*, pp. 413–424, Am. Soc. of Civ. Eng., New York, 1995.
- Rennie, S.E., Wind interaction with buoyant plumes on the inner continental shelf, Ph.D. dissertation, 174 pp., Sch. of Mar. Sci., Coll. of William and Mary, Gloucester Point, Va., 1998.
- Rieder, K.F., J.A. Smith, and R.A. Weller, Some evidence of colinear wind stress and wave breaking, *J. Phys. Oceanogr.*, **26**, 2519–2524, 1996.
- Sancho, F.E., I.A. Svendsen, A.R. Van Dongeren, and U. Putrevu, Longshore nonuniformities of nearshore currents, in *Coastal Dynamics '95*, pp. 425–436, Am. Soc. of Civ. Eng., New York, 1995.

- Slinn, D.N., J.S. Allen, P.A. Newberger, and R.A. Holman, Nonlinear shear instabilities of alongshore currents over barred beaches, *J. Geophys. Res.*, **103**, 18,357–18379, 1998.
- Smith, J.M., M. Larson, and N.C. Kraus, Longshore current on a barred beach: Field measurements and calculations, *J. Geophys. Res.*, **98**, 22,717–22,731, 1993.
- Svendsen, I.A., Wave heights and set-up in a surf zone, *Coastal Eng.*, **8**, 303–329, 1984.
- Svendsen, I.A., and U. Putrevu, Nearshore mixing and dispersion, *Proc. R. Soc. London, Ser. A*, **445**, 561–576, 1994.
- Thornton, E.B., Variation of longshore current across the surf zone, in *Proc. 12th Int. Coastal Engineering Conf.*, pp. 291–308, Am. Soc. of Civ. Eng., New York, 1970.
- Thornton, E.B., and R.T. Guza, Transformations of wave height distribution, *J. Geophys. Res.*, **88**, 5925–5938, 1983.
- Thornton, E.B., and R.T. Guza, Surf zone longshore currents and random waves: Field data and models, *J. Phys. Oceanogr.*, **16**, 1165–1178, 1986.
- Whitford, D.J., and E.B. Thornton, Comparison of wind and wave forcing of longshore currents, *Cont. Shelf. Res.*, **13**, 1205–1218, 1993.
- Whitford, D.J., and E.B. Thornton, Bed shear stress coefficients for longshore currents over a barred profile, *Coastal Eng.*, **27**, 243–262, 1996.

Chapter III

Alongshore Bottom Stress Parameterizations

III.A Abstract

The time-averaged alongshore bottom stress is an important component of nearshore circulation models. In a widely accepted formulation, the bottom stress is proportional to $\langle |\vec{u}|v \rangle$, the time average of the product of the instantaneous velocity magnitude $|\vec{u}|$ and the instantaneous alongshore velocity component v . Both mean and fluctuating (owing to random, directionally spread waves) velocities contribute to $\langle |\vec{u}|v \rangle$. However, direct estimation of $\langle |\vec{u}|v \rangle$ requires a more detailed specification of the velocity field than is usually available, so the term $\langle |\vec{u}|v \rangle$ is parameterized. Here, direct estimates of $\langle |\vec{u}|v \rangle$ based on time series of near-bottom currents observed between the shoreline and 8-m water depth are used to test the accuracy of $\langle |\vec{u}|v \rangle$ parameterizations.

Common $\langle |\vec{u}|v \rangle$ parameterizations that are linear in the mean alongshore current underestimate $\langle |\vec{u}|v \rangle$ by roughly a factor of 2-3 for moderately strong alongshore currents, resulting in overestimation of a drag coefficient determined by fitting modeled (with a linearized bottom stress) to observed alongshore currents. A parameterization based a joint-Gaussian velocity field with the ob-

served velocity statistics gives excellent agreement with the directly estimated $\langle |\vec{u}|v \rangle$. The joint-Gaussian parameterization allows analytic investigation of the statistical properties of the velocity field that govern $\langle |\vec{u}|v \rangle$. Except for the weakest flows, $\langle |\vec{u}|v \rangle$ depends strongly on the mean alongshore current and the total velocity variance, but depends only weakly on the mean wave angle, wave directional spread, and mean cross-shore current. Several other nonlinear parameterizations of $\langle |\vec{u}|v \rangle$ are shown to be more accurate than the linear parameterizations, and are adequate for many modeling purposes.

III.B Introduction

The time-averaged alongshore bottom stress τ_y^b plays a crucial role in the dynamics of mean alongshore currents in the nearshore. A commonly used stress formulation is [Longuet-Higgins, 1970; Grant and Madsen, 1979; Battjes, 1988; Garcez-Faria et al., 1998; Feddersen et al., 1998, and many others]

$$\tau_y^b = \rho c_f \langle |\vec{u}|v \rangle, \quad (\text{III.1})$$

where $\langle \cdot \rangle$ represents a time average over many wave periods, ρ is the water density, and c_f is a nondimensional drag coefficient. The total instantaneous horizontal velocity vector $|\vec{u}|$ and the instantaneous alongshore velocity v are evaluated near the seafloor, but above the bottom boundary layer. Mean and fluctuating velocity components contribute to the nonlinear term $\langle |\vec{u}|v \rangle$.

Although widely accepted as valid, the stress form (III.1) usually is parameterized in nearshore circulation models because estimation of $\langle |\vec{u}|v \rangle$ requires detailed specification of the fluctuating velocity field over a broad range of time scales (e.g. sea, swell, infragravity, and shear waves). Analogous stress parameterizations are necessary in other oceanographic contexts, including mean flow in the presence of tidal currents [Bowden, 1953] and large scale ocean circulation [Rooth, 1972].

Here, the accuracy of several linear and nonlinear parameterizations of $\langle |\bar{u}|v \rangle$ widely used in nearshore circulation models (reviewed in section 2) is tested with an extensive field data set described in section 3. The $\langle |\bar{u}|v \rangle$ term is calculated directly from the observed velocity time series and compared with parameterizations based on the velocity statistics estimated from the observations. The dependence of c_f on the flow environment and bottom roughness [e.g. *Grant and Madsen*, 1979; *Garcez-Faria et al.*, 1998] is not investigated here.

As discussed in section 4, parameterizations linear in the mean alongshore current often are inaccurate because the underlying assumptions (e.g. weak-currents) are violated. Estimates of $\langle |\bar{u}|v \rangle$ based on the assumption of an isotropic Gaussian velocity field [*Wright and Thompson*, 1983] are generalized to a joint-Gaussian velocity field corresponding to arbitrary wave-directional distributions. Although this accurate parameterization requires a more detailed specification of velocity field statistics than is generally available, it enables identification of the nondimensional variables controlling $\langle |\bar{u}|v \rangle$, providing a basis for further simplification. Several existing nonlinear parameterizations and special cases of the joint-Gaussian parameterization are found to be accurate. The mean alongshore current and total velocity variance are the components critical to parameterizing $\langle |\bar{u}|v \rangle$ accurately. The consequences of neglecting infragravity (< 0.05 Hz) velocity fluctuations in (III.1) and of using different parameterizations of (III.1) in a simple alongshore current model are discussed in section 5. Results are summarized in section 6.

III.C Bottom Stress Parameterizations

The weak-current, small-angle parameterization of $\langle |\bar{u}|v \rangle$ is linear in the mean alongshore current, and therefore often is used in models of surf zone circulation [e.g. *Wu et al.*, 1985; *Özkan-Haller and Kirby*, 1999]. The cross-shore u

and alongshore v velocities are decomposed into mean and fluctuating components

$$u = \bar{u} + u', \quad v = \bar{v} + v',$$

with variances σ_u^2 and σ_v^2 , respectively. The total velocity variance $\sigma_T^2 = \sigma_u^2 + \sigma_v^2$. Assuming $\bar{u} = 0$, and applying the weak-current ($|\bar{v}| \ll \sigma_T$) and small-angle ($\sigma_v \ll \bar{v}$) approximations yields

$$\langle |\bar{u}|v \rangle = \langle |u'| \rangle \bar{v} \quad (\text{III.2})$$

For monochromatic and unidirectional waves with period T (radian frequency ω) and wave velocity amplitude u_0 propagating at small angle θ relative to normal incidence,

$$u' = u_0 \cos(\theta) \cos(\omega t), \quad v' = u_0 \sin(\theta) \cos(\omega t),$$

(III.2) yields [Longuet-Higgins, 1970; Thornton, 1970]

$$\langle |\bar{u}|v \rangle = \langle |u'| \rangle \bar{v} = u_0 \bar{v} \cdot \frac{1}{T} \int_T |\cos(\omega t)| dt = \frac{2}{\pi} u_0 \bar{v} = \frac{2\sqrt{2}}{\pi} \sigma_T \bar{v}. \quad (\text{III.3})$$

Thornton and Guza [1986] extended (III.2) to unidirectional waves with a narrow frequency spectrum and Rayleigh distributed u_0 [Longuet-Higgins, 1952] with probability density function

$$P(u_0) = \frac{u_0}{\sigma_T^2} \exp\left(-\frac{u_0^2}{2\sigma_T^2}\right). \quad (\text{III.4})$$

Using (III.4) in (III.2) yields

$$\langle |u'| \rangle \bar{v} = E[|u'|] \bar{v} = \int_0^\infty u_0 P(u_0) du_0 \cdot \frac{1}{T} \int_T |\cos(\omega t)| dt \bar{v} = \sqrt{\frac{2}{\pi}} \sigma_T \bar{v} = 0.798 \sigma_T \bar{v} \quad (\text{III.5})$$

where $E[\cdot]$ is the expected value. Note that (III.5) can also be derived from the less restrictive assumption that the wave orbital velocities are Gaussian distributed [Longuet-Higgins, 1952], i.e.

$$\langle |u'| \rangle \bar{v} = \frac{\bar{v}}{\sqrt{2\pi}\sigma_T} \int_{-\infty}^{\infty} |u'| \exp\left(-\frac{u'^2}{2\sigma_T^2}\right) du' = \sqrt{\frac{2}{\pi}} \sigma_T \bar{v}.$$

Other weak-current linearized forms for $\langle |\vec{u}|v \rangle$ follow from different assumptions about the fluctuating velocity field. For example, *Liu and Dalrymple* [1978] relaxed the small angle assumption used in (III.3) and showed (for monochromatic waves) that

$$\langle |\vec{u}|v \rangle = \frac{2\sqrt{2}}{\pi} \sigma_T \bar{v} (1 + \sin^2 \theta). \quad (\text{III.6})$$

Wave obliquity thus increases $\langle |\vec{u}|v \rangle$ relative to small-angles (III.3).

Rayleigh friction,

$$\langle |\vec{u}|v \rangle = \mu \bar{v} \quad (\text{III.7})$$

where μ is a constant dimensional drag coefficient, has been used in models of surf zone alongshore currents [*Bowen*, 1969], shear waves [e.g. *Dodd et al.*, 1992; *Allen et al.*, 1996; *Slinn et al.*, 1998; *Feddersen*, 1998], and shelf circulation [e.g. *Lentz and Winant*, 1986]. Rayleigh friction follows from assuming a constant σ_T in (III.5).

Liu and Dalrymple [1978] parameterized $\langle |\vec{u}|v \rangle$ for strong currents ($|\bar{v}|/\sigma_T \gg 1$) and monochromatic unidirectional waves with arbitrary θ . For $\bar{u} = 0$,

$$\langle |\vec{u}|v \rangle = |\bar{v}| \bar{v} + \frac{\text{sgn}(\bar{v}) \sigma_T^2}{2} (1 + \sin^2 \theta) \quad (\text{III.8})$$

where $\text{sgn}(\bar{v})$ is the sign of \bar{v} . *Ebersole and Dalrymple* [1980] introduced a general formulation for linear, unidirectional, monochromatic waves. With $\bar{u} = 0$, the result (known hereinafter as ED80) is

$$\langle |\vec{u}|v \rangle = \frac{1}{T} \int_T [u_0^2 \cos^2(\omega t) + 2\bar{v}u_0 \sin(\theta) \cos(\omega t) + \bar{v}^2]^{1/2} [\bar{v} + u_0 \sin(\theta) \cos(\omega t)] dt. \quad (\text{III.9})$$

Thornton and Guza [1986] extended ED80 to a narrow frequency spectrum. Evaluating (III.9) for each orbital wave velocity amplitude u_0 yields $\overline{|\vec{u}|v}(u_0)$, and the expected value over the Rayleigh distributed u_0 is (known hereinafter as TG86)

$$\langle |\vec{u}|v \rangle = E[\overline{|\vec{u}|v}(u_0)] = \int_0^\infty \overline{|\vec{u}|v}(u_0) \cdot P(u_0) du_0 \quad (\text{III.10})$$

where $P(u_0)$ is the Rayleigh probability density function (III.4). Both ED80 and TG86 are nonlinear in \bar{v} and must be integrated numerically.

On a planar beach with maximum observed alongshore current $\bar{v}_{\max} \approx 0.6$ m/s, Thornton and Guza [1986] showed that 1-D model solutions with the linear (III.5) and the nonlinear TG86 (III.10) parameterizations ($\bar{u} = 0$) both approximately reproduce the observed cross-shore variation of $\bar{v}(x)$. However, the best-fit values of the drag coefficient c_f with TG86 was 0.6-0.8 of the c_f using (III.5). Thornton and Guza [1986] suggest the c_f values differed because $|\bar{v}|/\sigma_T$ was $O(1)$, violating the weak-current assumption underlying (III.5). On a barred beach with $\bar{v}_{\max} \approx 1.5$ m/s, $\bar{v}(x)$ solutions with both (III.5) and TG86 differs substantially, even using c_f values that yield the same modeled \bar{v}_{\max} [Church and Thornton, 1993]. In this case, the weak-current assumption likely was violated more severely than the cases with weaker \bar{v}_{\max} considered by Thornton and Guza [1986]. These differences suggest that the weak-current linearized parameterization (III.5) is inaccurate. Although weak currents and small angles are not assumed in ED80 and TG86, the mean cross-shore current and directional spreading of waves are neglected, and the errors due to these assumptions are not understood well.

Wright and Thompson [1983] investigated the accuracy of the linearized parameterization in the special case of an isotropic ($\sigma_u = \sigma_v = \sigma_T/\sqrt{2}$), uncorrelated Gaussian fluctuating velocity field, where

$$\langle |\bar{u}|v \rangle = E[|\bar{u}|v] = \iint_{-\infty}^{\infty} (u'^2 + v'^2 + 2\bar{v}v' + \bar{v}^2)^{1/2} (\bar{v} + v') P(u', v') du' dv', \quad (\text{III.11})$$

with the probability density function

$$P(u', v') = \frac{1}{2\pi\sigma_u^2} \exp \left[-\frac{1}{2\sigma_u^2} (u'^2 + v'^2) \right].$$

Although $\langle |\bar{u}|v \rangle$ is a function of two parameters, \bar{v} and σ_T , the ratio $\langle |\bar{u}|v \rangle / \sigma_T \bar{v}$ is a function of only $|\bar{v}|/\sigma_T$. Integrating (III.11) numerically, Wright and Thompson [1983] showed that for $0 < |\bar{v}|/\sigma_T \leq 1$, $\langle |\bar{u}|v \rangle / \sigma_T \bar{v}$ is relatively constant and

varies by 23% from its weak-current value of $0.75\sqrt{\pi} = 1.33$. Note that the small-angle random wave weak-current limit is 0.798. *Wright and Thompson* [1983] showed that the ratio $\langle |\vec{u}|v \rangle / \sigma_T \bar{v}$ for an isotropic, uncorrelated Gaussian velocity field is represented well (maximum error of 2%) for all values of $|\bar{v}|/\sigma_T$ by an empirical form (known hereinafter as WT83)

$$\frac{\langle |\vec{u}|v \rangle}{\sigma_T \bar{v}} = [\alpha^2 + (\bar{v}/\sigma_T)^2]^{1/2} \quad (\text{III.12})$$

with $\alpha = 1.33$. WT83 has the correct weak-current limit for an isotropic wave field, and the strong-current limit ($|\bar{v}|/\sigma_T \rightarrow \infty$)

$$\langle |\vec{u}|v \rangle = |\bar{v}| \bar{v} + \frac{1}{2} \alpha^2 \text{sgn}(\bar{v}) \sigma_T^2 \quad (\text{III.13})$$

has the same form as the strong-current parameterization for monochromatic unidirectional waves (III.8) [*Liu and Dalrymple*, 1978].

Naturally occurring wave-induced velocity fields are neither unidirectional nor isotropic. The formulation of *Wright and Thompson* [1983] is generalized here to include velocity fluctuations with arbitrary directional-distributions by assuming u and v are joint-Gaussian distributed random variables

$$E[|\vec{u}|v] = \int \int_{-\infty}^{\infty} (u^2 + v^2)^{1/2} v P(u, v) du dv. \quad (\text{III.14})$$

The joint probability density function $P(u, v)$, given in Appendix A, is a function of \bar{u} , \bar{v} , σ_u , σ_v , and the correlation coefficient ρ_{uv} ,

$$\rho_{uv} = \frac{\langle u'v' \rangle}{\sigma_u \sigma_v}.$$

The velocity moments σ_u , σ_v , and ρ_{uv} are related to the mean angle $\bar{\theta}$ and spread σ_θ for a directionally distributed wave field [*Kuik et al.*, 1988; *Herbers et al.*, 1999]. A unidirectional wave field corresponds to $\sigma_\theta^2 = 0$, $|\rho_{uv}| = 1$, and $\tan(|\bar{\theta}|) = \sigma_v/\sigma_u$, an isotropic wave field corresponds to $\rho_{uv} = 0$ and $\sigma_v = \sigma_u$, and a wave field spread symmetrically about normal incidence ($\bar{\theta} = 0$) corresponds to $\rho_{uv} = 0$, $\sigma_v \neq 0$, and

$$\sigma_\theta^2 = \frac{\sigma_v^2}{\sigma_u^2 + \sigma_v^2}.$$

	\bar{v} (m/s)	σ_T (m/s)	$ \bar{v} /\sigma_T$	\bar{u}/σ_T	σ_v/σ_u	ρ_{uv}	$\theta(^{\circ})$	$\sigma_{\theta} (^{\circ})$
Mean	0.03	0.35	0.33	-0.1	0.41	-0.11	-4.7	19.4
Std. Dev.	0.22	0.17	0.30	0.17	0.09	0.19	10.5	3.6
Max	1.74	0.96	2.79	1.47	1.21	0.85	44.5	51.7
Min	-1.60	0.05	0.00	-1.85	0.21	-0.92	-44.3	9.9

Table III.1: Statistics of the velocity field and the associated wave directional properties. Positive u and v correspond to onshore and southerly flow, respectively.

In general, (III.14) must be evaluated numerically (Appendix A). Special cases depend on fewer variables and are easier to evaluate. When $|\rho_{uv}| = 1$ (i.e. $\sigma_{\theta} = 0$, a unidirectional assumption similar to TG86), the double integral in (III.14) collapses to a single integral (III.21). For the case of small angles ($\sigma_v = 0$) and $\bar{u} = 0$, a closed form solution exists (Appendix C, known hereinafter as SA).

Estimates of $E[|\bar{u}|v]/\sigma_T\bar{v}$ based on (III.14) are a function of four nondimensional parameters (\bar{v}/σ_T , \bar{u}/σ_T , σ_v/σ_u , ρ_{uv}). Weak-currents ($|\bar{v}|/\sigma_T$) and $\bar{u}/\sigma_T = 0$ result in $\langle |\bar{u}|v \rangle / \sigma_T\bar{v} = \alpha(\sigma_v/\sigma_u, \rho_{uv})$ (III.4), a function of two parameters (equivalent to $\bar{\theta}$ and σ_{θ}). For unidirectional waves ($|\rho_{uv}| = 1$), the closed form expression (III.5) shows that the increase in $\langle |\bar{u}|v \rangle / \sigma_T\bar{v} = \alpha(\sigma_v/\sigma_u)$ owing to wave obliquity is $1 + \sin^2 \theta$, similar to the dependence for monochromatic waves (III.6).

III.D Field Observations

Field observations were collected near Duck, N.C. on a barrier island exposed to the Atlantic Ocean during the Duck94 (September-October 1994 [Elgar *et al.*, 1997; Gallagher *et al.*, 1998; Garcez-Faria *et al.*, 1998; Feddersen *et al.*, 1998; Thornton *et al.*, 1998; Herbers *et al.*, 1999; and elsewhere]) and SandyDuck (August-November 1997 [Elgar *et al.*, 1999]) field experiments. Data used here were acquired from 13 current meters deployed on a cross-shore transect extending 750-m from near the shoreline to 8-m water depth during Duck94, and from a 2-D array of 26 current meters spanning 350 m in the cross-shore and 200 m in the

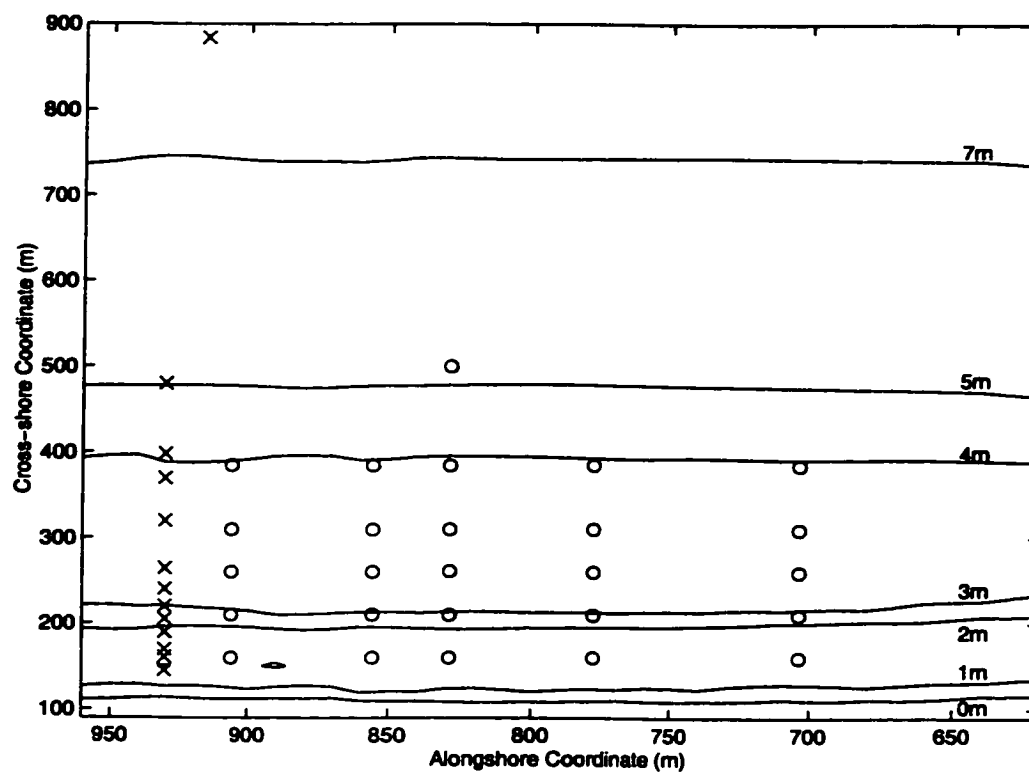


Figure III.1: Locations of the 13 Duck94 (x) and 26 SandyDuck (o) current meters used in this study. The U. S. Army Corps of Engineers Field Research Facility (FRF) coordinate system is used. Bathymetry from October 2, 1997 is contoured in units of meters below mean sea level.

alongshore during SandyDuck (Figure III.1). The current meters were raised or lowered as the bed level changed to maintain an elevation between approximately 0.4 to 1.0 m above the seafloor. The sensors closest to shore often were exposed at low tide and therefore inactive. Over all the sensors, the significant wave height ranged from approximately 0.2 to 4 m, the peak wave period from 5 to 12 seconds, and the wave directional properties are given in Table III.1.

Current meter data acquired at 2 Hz were processed into hourly-averaged estimates of \bar{v} , \bar{u} , σ_u , σ_v , $\langle |\vec{u}|v \rangle$, and ρ_{uv} resulting in 70,099 estimates of each variable, 15,072 from Duck94 and 55,027 from SandyDuck. The estimated hourly statistics contain contributions from shear and infragravity waves, as well as from sea and swell. Statistics of \bar{v} , σ_T , $|\bar{v}|/\sigma_T$, \bar{u}/σ_T , σ_v/σ_u , ρ_{uv} (Table III.1) show that the assumption of weak-currents ($|\bar{v}|/\sigma_T \ll 1$), small-angles ($\sigma_v/\sigma_u \ll 1$), negligible \bar{u} , and unidirectional waves ($|\rho_{uv}| = 1$) used in parameterizations of $\langle |\vec{u}|v \rangle$ often are violated.

III.E Parameterizations

III.E.1 Linear Parameterization

A linearized parameterization, based on the weak-current and small-angle parameterization (III.5),

$$\langle |\vec{u}|v \rangle = a \sigma_T \bar{v} \quad (\text{III.15})$$

where a is a best-fit coefficient, does not describe accurately the observed relationship between $\langle |\vec{u}|v \rangle$ and $\sigma_T \bar{v}$ (Figure III.2a). There is considerable scatter in the observed $\langle |\vec{u}|v \rangle$ for $|\sigma_T \bar{v}| > 0.2 \text{ m}^2/\text{s}^2$, and a systematic nonlinear trend (e.g. $\langle |\vec{u}|v \rangle$ increases nonlinearly for the largest values of $\sigma_T \bar{v}$). The Rayleigh friction parameterization (III.7) is even less accurate (Figure III.2b), with pronounced systematic deviations and a lower skill than (III.15). With moderately strong flows the errors for both parameterizations (with best-fit slopes) are roughly a factor of two.

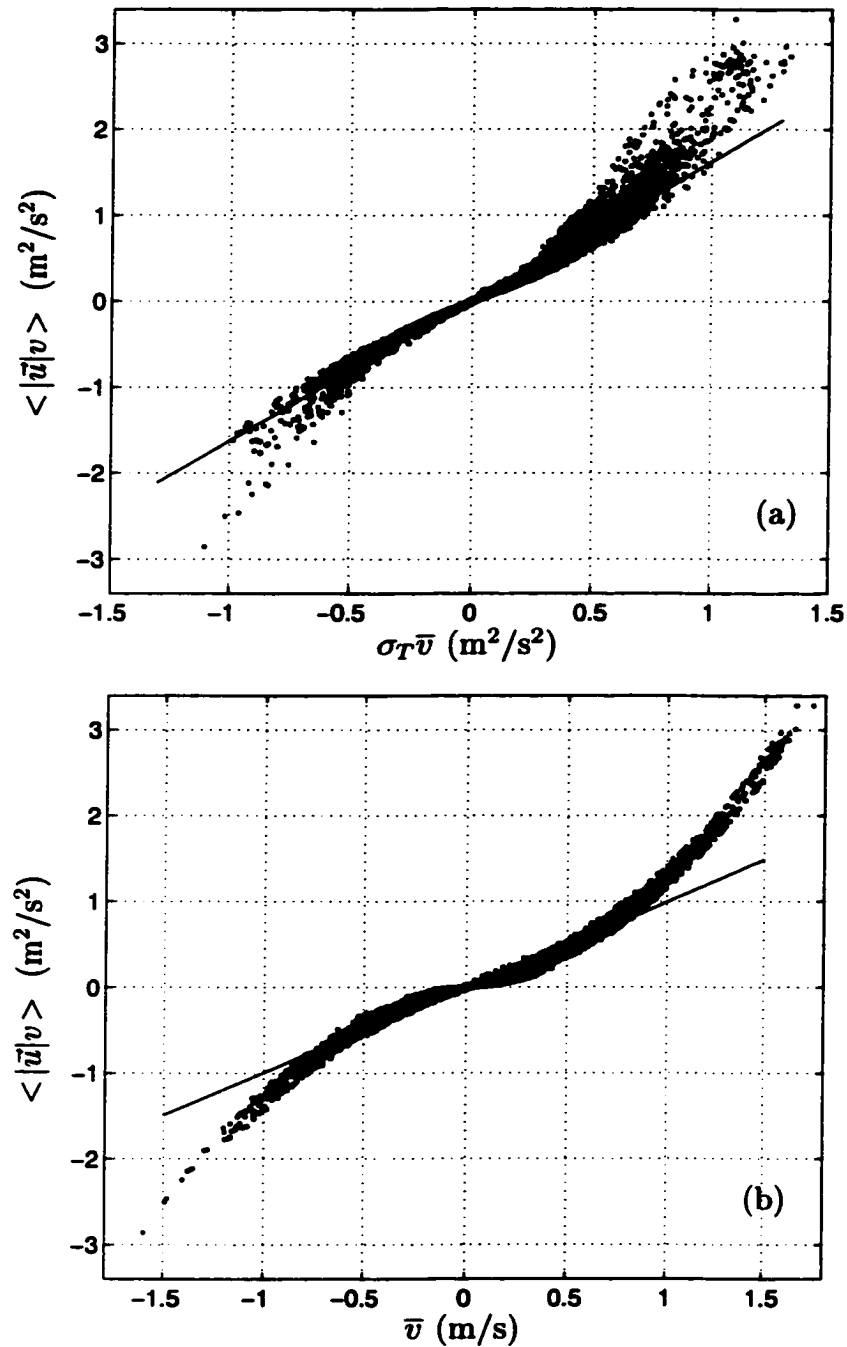


Figure III.2: (a) Observed $\langle |\bar{u}|v \rangle$ versus $\sigma_T \bar{v}$. The solid line is the least-squares best-fit (slope $a = 1.62$ and skill $r^2 = 0.94$). (b) Observed $\langle |\bar{u}|v \rangle$ versus \bar{v} . The solid line is the least-squares best-fit (slope = 0.99 m/s and skill $r^2 = 0.88$). Each panel has 70,099 data points.

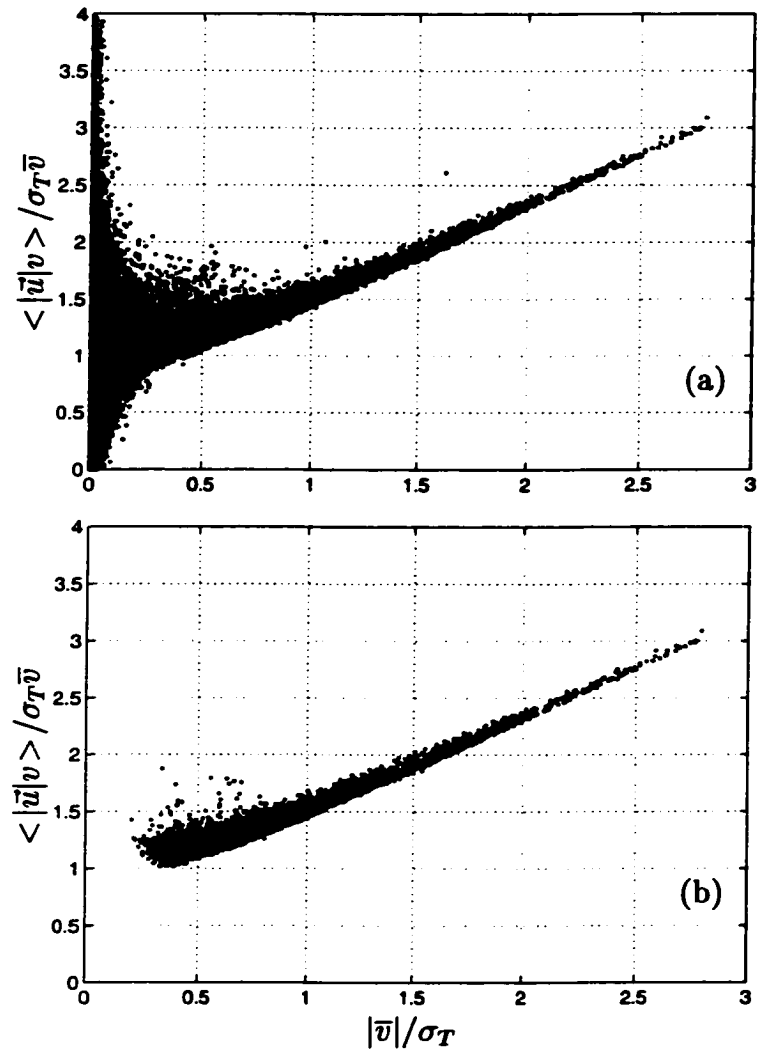


Figure III.3: Observed $\langle |\vec{u}|v \rangle / \sigma_T \bar{v}$ versus $|\vec{v}|/\sigma_T$. (a) All data points in the region $0 < (\langle |\vec{u}|v \rangle / \sigma_T \bar{v}) < 4$. (b) The subset of data where $|\langle |\vec{u}|v \rangle| > 0.2 \text{ m}^2/\text{s}^2$ (7857 data points).

The ratio $\langle |\vec{u}|v \rangle / \sigma_T \bar{v}$ (constant if (III.15) were correct) depends systematically on $|\bar{v}|/\sigma_T$ (Figure III.3). For values of $|\bar{v}|/\sigma_T > 0.5$, $\langle |\vec{u}|v \rangle / \sigma_T \bar{v}$ increases approximately linearly with $|\bar{v}|/\sigma_T$, consistent with the expectation that $\langle |\vec{u}|v \rangle \sim |\bar{v}| \bar{v}$ for strong currents. The linear relationship between $\langle |\vec{u}|v \rangle / \sigma_T \bar{v}$ and $|\bar{v}|/\sigma_T$ is clearer when cases with $|\langle |\vec{u}|v \rangle| < 0.2 \text{ m}^2/\text{s}^2$ are excluded (Figure III.3b). For small values of $|\bar{v}|/\sigma_T$ (i.e. < 0.5), where the weak-current approximation (III.15) might be expected to be valid, $\langle |\vec{u}|v \rangle / \sigma_T \bar{v}$ is scattered over a wide range, and many values of $\langle |\vec{u}|v \rangle / \sigma_T \bar{v}$ are offscale in Figure III.3a. As shown below, much of this scatter reflects terms involving the mean cross-shore flow \bar{u} and directional spread that are neglected in the weak-current, small-angle parameterization, but are important when \bar{v} is small. Although the relative errors in (III.15) for small $|\bar{v}|/\sigma_T$ are often large (Figure III.3a), the absolute error is small (Figure III.2a) because $\langle |\vec{u}|v \rangle$ usually is small when $|\bar{v}|/\sigma_T \rightarrow 0$ (Figure III.3b).

III.E.2 Joint-Gaussian Parameterization

The joint-Gaussian expected-value parameterization (III.14) is accurate, as demonstrated by the close correspondence between observed $\langle |\vec{u}|v \rangle$ values obtained directly from the velocity time series and $E[|\vec{u}|v]$ using observed values of \bar{u} , \bar{v} , σ_u , σ_v , and ρ_{uv} (Figure III.4a). Although $\langle |\vec{u}|v \rangle / E[|\vec{u}|v]$ is still scattered for small $|\bar{v}|/\sigma_T$, the scatter is reduced relative to the linearized parameterization (compare Figure III.4b with Figure III.3a). One possible cause for the remaining scatter for low $|\bar{v}|/\sigma_T$ in Figure III.4b is the sensitivity of $E[|\vec{u}|v]/\sigma_T \bar{v}$ for small $|\bar{v}|/\sigma_T$ to a non-zero skewness (Appendix B). The velocity skewness usually is non-zero in the surf zone due to nonlinearities in the wave field [Guza and Thornton, 1985].

Based on the agreement between $E[|\vec{u}|v]$ and $\langle |\vec{u}|v \rangle$, $E[|\vec{u}|v]$ is used below as a proxy for $\langle |\vec{u}|v \rangle$ in the surf zone. The dependence of $E[|\vec{u}|v]/\sigma_T \bar{v}$ on \bar{v}/σ_T , \bar{u}/σ_T , σ_v/σ_u , and ρ_{uv} are used to explain the distribution of data in Figure III.3. The observed ranges of these quantities at Duck (Table III.1) are

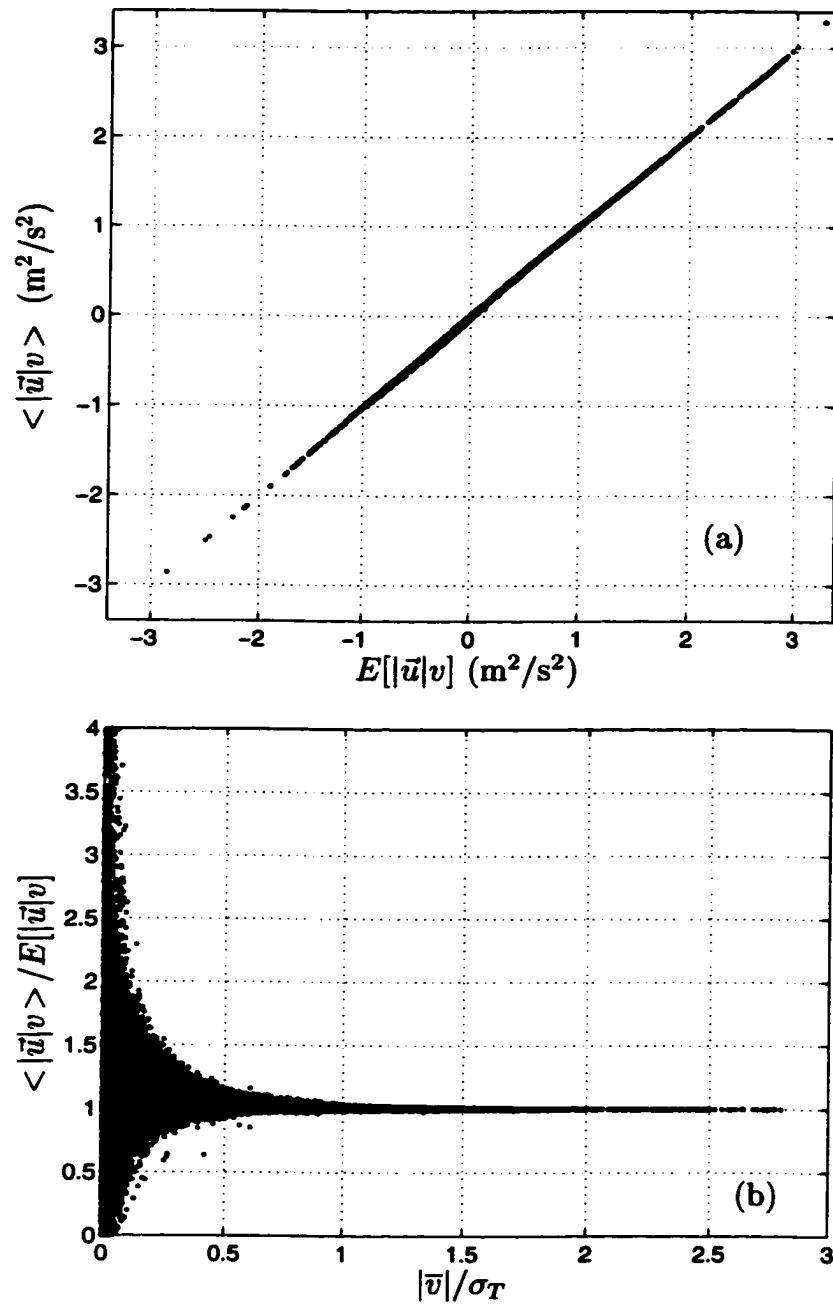


Figure III.4: (a) Observed $\langle |\bar{u}|v \rangle$ versus the expected value $E[|\bar{u}|v]$ assuming a joint-Gaussian velocity field with observed means, variances, and ρ_{uv} . The slope is 1.00, and the skill is $r^2 = 1.00$. (b) The ratio $\langle |\bar{u}|v \rangle / E[|\bar{u}|v]$ versus $|\bar{v}|/\sigma_T$.

used to guide the parameter space considered, and likely are representative of other nearshore environments as well.

The dependence of $E[|\bar{u}|v]/\sigma_T\bar{v}$ on σ_v/σ_u , with $\bar{u} = 0$ and $\rho_{uv} = 0$, is shown in Figure III.5a. For $|\bar{v}|/\sigma_T > 0.5$ no data points in Figure III.3a lie below the $\sigma_v/\sigma_u = 0$ curve. The range of $\langle |\bar{u}|v \rangle / \sigma_T\bar{v}$ with varying σ_v/σ_u decreases with larger $|\bar{v}|/\sigma_T$. The values of $E[|\bar{u}|v]/\sigma_T\bar{v}$ are relatively insensitive to variations of $|\rho_{uv}|$ when $\bar{u}/\sigma_T = 0$ (Figure III.5b), and slightly more sensitive to variations of \bar{u}/σ_T when $\rho_{uv} = 0$ (Figure III.5c). In contrast, when $\bar{u}/\sigma_T \neq 0$ and $\rho_{uv} \neq 0$, $E[|\bar{u}|v]/\sigma_T\bar{v}$ is spread over a wide range of values for small $|\bar{v}|/\sigma_T$ (Figure III.5d), and the envelope of these curves bracket the observed distribution of $\langle |\bar{u}|v \rangle / \sigma_T\bar{v}$ in Figure III.3a. As $|\bar{v}|/\sigma_T \rightarrow 0$, $E[|\bar{u}|v]/\sigma_T\bar{v} \rightarrow \pm\infty$ because $\langle |\bar{u}|v \rangle$ does not necessarily vanish when $\bar{v} = 0$, but $\bar{u} \neq 0$ and $\rho_{uv} \neq 0$ (III.6). As the magnitude of \bar{u}/σ_T increases, the spreading of $E[|\bar{u}|v]/\sigma_T\bar{v}$ in Figure III.5d persists for larger $|\bar{v}|/\sigma_T$. However, even for the extreme observed value (Table III.1) $\bar{u}/\sigma_T = 1$, this effect becomes important only for $|\bar{v}|/\sigma_T < 0.75$ (not shown). From Figure III.3a, the observed spreading occurs largely for $|\bar{v}|/\sigma_T \leq 0.5$.

III.E.3 Nonlinear Parameterizations

The ED80, TG86, and $|\rho_{uv}| = 1$ $E[|\bar{u}|v]$ parameterizations all with $\bar{u} = 0$ (as commonly is assumed in 1-D alongshore current modeling) have high skills ($r^2 \geq 0.98$) and best-fit slopes close to unity (Table III.2 and Figure III.6) regardless of wave angle definition. With $\bar{u} = 0$, all three parameterizations are functions of three parameters (\bar{v} , σ_T , and θ). In ED80 and TG86, $u_0 = \sqrt{2}\sigma_T$ is used. The wave angle θ is set to either (a) the zero spread (i.e. $\rho_{uv} = \pm 1$) wave angle $\tan|\theta| = \sigma_v/\sigma_u$, (b) the *Kuik et al.* [1988] mean wave angle (always closer to normal incidence than (a)), or (c) $\theta = 0$. Examining the effect of different wave angles is equivalent to varying σ_v/σ_u . These parameterizations do differ from the full joint-Gaussian $E[|\bar{u}|v]$ as $|\bar{v}|/\sigma_T \rightarrow 0$ (compare Figure III.7a with Figure III.7b-d) where the bias and standard deviations in the ratio of the observed to parameter-

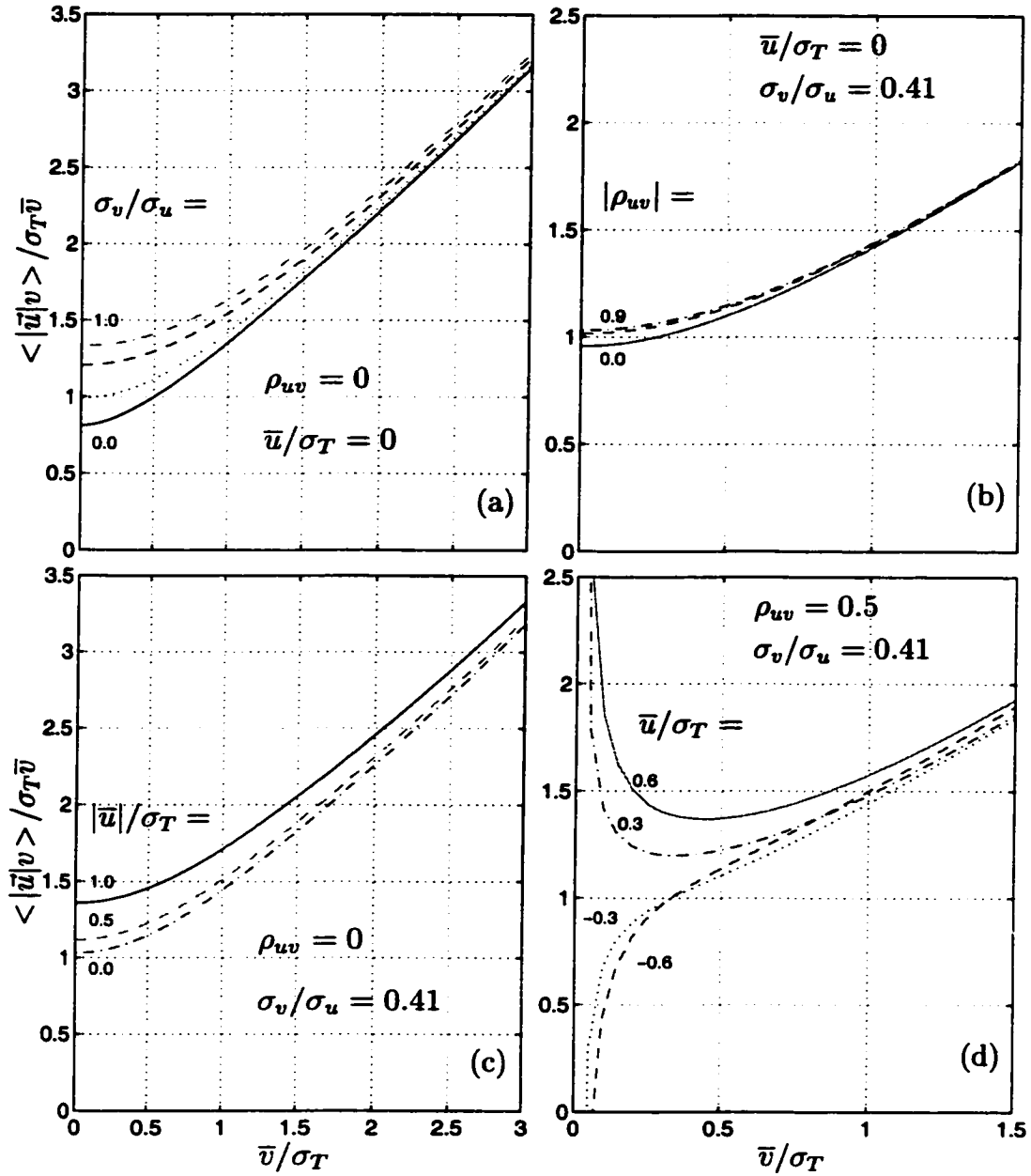


Figure III.5: The joint-Gaussian based $E[|\bar{u}|v]/\sigma_T \bar{v}$ versus $|\bar{v}|/\sigma_T$. (a) $\bar{u}/\sigma_u = 0$, $\rho_{uv} = 0$, and $\sigma_v/\sigma_u = 0.0$ (solid), 0.35 (dotted), 0.7 (dashed), and 1.0 (dash-dot). (b) $\bar{u} = 0$, $\sigma_v/\sigma_u = 0.41$ (the observed mean value), and $|\rho_{uv}| = 0.9$ (dash-dot), 0.45 (dashed), and 0 (solid). (c) $\sigma_v/\sigma_u = 0.41$, $\rho_{uv} = 0$, and $|\bar{u}|/\sigma_T = 1.0$ (solid), 0.5 (dashed), and 0 (dash-dot). (d) $\sigma_v/\sigma_u = 0.41$, $\rho_{uv} = 0.5$, and $\bar{u}/\sigma_T = -0.6$ (dashed), -0.3 (dotted), 0.3 (dash-dot), and 0.6 (solid). Note the axes scales of (a) and (c) are different than (b) and (d).

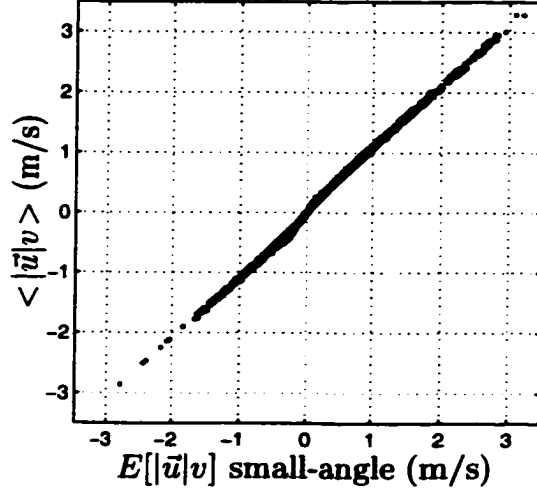


Figure III.6: Observed $\langle |\vec{u}|v \rangle$ versus the closed form small-angle parameterization (III.2) with the observed \bar{v} and σ_T . The best-fit slope is 1.06 and the skill $r^2 = 0.98$. Plots for all the nonlinear parameterizations (sections 4.3 and 4.4) are similar.

ized $\langle |\vec{u}|v \rangle$ increase. The bias is greater with $\theta = 0$ than with $\tan |\theta| = \sigma_v/\sigma_u$ (compare Figure III.7c with Figure III.7b), which reflects the importance of σ_v/σ_u for small $|\bar{v}|/\sigma_T$. Including \bar{u} (not shown) only marginally improves the parameterizations for small $|\bar{v}|/\sigma_T$ and the best-fit slopes are only slightly closer to unity than with $\bar{u} = 0$ (Table III.2).

	TG86	ED80	$ \rho_{uv} = 1 E[\vec{u} v]$
(a) $\tan \theta = \sigma_v/\sigma_u$	1.008	1.013	0.979
(b) $\theta = \text{Kuik}$	1.037	1.044	0.983
(c) $\theta = 0$	1.042	1.050	1.059 (SA)

Table III.2: Best-fit slopes between the observed $\langle |\vec{u}|v \rangle$ and the TG86, ED80, and the $E[|\vec{u}|v]$ with $|\rho_{uv}| = 1$ (III.21) parameterizations (all with $\bar{u} = 0$) using three different wave angles. The *Kuik et al.* [1988] angle is a principal axes angle calculated from the velocity covariance matrix. The $\theta = 0$ entry for the $|\rho_{uv}| = 1 E[|\vec{u}|v]$ is the SA (III.2) parameterization (Figure III.6). For all parameterizations the skill $r^2 \geq 0.98$.

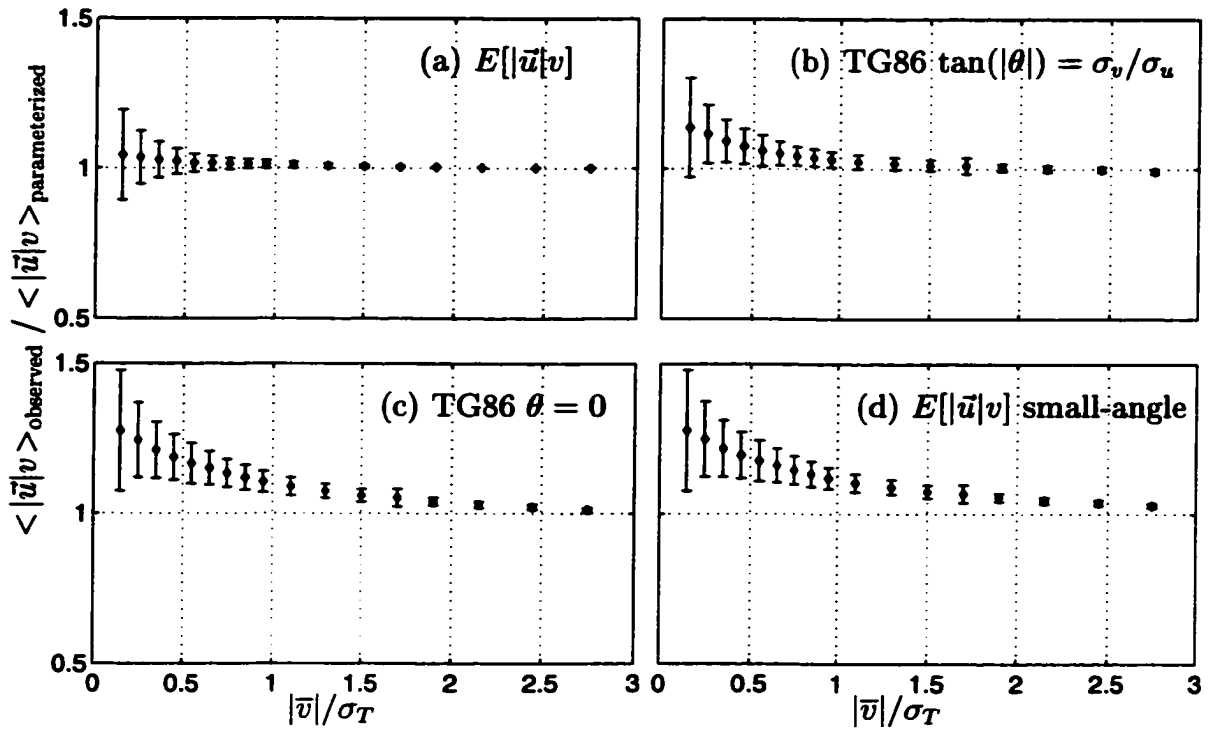


Figure III.7: Means (\diamond) and standard deviations (vertical bars) of the ratio of the observed to the parameterized $\langle |\vec{u}|v \rangle$. (a) The joint-Gaussian $E[|\vec{u}|v]$, (b) TG86 with $\tan(|\theta|) = \sigma_v/\sigma_u$, (c) TG86 with $\theta = 0$, and (d) closed form small-angle (III.2).

	mean	standard deviation	maximum	minimum
$\alpha(\sigma_v/\sigma_u, \rho_{uv})$	1.02	0.05	1.38	0.88
$\alpha(\sigma_v/\sigma_u)$	0.92	0.04	1.27	0.83

Table III.3: Statistics of $\alpha(\sigma_v/\sigma_u, \rho_{uv})$ (III.4) and $\alpha(\sigma_v/\sigma_u)$ (III.5) based on the observed σ_v/σ_u and ρ_{uv} .

III.E.4 Empirical Nonlinear Parameterizations

Empirical parameterizations, hybrids of the weak-current and strong-current forms are suggested by the distribution of $\langle |\vec{u}|v \rangle / \sigma_T \bar{v}$ in Figures III.3 and III.5. The formulations have algebraic forms, convenient for theoretical and numerical analysis. The *Wright and Thompson* [1983] empirical form (III.12)

$$\langle |\vec{u}|v \rangle = \sigma_T \bar{v} [\alpha^2 + (|\bar{v}|/\sigma_T)^2]^{1/2},$$

is examined with three weak-current limits for α . The first $\alpha(\sigma_v/\sigma_u, \rho_{uv})$ is based on a joint-Gaussian wave field and $\bar{u} = 0$ (III.4), and is evaluated numerically using the observed σ_v/σ_u and ρ_{uv} . The $\alpha(\sigma_v/\sigma_u, \rho_{uv})$ values typically lie (Table III.3) between the small-angle 0.798 and isotropic 1.33 limits. The WT83 parameterization with $\alpha(\sigma_v/\sigma_u, \rho_{uv})$ has best-fit slope 1.02, high skill ($r^2 = 0.99$), and low bias for small values of $|\bar{v}|/\sigma_T$ (Figure III.8a). This parameterization performs almost as well as the joint-Gaussian based $E[|\vec{u}|v]$ for all values of $|\bar{v}|/\sigma_T$ (compare Figure III.8a with Figure III.7a).

An $\alpha(\sigma_v/\sigma_u)$ based on a unidirectional random wave field has a closed form expression (III.5) that typically has smaller values than the more general $\alpha(\sigma_v/\sigma_u, \rho_{uv})$ (Table III.3). This is reflected in the increased bias in the ratio of the observed to parameterized $\langle |\vec{u}|v \rangle$ for small $|\bar{v}|/\sigma_T$ (compare Figure III.8b with Figure III.8a). However, the best-fit slope is 1.05, the skill is high ($r^2 = 0.99$), and the bias and scatter are no larger than the more complicated parameterizations in Figure III.7b-d. Owing to the limited range of both α (Table III.3), a best-fit constant $\alpha = 1.16$ (which is within the range of weak-current derived α in Table III.3) can be used in WT83 (III.12), with high skill ($r^2 = 0.99$), and only

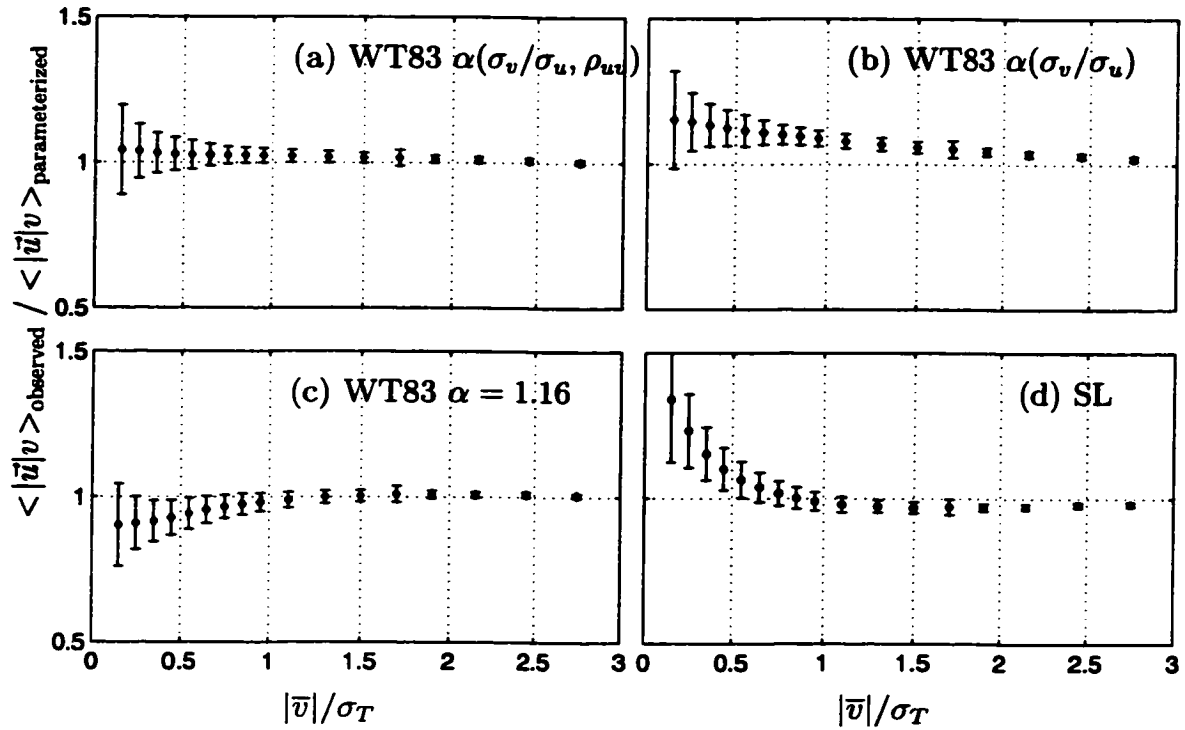


Figure III.8: Means (\diamond) and standard deviations (vertical bars) of the ratio of the observed to the parameterized $\langle |\vec{u}|v \rangle$. (a) WT83 with the weak-current $\alpha(\sigma_v/\sigma_u, \rho_{uv})$, (b) WT83 with the weak-current unidirectional wave $\alpha(\sigma_v/\sigma_u)$, (c) WT83 with the best-fit constant $\alpha = 1.16$, and (d) SL with best-fit constants $a_1 = 0.66$ and $a_2 = 0.87$.

slightly increased bias for small values of $|\bar{v}|/\sigma_T$ (Figure III.8c).

A second empirical form, the straight-line parameterization (known hereinafter as SL)

$$\langle |\bar{u}|v \rangle = a_1 \sigma_T \bar{v} + a_2 |\bar{v}| \bar{v}. \quad (\text{III.16})$$

is suggested by the linear relationship between $\langle |\bar{u}|v \rangle / \sigma_T \bar{v}$ and $|\bar{v}|/\sigma_T$ in Figure III.3b. The best-fit coefficients ($a_1 = 0.66$ and $a_2 = 0.87$) are found by fitting (III.16) to the observed $\langle |\bar{u}|v \rangle$. The straight-line parameterization reproduces $\langle |\bar{u}|v \rangle$ with high skill ($r^2 = 0.98$). Although the best-fit SL parameterization has the largest bias and standard deviations for small $|\bar{v}|/\sigma_T$ (Figure III.8d), the errors for $|\bar{v}|/\sigma_T > 0.5$ are similar to the other nonlinear parameterizations considered, and (III.16) allows for direct solution in 1-D alongshore current models that balance wave (and wind) forcing against bottom stress.

These nonlinear $\langle |\bar{u}|v \rangle$ parameterizations, based on different assumptions of the flow field have larger errors (Figure III.7b-e and Figure III.8) than the joint-Gaussian based $E[|\bar{u}|v]$ (Figure III.7a), but may reproduce $\langle |\bar{u}|v \rangle$ adequately (Figure III.6) for many modeling applications. The critical elements in parameterizing $\langle |\bar{u}|v \rangle$ accurately are \bar{v} and σ_T . For small $|\bar{v}|/\sigma_T$ other factors (e.g. σ_v/σ_u , \bar{u}/σ_T , ρ_{uv} , velocity skewness) are also important. The choice of parameterization for a particular application depends on the desired tradeoff between complexity and accuracy.

III.F Discussion

The $\langle |\bar{u}|v \rangle$ parameterizations examined above use the observed total velocity variance σ_T^2 that includes variability on time scales of sea-swell (0.05-0.3 Hz) and infragravity and shear waves (< 0.05 Hz). In alongshore current models, σ_T often is inferred from a wave-transformation model [e.g. *Thornton and Guza*, 1983; *Church and Thornton*, 1993; *Lippmann et al.*, 1996; and many others] that only includes sea and swell, and excludes lower frequency motions. The

relationship between σ_{Tbp} (the sea-swell bandpassed σ_T) and σ_T is investigated here to determine the effect of neglecting infragravity and shear waves in the $\langle |\bar{u}|v \rangle$ parameterizations.

During SandyDuck, multiple sensors were deployed at different cross-shore locations (Figure III.1). At each of these cross-shore locations, bandpassed σ_u^2 and σ_v^2 were calculated over the sea-swell frequency band and summed to give σ_{Tbp}^2 . The infragravity contribution to σ_T is largest near the shoreline, where the relationship between σ_T and σ_{Tbp} has a best-fit slope of 0.83 and $r^2 = 0.94$ (e.g. on average infragravity and shear waves contribute 17% to σ_T near the shoreline). Farther offshore, the infragravity contribution decreases, and the best-fit slopes between σ_T and σ_{Tbp} are closer to unity (0.93-0.96) and there is less scatter ($r^2 = 0.98$).

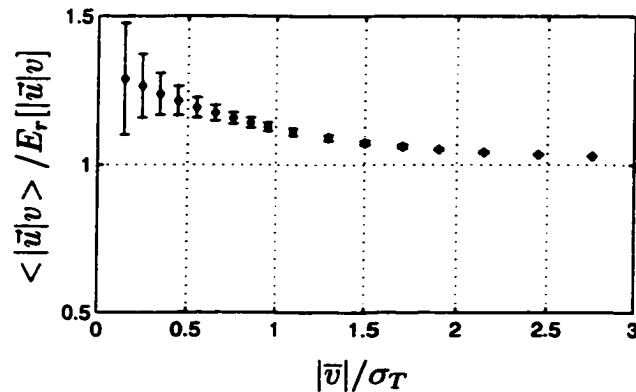


Figure III.9: The means and standard deviations of the ratio $\langle |\bar{u}|v \rangle / E_r[|\bar{u}|v]$ versus $|\bar{v}|/\sigma_T$. The observed $\langle |\bar{u}|v \rangle$ is used, and $E_r[|\bar{u}|v]$ is based on the observed \bar{u} , \bar{v} , and ρ_{uv} , but with 80% of the observed σ_u and σ_v . The corresponding result using the observed σ_u and σ_v is shown in Figure III.7a.

The effect of using a reduced σ_T (σ_{Tr}) in the joint-Gaussian parameterization ($E_r[|\bar{u}|v]$) is examined in Figure III.9 by reducing σ_u and σ_v (and therefore σ_T) to 80% of their original values (a typical near-shoreline reduction). For small $|\bar{v}|/\sigma_T$, the $\langle |\bar{u}|v \rangle / E_r[|\bar{u}|v]$ binned means are about $1/0.8 = 1.25$ (e.g. σ_T/σ_{Tr}), as expected from a weak-current linearization proportional to $\sigma_T\bar{v}$. For larger $|\bar{v}|/\sigma_T$, the $\langle |\bar{u}|v \rangle / E_r[|\bar{u}|v]$ ratio approaches unity, as expected because both

$\langle |\vec{u}|v \rangle$ and $E_r[|\vec{u}|v] \sim |\bar{v}|\bar{v}$ for large $|\bar{v}|/\sigma_T$. Thus, the maximum average under-prediction of $\langle |\vec{u}|v \rangle$, by the factor σ_{T_r}/σ_T , occurs for small $|\bar{v}|/\sigma_T$. Based on the best-fit slopes between σ_T and $\sigma_{T_{bp}}$, using $\sigma_{T_{bp}}$ results in an average stress error of less than 10% seaward of the shallowest sensor location, and average errors as large as 20% at the shallowest locations, comparable with the mean errors introduced with the nonlinear parameterizations discussed in section 4.3 (compare Figure III.7b-d with Figure III.9).

Simple alongshore current models balance the alongshore wave forcing (e.g. gradients in the wave radiation stress) with the alongshore bottom stress τ_y^b . Alongshore current solutions on a barred bathymetry are shown in Figure III.10 for four (best-fit) $\langle |\vec{u}|v \rangle$ parameterizations given by

$$\frac{\tau_y^b}{\rho c_f} = \begin{cases} 1.62 \sigma_T \bar{v} & \text{weak - current linearized (III.15)} \\ 0.99 \bar{v} & \text{Rayleigh (III.7)} \\ \sigma_T \bar{v} [1.16^2 + (\bar{v}/\sigma_T)^2]^{1/2} & \text{WT83 (III.12)} \\ 0.66 \sigma_T \bar{v} + 0.87 |\bar{v}|\bar{v} & \text{SL (III.16),} \end{cases}$$

with c_f constant in the cross-shore. Alongshore current solutions for the first two (linear) models are proportional to c_f^{-1} , whereas the WT83 and SL parameterization have a single solution that scales between $\bar{v} \sim c_f^{-1/2}$ (for stronger forcing) and $\bar{v} \sim c_f^{-1}$ (for weaker forcing). Therefore \bar{v} solutions with the SL and WT83 are less sensitive to c_f changes than are solutions with the linear parameterizations.

Garcez-Faria et al. [1998] report a range of drag coefficients $c_f = 0.001$ to $c_f = 0.01$ based on calculating τ_y^b using observed vertical profiles of \bar{v} and bottom boundary layer theory [*Grant and Madsen*, 1979]. For $c_f = 0.01$ (Figure III.10a), the maximum $|\bar{v}|/\sigma_T \approx 0.6$, and the magnitude and structure of the four \bar{v} solutions are similar. The small difference between WT83 and SL is consistent with the $|\bar{v}|/\sigma_T \sim 0.5$ trends in Figure III.8c-d. For $c_f = 0.001$ (Figure III.10b), the current is strong (the WT83 and SL maximum $|\bar{v}|/\sigma_T = 2.3$), and the weak-current (III.15) and Rayleigh (III.7) parameterization give $\bar{v}_{\max} = 2.9$ m/s and $\bar{v}_{\max} = 3.6$ m/s respectively, much larger than the $\bar{v}_{\max} = 1.8$ m/s predicted using

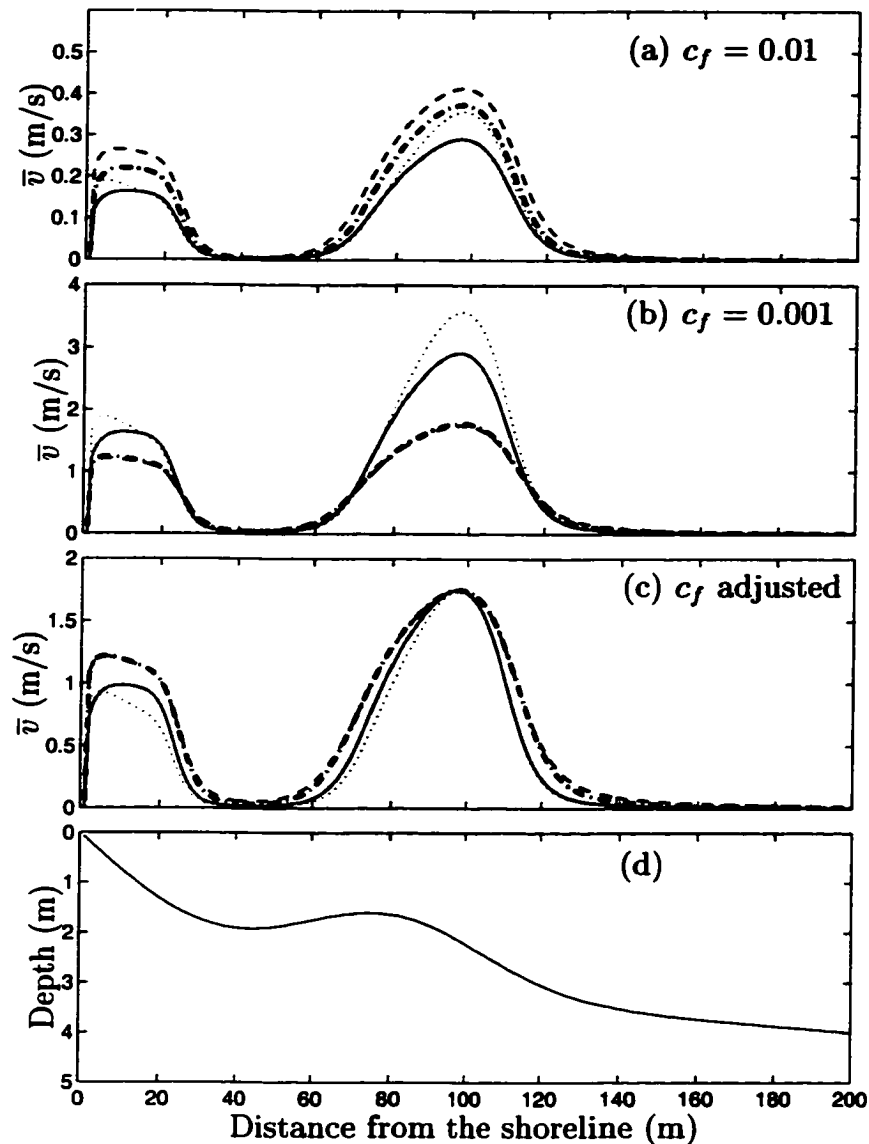


Figure III.10: Alongshore current solutions versus distance from the shoreline with four parameterizations for the bottom stress: weak-current (III.15) (solid), Rayleigh (dotted), WT83 (dash-dot), and SL (dashed). Solutions are shown for different values of the drag coefficient c_f . (a) $c_f = 0.01$, (b) $c_f = 0.001$, and (c) with c_f adjusted to yield the same \bar{v}_{\max} as SL with $c_f = 0.001$. The c_f values for the weak-current, Rayleigh, WT83, and SL parameterizations are 1.66, 2.04, 1.03, and 1.00 (all $\times 10^{-3}$) respectively. The flow is forced by waves (offshore $H_{\text{rms}} = 1$ m, $\theta = 10^\circ$, and peak period $T = 10$ s) that are transformed using Church and Thornton [1993] over the barred bathymetry shown in (d).

WT83 or SL. Similar differences between linear and nonlinear parameterizations are apparent in *Church and Thornton* [1993, Figures 8, 10, and 11], although different c_f values are used for each parameterization. To avoid the unrealistically large velocities predicted with linearized $\langle |\vec{u}|v \rangle$ parameterizations, c_f typically is adjusted to match the magnitude of the observed flow. A factor of two adjustment of c_f in the linear parameterizations is needed to match the \bar{v}_{\max} predicted by SL with $c_f = 0.001$, whereas the c_f adjustment is only 3% for WT83 (Figure III.10c). Inferring c_f values by fitting models using linearized bottom stresses to data can be misleading.

III.G Conclusions

The weak-current (III.15) and the Rayleigh (III.7) parameterizations of the alongshore bottom stress are inaccurate for the wide range of conditions observed between the shoreline and 8-m water depth (Figure III.2). The weak-current parameterization has significant bias and scatter at larger $\langle |\vec{u}|v \rangle$ (Figure III.2a). The observed distribution of $\langle |\vec{u}|v \rangle / \sigma_T \bar{v}$ is highly scattered at small $|\bar{v}|/\sigma_T$, and depends linearly on $|\bar{v}|/\sigma_T$ at larger values of $|\bar{v}|/\sigma_T$ (Figure III.3) consistent with $\langle |\vec{u}|v \rangle \sim |\bar{v}| \bar{v}$.

An expected-value $E[|\vec{u}|v]$ based on a joint-Gaussian distributed velocity field accurately parameterizes $\langle |\vec{u}|v \rangle$ (Figure III.4). The observed distribution of $\langle |\vec{u}|v \rangle / \sigma_T \bar{v}$ (Figure III.3a) is reproduced by varying the parameters (\bar{v}/σ_T , \bar{u}/σ_T , σ_v/σ_u , ρ_{uv} , Appendix B) that govern $E[|\vec{u}|v]/\sigma_T \bar{v}$ (Figure III.5).

The joint-Gaussian parameterization $E[|\vec{u}|v]$ requires a more detailed specification of the velocity field than usually is available. Other nonlinear parameterizations, *Ebersole and Dalrymple* [1980], *Thornton and Guza* [1986], and special cases of $E[|\vec{u}|v]$ (III.21 and III.2), approximately reproduce $\langle |\vec{u}|v \rangle$ (Table III.2 and Figure III.6) regardless of the wave angle definition and whether or not the observed \bar{u} is included. The empirical WT83 (III.12) and the straight-line pa-

parameterization (III.16) also reproduce $\langle |\vec{u}|v \rangle$. The most important factors in parameterizing $\langle |\vec{u}|v \rangle$ are \bar{v} and σ_T . At small $|\bar{v}|/\sigma_T$, other factors (e.g. σ_v/σ_u , \bar{u} , and ρ_{uv}) are important and the parameterizations differ (Figures III.7 and III.8).

Neglecting velocity fluctuations in the infragravity frequency band (< 0.05 Hz) on average reduces σ_T by about 20% close to the shoreline, resulting in average errors in the joint-Gaussian values of $E[|\vec{u}|v]$ (Figure III.9) comparable with the average errors of the nonlinear parameterizations of section 4.3 (Figure III.7c-d). Errors from neglecting infragravity velocity fluctuations decrease farther offshore. Alongshore current solutions with linear parameterizations of the bottom stress are more sensitive to variations in c_f than are solutions using nonlinear parameterizations. Inferring c_f by fitting model solutions using the linear parameterizations to observations can be misleading.

III.H Appendix A. Evaluation of $E[|\vec{u}|v]$

Assuming a joint-Gaussian probability density function for u and v , the expected value of $E[|\vec{u}|v]$ is

$$E[|\vec{u}|v] = \frac{1}{2\pi\sigma_u\sigma_v(1-\rho_{uv}^2)} \int_{-\infty}^{\infty} \int_{-\infty}^{\infty} \sqrt{u^2 + v^2} v \times \exp\left[-\frac{\sigma_v^2(u-\bar{u})^2 - 2\rho_{uv}\sigma_u\sigma_v(u-\bar{u})(v-\bar{v}) + \sigma_u^2(v-\bar{v})^2}{2\sigma_u^2\sigma_v^2(1-\rho_{uv}^2)}\right] dudv. \quad (\text{III.17})$$

Writing the velocities in terms of mean and fluctuating components (i.e. $u = \bar{u} + u'$) gives

$$E[|\vec{u}|v] = \frac{1}{2\pi \det(\mathbf{C}_{uv})} \int_{-\infty}^{\infty} \int_{-\infty}^{\infty} \sqrt{(u' + \bar{u})^2 + (v' + \bar{v})^2} (v' + \bar{v}) \exp\left(-\frac{1}{2}\mathbf{u}'^T \mathbf{C}_{uv}^{-1} \mathbf{u}'\right) du' dv' \quad (\text{III.18})$$

where $\mathbf{u} = [u' \ v']^T$, and the velocity covariance matrix \mathbf{C}_{uv} is

$$\mathbf{C}_{uv} = \begin{bmatrix} \sigma_u^2 & \rho_{uv}\sigma_u\sigma_v \\ \rho_{uv}\sigma_u\sigma_v & \sigma_v^2 \end{bmatrix}. \quad (\text{III.19})$$

The symmetric, positive semi-definite matrix \mathbf{C}_{uv}^{-1} exists (because the observed $|\rho_{uv}| \neq 1$ and $\sigma_v \neq 0$) and has an eigenvalue decomposition

$$\mathbf{C}_{uv}^{-1} = \mathbf{L}\Lambda^{-1}\mathbf{L}^T$$

where \mathbf{L} is the orthonormal eigenvector matrix, and $\Lambda = \text{diag}(\lambda_i)$ is the eigenvalue matrix. Transforming into stretched principal axes such that $\mathbf{x} = \Lambda^{-1/2}\mathbf{L}^T\mathbf{u}/\sqrt{2}$, where $\mathbf{x} = [x \ y]^T$, so that

$$\mathbf{x}^T\mathbf{x} = \frac{1}{2}\mathbf{u}^T\mathbf{C}_{uv}^{-1}\mathbf{u}$$

and defining $\mathbf{K} = \sqrt{2}\mathbf{L}\Lambda^{1/2}$, it follows that $\mathbf{u} = \mathbf{K}\mathbf{x}$, and $dudv = \det(\mathbf{K})dxdy$, where $\det(\mathbf{K}) = 2\sqrt{\lambda_1\lambda_2}$.

The term $\sqrt{u^2 + v^2}v$ in (III.17) is written with the change of variable as ($\mathbf{K} = k_{ij}$)

$$g(x, y) = [(k_{11}^2 + k_{21}^2)x^2 + 2(k_{11}k_{12} + k_{21}k_{22})xy + (k_{12}^2 + k_{22}^2)y^2 + 2(k_{11}x + k_{12}y)\bar{u} + 2(k_{21}x + k_{22}y)\bar{v} + \bar{u}^2 + \bar{v}^2]^{1/2} (k_{21}x + k_{22}y + \bar{v}).$$

Defining $\gamma = \pi\sigma_u\sigma_v\sqrt{(1 - \rho^2)/(\lambda_1\lambda_2)}$, the integral (III.17) becomes

$$E[|\bar{u}|v] = \frac{1}{\gamma} \int_{-\infty}^{\infty} \int_{-\infty}^{\infty} g(x, y) \exp[-(x^2 + y^2)]dxdy. \quad (\text{III.20})$$

Equation (III.20) was integrated numerically using a $n = 24$ point quadrature scheme for both x and y appropriate for integrals of the form (III.20) [Abramowitz and Stegun, 1968],

$$E[|\bar{u}|v] \approx \frac{1}{\gamma} \sum_{i=1}^n \sum_{j=1}^n w_{ij}g(x_i, y_j)$$

where x_i and y_j are the zeros of the Hermite polynomials $H_n(x)$ and $H_n(y)$, and w_{ij} are the weights

$$w_{ij} = \frac{2^{2n-2}n!n!\pi}{n^4 H_{n-1}^2(x_i)H_{n-1}^2(y_j)}$$

This scheme is both accurate and efficient. A $n = 12$ point quadrature scheme also could be used in a circulation model. For the case where $\bar{u} = 0$ and $\sigma_v = 0$ the numerical integration agrees well with the closed form solution (Appendix C) for the small-angle parameterization. Small errors in the numerical integration as $\bar{v}/\sigma_u \rightarrow 0$ with $\bar{u} = 0$ are expected because the function $\sqrt{u^2}$ has a discontinuous derivative at $u = 0$. The quadrature scheme is most accurate with functions that are continuous and have continuous derivatives.

If the wave spread σ_θ is assumed zero (i.e. $\rho_{uv} = \pm 1$) as in TG86 and ED80, then the double integral in (III.17) is transformed into a single integral

$$E[|\bar{u}|v] = \frac{1}{\sqrt{2\pi}\sigma_T} \int_{-\infty}^{\infty} [(u'_T \cos(\theta) + \bar{u})^2 + (u'_T \sin(\theta) + \bar{v})^2]^{1/2} (u'_T \sin(\theta) + \bar{v}) \exp\left[-\frac{u'^2_T}{2\sigma_T^2}\right] du'_T \quad (\text{III.21})$$

that is readily calculated with an analogous quadrature scheme.

Although $\langle |\bar{u}|u \rangle$ is not related obviously to the time-averaged cross-shore bottom stress because of the strong depth variation in \bar{u} , it is interesting to examine whether the relationship between $\langle |\bar{u}|u \rangle$ and $E[|\bar{u}|u]$ is as robust as that between $\langle |\bar{u}|v \rangle$ and $E[|\bar{u}|v]$ (Figure III.4). The joint-Gaussian $E[|\bar{u}|u]$, integrated numerically with the scheme described above, is compared with $\langle |\bar{u}|u \rangle$ in Figure III.11. The skill between $\langle |\bar{u}|u \rangle$ and $E[|\bar{u}|u]$ is high ($r^2 = 0.95$), but is lower than that between $\langle |\bar{u}|v \rangle$ and $E[|\bar{u}|v]$. The reduced range of observed $\langle |\bar{u}|u \rangle$ and increased scatter at small values of $\langle |\bar{u}|u \rangle$ relative to $\langle |\bar{u}|v \rangle$ both contribute to the lower skill.

III.I Appendix B. Weak-current Approximations

For a joint-Gaussian velocity field, the ratio $\langle |\bar{u}|v \rangle / \sigma_T \bar{v}$ is

$$\frac{E[|\bar{u}|v]}{\sigma_T \bar{v}} = \frac{1}{2\pi(1 - \rho_{uv}^2)} \int_{-\infty}^{\infty} \int_{-\infty}^{\infty} \sqrt{\left(\frac{u'}{\sigma_T} + \frac{\bar{u}}{\sigma_T}\right)^2 + \left(\frac{v'}{\sigma_T} + \frac{\bar{v}}{\sigma_T}\right)^2} \left(\frac{v'}{\bar{v}} + 1\right) \exp\left[-\frac{1}{2(1 - \rho_{uv}^2)} \left(\frac{u'^2}{\sigma_u^2} - \frac{2\rho_{uv}u'v'}{\sigma_u\sigma_v} + \frac{v'^2}{\sigma_v^2}\right)\right] \frac{du'}{\sigma_u} \frac{dv'}{\sigma_v}.$$

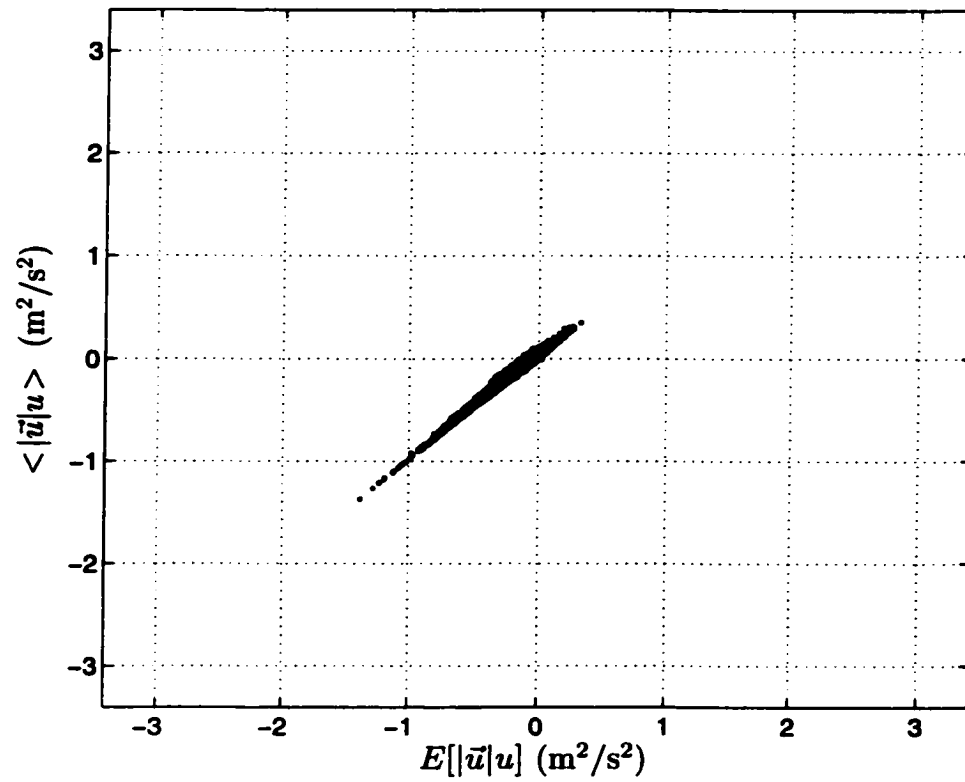


Figure III.11: Observed $\langle |\vec{u}|u \rangle$ versus $E[|\vec{u}|u]$. The skill $r^2 = 0.95$ and $N = 70,099$. The scale is the same as in Figure III.4.

With $x = u'/\sigma_T$ and $y = v'/\sigma_T$, and using $\sigma_T^2 = \sigma_u^2 + \sigma_v^2$, it follows that

$$\frac{E[|\vec{u}|v]}{\sigma_T \bar{v}} = \frac{\left(\frac{\sigma_u}{\sigma_v} + \frac{\sigma_v}{\sigma_u}\right)}{2\pi(1 - \rho_{uv}^2)} \iint_{-\infty}^{\infty} \sqrt{\left(x + \frac{\bar{u}}{\sigma_T}\right)^2 + \left(y + \frac{\bar{v}}{\sigma_T}\right)^2} \left(y \frac{\sigma_T}{\bar{v}} + 1\right) \exp\left[-\frac{x^2 \left(1 + \frac{\sigma_u^2}{\sigma_v^2}\right) + 2\rho_{uv}xy \left(\frac{\sigma_u}{\sigma_u} + \frac{\sigma_u}{\sigma_v}\right) + y^2 \left(1 + \frac{\sigma_u^2}{\sigma_v^2}\right)}{2(1 - \rho_{uv}^2)}\right] dx dy \quad (\text{III.1})$$

which is a function of four nondimensional quantities, \bar{v}/σ_T , \bar{u}/σ_T , σ_v/σ_u , and ρ_{uv} .

Denoting the expected value with the brackets operator, (III.1) is

$$\frac{E[|\vec{u}|v]}{\sigma_T \bar{v}} = \left\langle \sqrt{\left(x + \frac{\bar{u}}{\sigma_T}\right)^2 + \left(y + \frac{\bar{v}}{\sigma_T}\right)^2} \left(y \frac{\sigma_T}{\bar{v}} + 1\right) \right\rangle. \quad (\text{III.2})$$

For weak-currents (i.e. small \bar{v}/σ_T and \bar{u}/σ_T), Taylor expanding the square-root in (III.2), and keeping up to linear terms in the mean current gives

$$\frac{E[|\vec{u}|v]}{\sigma_T \bar{v}} = \left\langle (x^2 + y^2)^{1/2} \left[1 + \frac{x}{(x^2 + y^2)} \frac{\bar{u}}{\sigma_T} + \frac{y}{(x^2 + y^2)} \frac{\bar{v}}{\sigma_T}\right] \left(y \frac{\sigma_T}{\bar{v}} + 1\right) \right\rangle.$$

The joint-Gaussian expected value of odd functions is zero so

$$\left\langle \frac{x}{(x^2 + y^2)^{1/2}} \right\rangle \frac{\bar{u}}{\sigma_T} = \left\langle \frac{y}{(x^2 + y^2)^{1/2}} \right\rangle \frac{\bar{v}}{\sigma_T} = \langle y(x^2 + y^2)^{1/2} \rangle \frac{\sigma_T}{\bar{v}} = 0.$$

Note that if the underlying probability density function has a non-zero skewness, then $\langle y(x^2 + y^2)^{1/2} \rangle \neq 0$, and as $|\bar{v}|/\sigma_T \rightarrow 0$, $E[|\vec{u}|v]/\sigma_T \bar{v} \rightarrow \pm\infty$.

For weak-currents and a joint-Gaussian velocity field,

$$\frac{E[|\vec{u}|v]}{\sigma_T \bar{v}} = \left\langle (x^2 + y^2)^{1/2} + \frac{y^2}{(x^2 + y^2)^{1/2}} + \frac{xy}{(x^2 + y^2)^{1/2}} \frac{\bar{u}/\sigma_T}{\bar{v}/\sigma_T} \right\rangle. \quad (\text{III.3})$$

With the common alongshore current modeling assumption $\bar{u} = 0$, (III.3) reduces to a function of σ_v/σ_u and ρ_{uv} ,

$$\frac{E[|\vec{u}|v]}{\sigma_T \bar{v}} = \left\langle \frac{x^2 + 2y^2}{(x^2 + y^2)^{1/2}} \right\rangle, \quad (\text{III.4})$$

which can be integrated using techniques described in Appendix A. The value of the isotropic case ($\sigma_v/\sigma_u = 1$ and $\rho_{uv} = 0$) considered by *Wright and Thompson* [1983], is recovered from (III.4)

$$\frac{E[|\vec{u}|v]}{\sigma_T \bar{v}} = \frac{3}{4} \Gamma(1/2) = \frac{3\sqrt{\pi}}{4}.$$

where Γ is the gamma function. When $|\rho_{uv}| = 1$, (III.4) yields a closed form solution,

$$\frac{E[|\bar{u}|v]}{\sigma_T \bar{v}} = \sqrt{\frac{2}{\pi}} \left[1 + \frac{\sigma_v^2/\sigma_u^2}{1 + \sigma_v^2/\sigma_u^2} \right] = \sqrt{\frac{2}{\pi}} [1 + \sin^2 \theta]. \quad (\text{III.5})$$

The correction for wave obliquity is the same as for unidirectional monochromatic waves (III.6) [*Liu and Dalrymple, 1978*].

Allowing $\bar{u}/\sigma_T \neq 0$ with $|\rho_{uv}| = 1$ gives a closed form expression for the third term in (III.3)

$$\left\langle \frac{xy}{(x^2 + y^2)^{1/2}} \right\rangle \frac{\bar{u}/\sigma_T}{\bar{v}/\sigma_T} = \sqrt{\frac{2}{\pi}} \text{sgn}(\rho_{uv}) \left(\frac{\sigma_u}{\sigma_v} + \frac{\sigma_v}{\sigma_u} \right)^{-1} \frac{\bar{u}/\sigma_T}{\bar{v}/\sigma_T} = \sqrt{\frac{2}{\pi}} \text{sgn}(\rho_{uv}) \frac{\sigma_u \sigma_v}{\sigma_T^2} \frac{\bar{u}}{\bar{v}}. \quad (\text{III.6})$$

For $\bar{u} \neq 0$, as $\bar{v} \rightarrow 0$ the ratio $E[|\bar{u}|v]/\sigma_T \bar{v} \rightarrow \pm\infty$ depending on the signs of ρ_{uv} , \bar{u} , and \bar{v} . When $\rho_{uv} = 0$,

$$\left\langle \frac{xy}{(x^2 + y^2)^{1/2}} \right\rangle = 0,$$

and \bar{u} does not enter into the weak-current forms.

III.J Appendix C. Small-Angle Parameterization

The small-angle (SA) parameterization follows from (III.17) with the assumption that alongshore velocities are negligible ($\sigma_v = 0$) and $\bar{u} = 0$,

$$E[|\bar{u}|v] = \frac{\bar{v}}{\sqrt{2\pi}\sigma_T} \int_{-\infty}^{\infty} \sqrt{u'^2 + \bar{v}^2} \cdot \exp\left(-\frac{u'^2}{2\sigma_T^2}\right) du'. \quad (\text{III.1})$$

Changing variables so that $r^2 = u'^2/(2\sigma_T^2)$ and $b = \bar{v}^2/(4\sigma_T^2)$ yields

$$E[|\bar{u}|v] = \sqrt{\frac{2}{\pi}} \sigma_T \bar{v} \times \int_{-\infty}^{\infty} \sqrt{r^2 + 2b} \cdot \exp(-r^2) dr = \sqrt{\frac{2}{\pi}} \sigma_T \bar{v} \cdot b \exp(b) [K_0(b) + K_1(b)] \quad (\text{III.2})$$

where K_0 and K_1 are the modified Bessel functions of the second kind. As $|\bar{v}|/\sigma_T \rightarrow 0$, $b \rightarrow 0$, $\exp(b) \sim 1 + b$, $K_0(b) \sim -\ln b$, and $K_1(b) \sim b^{-1}$, so to leading order

$$E[|\bar{u}|v] \sim \sqrt{\frac{2}{\pi}} \sigma_T \bar{v} \cdot b(1+b)(b^{-1} - \ln b) \sim \sqrt{\frac{2}{\pi}} \sigma_T \bar{v},$$

recovering the weak-current limit. As $|\bar{v}|/\sigma_T \rightarrow \infty$, $b \rightarrow \infty$,

$$K_0(b), K_1(b) \sim \sqrt{\pi/2} b^{-1/2} \exp(-b)$$

so to leading order

$$E[|\bar{u}|v] \sim \sqrt{\frac{2}{\pi}} \sigma_T \bar{v} \cdot 2\sqrt{\frac{\pi}{2}} \frac{\bar{v}}{2\sigma_T} = |\bar{v}| \bar{v}$$

recovering the strong-current limit.

Acknowledgements

This research was supported by the ONR Coastal Dynamics and AASERT programs and the NSF CooP program. Steve Lentz and Glenn Ierley provided useful suggestions. Staff from the Center for Coastal Studies acquired the field data. Britt Raubenheimer and Edie Gallagher helped collect the data. The Field Research Facility, Coastal Engineering Research Center, Duck, North Carolina, provided excellent logistical support. Thank you.

This chapter, in full, is a reprint of Feddersen, F., R. T. Guza, S. Elgar, T. H. C. Herbers, Alongshore bottom stress parameterizations, in preparation. I was the primary researcher and author, and the co-authors listed in this publication directed and supervised the research which forms the basis of this chapter.

III.K References

- Abramowitz, M., and Stegun, I., *Handbook of Mathematical Functions*, Dover, New York, 1968.
- Allen, J. S., P. A. Newberger, and R. A. Holman Nonlinear shear instabilities of alongshore currents on plane beaches, *J. Fluid Mech.* **310**, 181–213, 1996.
- Battjes, J. A., Surf-zone dynamics, *Ann. Rev. Fluid Mech.*, **20**, 257–293, 1988.
- Bowden, K. F., Note on wind drift in a channel in the presence of tidal currents, *Proc. Royal Soc. A*, **219**, 426–446, 1953.
- Bowen, A.J., The generation of longshore currents on a plane beach, *J. Mar. Res.*, **27**, 206–215, 1969.
- Church, J. C., and E. B. Thornton, Effects of breaking wave induced turbulence within a longshore current model, *Coastal Eng.*, **20**, 1–28, 1993.
- Ebersole, B. A. and Dalrymple, R. A. Numerical modeling of nearshore circulation, *Proc 17th Int. Coastal Engineering Conf.*, New York, ASCE, pp. 2710–2725, 1980.
- Elgar, S., R. T. Guza, B. Raubenheimer, T. H. C. Herbers, E. Gallagher, Spectral evolution of shoaling and breaking waves on a barred beach, *J. Geophys. Res.*, **102**, 15,797–15,805, 1997.
- Elgar, S., W. C. O'Reilly, B. Raubenheimer, R. T. Guza, T. H. C. Herbers, Pier effects on waves, *J. Waterways, Port, Coastal, Ocean Eng.*, ASCE (in review), 1999.
- Feddersen, F., R. T. Guza, S. Elgar, and T. H. C. Herbers, Alongshore momentum balances in the nearshore, *J. Geophys. Res.*, **103**, 15,667–15,676, 1998.
- Feddersen, F. Finite amplitude shear waves, *J. Fluid Mech.*, **372**, 71–91, 1998.
- Gallagher, E. L., S. Elgar and R. T. Guza. Observations of sand bar evolution on a natural beach, *J. Geophys. Res.*, **103**, 3203–3215, 1998.
- Garcez-Faria, A. F., E. B. Thornton, T. P. Stanton, C. V. Soares, and T. C. Lippmann, Vertical profiles of longshore currents and related bed shear stress and bottom roughness, *J. Geophys. Res.*, **103**, 3217–3232, 1998.
- Grant, W. D., and O. S. Madsen, Combined wave and current interaction with a rough bottom, *J. Geophys. Res.*, **84**, 1797–1808, 1979.

- Guza, R. T., and E. B. Thornton, Velocity moments in the nearshore, *J. Waterways, Port, Coastal, Ocean Eng.*, ASCE, **111**, 235–256 1985.
- Herbers, T. H. C, S. Elgar, and R. T. Guza, Directional spreading of waves in the nearshore, *J. Geophys. Res.*, (in press), 1999.
- Kuik, A. J., G. P. van Vledder, and L. H. Holthuijsen, A method for the routine analysis of pitch-and-roll buoy wave data, *J. Phys. Oceanogr.*, **18**, 1020–1034, 1988.
- Lentz, S. J., and C. D. Winant, Subinertial currents on the southern California shelf, *J. Phys. Oceanogr.*, **16**, 1737–1750, 1986.
- Lippmann T. C., A. H. Brookins, and E. B. Thornton, Wave energy transformation on natural profiles, *Coastal. Eng.*, **27**, 1–20, 1996.
- Liu, P. L., and R. A. Dalrymple, Bottom frictional stresses and longshore currents due to waves with large angles of incidence, *J. Mar. Res.*, **36**, 357–373, 1978.
- Longuet-Higgins, M. S., On the statistical distribution of the heights of sea waves, *J. Mar. Res.*, **11**, 245–266, 1952.
- Longuet-Higgins, M. S., Longshore currents generated by obliquely incident sea waves 1, *J. Geophys. Res.*, **75**, 6790–6801, 1970.
- Özkan, H. T., and J. T. Kirby, Finite amplitude shear wave instabilities, *Proc. Coastal Dynamics 95*, ASCE, 465–476, 1995.
- Özkan-Haller, H. T., and J. T. Kirby, Nonlinear evolution of shear instabilities of the longshore current: A comparison of observations and computations, *J. Geophys. Res.*, (in press), 1999.
- Rooth, C., A linearized bottom friction law for large-scale oceanic motions, *J. Phys. Oceanogr.*, **2**, 509–510, 1972.
- Slinn, D. N., J. S. Allen, P. A. Newberger, and R. A. Holman, Nonlinear shear instabilities of alongshore currents over barred beaches, *J. Geophys. Res.*, **103**, 18357–18,379, 1998.
- Thornton, E.B., Variation of longshore current across the surf zone, in *Proc. 12th Int. Coastal Engineering Conf.*, pp. 291-308, Am. Soc. of Civ. Eng., New York, 1970.
- Thornton, E. B., J. L. Swayne, J. R. Dingler, Small-scale morphology across the surf zone, *Mar. Geol.*, **145**, 173–196, 1998.

- Thornton, E. B. and R. T. Guza, Transformations of wave height distribution, *J. Geophys. Res.*, **88**, 5925–5938, 1983.
- Thornton, E. B. and R. T. Guza, Surf zone longshore currents and random waves: field data and models, *J. Phys. Oceanogr.*, **16**, 1165–1178, 1986.
- Wright, D. G and K. R. Thompson, Time-averaged forms of the nonlinear stress law, *J. Phys. Oceanogr.*, **13**, 341–346, 1983.
- Wu, C. S, E. B Thornton, and R. T. Guza, Waves and longshore currents: comparison of a numerical model with field data, *J. Geophys. Res.*, **90**, 4951–4958, 1985.

Chapter IV

Weakly Nonlinear Shear Waves

IV.A Abstract

Alongshore propagating low frequency $O(0.01 \text{ Hz})$ waves related to the direction and intensity of the alongshore current were first observed in the surf zone by *Oltman-Shay et al.* [1989]. Based on a linear stability analysis, *Bowen and Holman* [1989] demonstrated that a shear instability of the alongshore current gives rise to alongshore propagating shear (vorticity) waves. The fully nonlinear dynamics of finite amplitude shear waves, investigated numerically by *Allen et al.* [1996], depend on α , the nondimensional ratio of frictional to nonlinear terms, essentially an inverse Reynolds number. A wide range of shear wave environments are reported as a function of α , from equilibrated waves at larger α to fully turbulent flow at smaller α . When α is above the critical level α_c , the system is stable. In this paper, a weakly nonlinear theory, applicable to α just below α_c , is developed. The amplitude of the instability is governed by a complex Ginzburg-Landau equation. For the same beach slope and base-state alongshore current used in *Allen et al.* [1996], a equilibrated shear wave is found analytically. The finite amplitude behavior of the analytic shear wave, including a forced second harmonic, correction to the mean alongshore current, and amplitude dispersion, agree well with the numerical results of *Allen et al.* [1996]. Limitations in their

numerical model prevent the development of a side-band instability. The stability of the equilibrated shear wave is demonstrated analytically. The analytical results confirm that the *Allen et al.* [1996] model correctly reproduces many important features of weakly nonlinear shear waves.

IV.B Introduction

Low frequency approximately nondispersive alongshore propagating waves with periods of $O(100\text{ s})$ and wavelengths of $O(100\text{ m})$ were first observed on a barred beach by *Oltman-Shay et al.* [1989]. The wavelengths of these motions are much shorter than the wavelengths of edge waves of the same frequency, and are related to the intensity and direction of the mean alongshore current. In a companion paper, *Bowen and Holman* [1989] used linear stability theory, an idealized topography, and an idealized alongshore current to demonstrate that a shear instability of the alongshore current leads to growing, nearly nondispersive shear waves propagating in the direction of the alongshore current. *Dodd et al.*, [1992] included a linearized bottom stress, realistic barred-beach profile, and alongshore currents, found good agreement between wavelengths and frequencies of the most unstable linear mode and the energetic regions of the observed frequency-wavenumber spectra of velocity. However, neither linear stability analyses nor frequency-wavenumber spectra address the finite amplitude behavior of shear waves.

The finite amplitude behavior of shear waves was investigated numerically by *Allen et al.* [1996, hereafter ANH96)]. Using the rigid-lid shallow-water equations on a planar beach with an idealized alongshore forcing and a linearized bottom stress, ANH96 found that the nonlinearity of the flow can be characterized by a nondimensional parameter α (Q in ANH96), the ratio of frictional to nonlinear terms, essentially an inverse Reynolds number. For values of α below the critical value for an instability α_c , a wide range of behaviors is reported, rang-

ing from steady equilibrated waves at larger values of α to irregular eddies and transient rips at smaller values of α . In ANH96, shear wave energy propagates nondispersively for all values of α . It is not known whether natural shear wave environments are similar to those at larger or smaller α reported by ANH96.

ANH96 did not study the near critical (i.e. at α just below α_c) behavior of shear waves. An issue complicating such study is that numerical effects can alter the near critical behavior. For example, *Hyman et al.* [1986] found that inadequate numerical accuracy could induce a false stability in simulations of the Kuramoto-Sivashinsky equation. In the ANH96 model, finite numerical resolution and biharmonic friction (added for numerical stability) might significantly distort the solutions near α_c . Note also that finite alongshore domain lengths prevent potential side-band instabilities and motions on scales longer than the domain length from developing.

In this paper analytic shear wave solutions are found for near critical conditions when the departure from stability, given by ϵ

$$\epsilon^2 = \frac{\alpha_c - \alpha}{\alpha_c}, \quad (\text{IV.1})$$

is small that largely confirm the results of ANH96. Preliminary work on the finite amplitude weakly nonlinear theory has been reported by *Dodd and Thornton* [1992]. Recently *Shrira et al.* [1997] demonstrated that, for weak bottom friction ($\alpha \ll 1$), resonant triads composed of growing waves experience an explosive instability. Here we follow the approach of *Stewartson and Stuart*, [1971], who solved for the finite amplitude behavior of instabilities of plane Poiseuille flow. An equation for the perturbation potential vorticity is derived in terms of the perturbation streamfunction ψ , and expanded in powers of ϵ . At $O(\epsilon)$ [e.g. *Bowen & Holman*, 1989; *Dodd et al.*, 1992; and others], the eigenvalue problem for ψ at a particular α and alongshore wavenumber k yields growing or decaying alongshore propagating wave solutions for the streamfunction. There is a critical pair (α_c, k_c) such that one eigenvalue has zero imaginary component whose eigenfunction is a neutrally stable

wave, and the rest have negative imaginary components whose eigenfunctions are decaying solutions. The frequency of the neutrally stable mode is by definition the primary frequency. At $O(\epsilon^2)$ phenomena typical of weakly nonlinear waves are found: a correction to the mean flow and a forced wave (second harmonic) at twice the primary frequency and wavenumber. At $O(\epsilon^3)$ the complex Ginzburg-Landau equation for the amplitude of the disturbance is derived. This equation has solutions that can exhibit a wide variety of behaviors ranging from a simple steady wave to chaotic solutions [Manneville, 1990]. For the same choice of beach slope and alongshore forcing as ANH96, the real part of the Landau coefficient is negative, indicating that the instability is supercritical and that equilibrated finite amplitude solutions are possible at $O(\epsilon^3)$. Time-periodic solutions for the amplitude of the disturbance are side-band stable, and amplitude dispersion, a frequency shift of the equilibrated wave related to ϵ , is found.

Analytic solutions are compared to numerical solutions using the model of ANH96 at α near α_c . Equilibrated finite amplitude waves are found in the ANH96 solutions, and exhibit characteristic features of weakly nonlinear systems, such as spectral peaks at integer frequencies of the primary frequency and amplitude dispersion. Numerical effects that affect the near critical behavior of the shear instability also complicate comparison with the analytic model, particularly since α_c for the ANH96 model is different from the analytic model. Nevertheless, the cross-shore structures of the ANH96 model primary wave, the second harmonic, and the mean flow correction are in excellent agreement with theory. Although differences in the α_c and therefore the ϵ of the two models prevent quantitative comparison of shear wave amplitudes, the ANH96 model shear wave amplitudes and amplitude dispersion are in reasonable agreement with the analytic model. The overall level of agreement between the analytic and ANH96 model verifies that the ANH96 model correctly reproduces the qualitative behavior of weakly nonlinear shear waves.

The remainder of this paper is organized as follows: The weakly nonlinear

theory for a planar beach and arbitrary background alongshore current is developed in section 2. The numerical method and solutions for the finite amplitude shear waves are described in section 3. Comparisons to ANH96 are given in section 4. Section 5 contains a discussion and conclusion.

IV.C Theory

Including forcing and linear bottom friction, the rigid-lid shallow water equations (continuity, cross-, and alongshore momentum) representing the depth- and time-averaged flow in the nearshore are

$$(hu)_x + (hv)_y = 0 \quad (\text{IV.2a})$$

$$u_t + uu_x + vv_y = -g\eta_x - \nu u/h \quad (\text{IV.2b})$$

$$v_t + uv_x + vv_y = -g\eta_y + F - \nu v/h \quad (\text{IV.2c})$$

where x and y are the cross- and alongshore coordinates respectively (Figure IV.1), u and v are the cross- and alongshore velocities, η is the sea surface elevation, ν is a constant friction coefficient, and g represents gravity. This system of equations (IV.2) is the same as in ANH96 except that biharmonic friction terms included in ANH96 to dampen numerical instabilities are not required here. The bathymetry contours are planar ($h(x) = \beta x$) and the shoreline is at $x = 0$. Following ANH96, the forcing $F(x)$ from breaking, obliquely-incident, surface-gravity waves is for simplicity alongshore directed and does not vary in the alongshore direction. The bottom stress terms (e.g. $\nu v/h$) are an idealized representation of the bulk effects of bottom stress in the surf zone. This representation has the advantage that it is simple analytically, and has been used in the linear stability problem [*Dodd et al.*, 1992; *Falques and Iranzo*, 1994] and by ANH96. Although other bottom stress representations which take orbital wave velocities into account are probably more realistic in the surf zone [e.g. *Thornton and Guza*, 1986], the simple bottom stress

representation is appropriate for both numerical model based [e.g. ANH96] and theory-based process studies of shear waves, and allows comparison of the present results to ANH96.

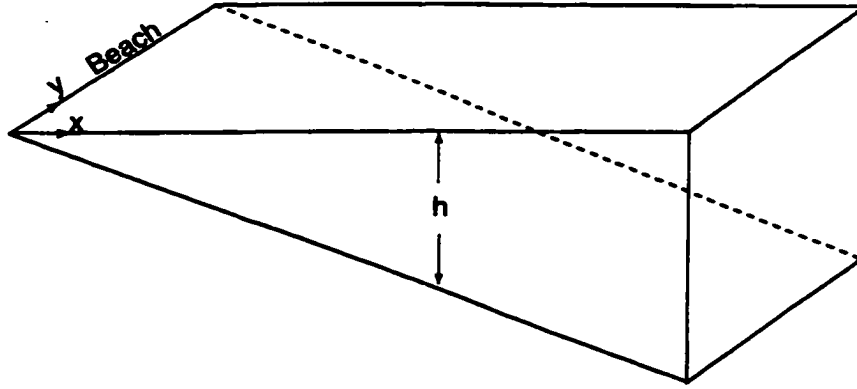


Figure IV.1: The coordinate system used. x is the cross-shore coordinate and y is the alongshore coordinate.

If the alongshore current is steady and independent of y (i.e. $v = V(x)$), it then follows from the continuity equation and the boundary condition of no mass flux into the shoreline ($hu = 0$ at $x = 0$) that u vanishes everywhere. The base-state alongshore current whose stability will be investigated is then given by a balance between forcing and bottom friction,

$$V(x) = \frac{Fh}{\nu} = \frac{F\beta x}{\nu}.$$

The shallow water equations are nondimensionalized with the following scalings (ANH96):

$$u = Uu' \quad v = Uv'$$

$$x = Lx' \quad y = Ly'$$

$$t = Tt' = \frac{L}{U}t'$$

$$g\eta = N\eta'$$

$$h = h_0 h' = \beta L x'$$

$$F = \frac{U\nu}{h_0} F' = \frac{U\nu}{\beta L} F'$$

where the primed quantities are nondimensional. The choice for the length scale L is typically the distance from the shoreline to the maximum in the alongshore current. Previous linear stability analyses [e.g. *Putrevu and Svendsen, 1992*] have found that the ratio of L to the wavelength of the fastest growing wave is $O(1)$. The velocity scale U chosen is the maximum of the base-state alongshore current $V(x)$. The choice for the time scale $T = L/U$ is based on the observation [*Oltman-Shay et al., 1989; Dodd et al., 1992*] and linear stability result [e.g. *Bowen and Holman, 1989; Putrevu and Svendsen, 1992*] that the shear wave phase speed is 0.5-0.7 of the maximum alongshore current. *Falques and Iranzo (1994)* have found that the rigid-lid approximation used here is excellent for the linear stability problem when the maximum of the Froude number $\text{Fr} = V(x)/\sqrt{gh(x)}$, is 0.14, and still quite reasonable for values as large as $\text{Fr}_{\max} = 0.63$. The affect of the rigid-lid approximation on finite amplitude shear waves was investigated numerically by *Özkan and Kirby (1995)* whose results were quantitatively consistent with those of ANH96 with a $\text{Fr}_{\max} = 0.154$.

Dropping the primes, the resulting nondimensional equations are

$$(ux)_x + (vx)_y = 0 \tag{IV.3a}$$

$$u_t + uu_x + vv_y = -\gamma\eta_x - \alpha u/x \tag{IV.3b}$$

$$v_t + uv_x + vv_y = -\gamma\eta_y + \alpha(F - v/x) \tag{IV.3c}$$

where $\gamma = N/U^2$ is the ratio of pressure forces to nonlinearity, and $\alpha = \nu/\beta U$ is the ratio of frictional and nonlinear terms, an inverse Reynolds number, analogous to the parameter Q of ANH96. The nondimensional base-state alongshore current is $V(x) = xF(x)$.

Consider a perturbation of u and v about the base-state alongshore current $V(x)$. The nondimensional perturbation equations become

$$(ux)_x + (vx)_y = 0$$

$$u_t + uu_x + (v + V)u_y = -\gamma\eta_x - \alpha u/x$$

$$v_t + u(v_x + V_x) + (v + V)v_y = -\gamma\eta_y - \alpha v/x.$$

Taking the curl of the perturbation momentum equations, dividing by the water depth and substituting the continuity equation yields a perturbation potential vorticity equation

$$\frac{Dq}{Dt} + uQ_x = \frac{\alpha}{x} \left[-\left(\frac{v}{x}\right)_x + \left(\frac{u}{x}\right)_y \right]$$

where

$$\frac{D}{Dt} = \frac{\partial}{\partial t} + u\frac{\partial}{\partial x} + (V + v)\frac{\partial}{\partial y}.$$

The perturbation potential vorticity is $q = \zeta/x$, the perturbation vorticity is $\zeta = v_x - u_y$, and the background potential vorticity is $Q = V_x/x$. In terms of the perturbation transport streamfunction ψ , where $\psi_x = xv$ and $\psi_y = -xu$, the potential vorticity becomes

$$q = \frac{1}{x^2} (\nabla^2\psi - \psi_x/x),$$

and the potential vorticity equation is

$$\frac{D}{Dt} \left[\frac{1}{x^2} (\nabla^2\psi - \psi_x/x) \right] - \frac{\psi_y}{x} Q_x = -\frac{\alpha}{x^3} (\nabla^2\psi - 2\psi_x/x). \quad (\text{IV.4})$$

The boundary conditions of no cross-shore mass flux at both the shoreline and far offshore make ψ constant at $x = 0$ and ∞ . The perturbation is assumed not to induce any net alongshore transport so ψ is the same constant (set for convenience to $\psi = 0$) at $x = 0$ and ∞ . Fully expanded in terms of ψ and multiplied by x^2 ,

(IV.4) becomes

$$\begin{aligned} (\nabla^2\psi - \psi_x/x)_t - \frac{\psi_y}{x} (\nabla^2\psi_x - 2\nabla^2\psi/x - \psi_{xx}/x + 3\psi_x/x^2) - xQ_x\psi_y \\ + \left(V + \frac{\psi_x}{x}\right) (\nabla^2\psi_y - \psi_{xy}/x) = -\frac{\alpha}{x} (\nabla^2\psi - 2\psi_x/x). \end{aligned} \quad (\text{IV.5})$$

This equation and the boundary conditions on ψ govern the evolution of shear instabilities on a planar sloping bottom with a given base-state alongshore current. Substituting a perturbation expansion of ψ ,

$$\psi = \epsilon\psi_1 + \epsilon^2\psi_2 + \epsilon^3\psi_3 + \dots, \quad (\text{IV.6})$$

into (IV.5) and collecting terms of $O(\epsilon)$ yields

$$\begin{aligned} L[\psi_1] &= (\nabla^2\psi_1 - \psi_{1x}/x)_t - xQ_x\psi_{1y} + V(\nabla^2\psi_{1y} - \psi_{1xy}/x) \\ &+ \frac{\alpha}{x} (\nabla^2\psi_1 - 2\psi_{1x}/x) = 0. \end{aligned} \quad (\text{IV.7})$$

This equation determines the linear stability of the flow. A alongshore propagating wave solution for ψ_1 ,

$$\psi_1 = \phi_1(x) \exp[ik(y - ct)] + \text{c.c.},$$

is substituted into (IV.7) where k is a alongshore wavenumber and c.c. denotes the complex conjugate. In general, c is complex. The real part c_r is the phase speed and is related to the frequency of the wave by $\omega = kc_r$. The imaginary part c_i is related to the linear growth rate of the wave as $\sigma = kc_i$. Collecting terms proportional to $\exp[ik(y - ct)]$ yields [Dodd *et al.*, 1992; ANH96]

$$\left(V - \frac{i\alpha}{kx} - c\right) (\phi_{1xx} - \phi_{1x}/x - k^2\phi_1) = xQ_x\phi_1 - \frac{i\alpha}{kx^2}\phi_{1x} \quad (\text{IV.8})$$

with boundary conditions $\phi_1(0) = \phi_1(\infty) = 0$. For a particular paired value of k and α , an infinite set of paired eigenvalues c and eigenfunctions $\phi_1(x)$ are solutions of (IV.8). To proceed with the weakly nonlinear analysis, the critical $\alpha = \alpha_c$ is sought such that there is only one wavenumber, $k = k_c$ for which a single

eigenvalue is purely real, while all others have negative imaginary parts. At all other wavenumbers the solutions decay ($c_i < 0$). At (α_c, k_c) , $\phi_1(x)$ represents the single neutral mode corresponding to the critical eigenvalue. A dispersion relation is defined at α_c

$$\omega_c(k) + i\sigma_c(k) = kc \quad (\text{IV.9})$$

where c is the critical eigenvalue. A few properties of this dispersion relation are

$$\sigma_c(k_c) = 0 \quad , \quad \frac{\partial \omega_c(k_c)}{\partial k} = c_g \quad , \quad \frac{\partial \sigma_c(k_c)}{\partial k} = 0 \quad (\text{IV.10})$$

where c_g is the group velocity. After finding α_c and k_c , the finite amplitude shear wave behavior for small values of ϵ is found by setting $\alpha = \alpha_c(1 - \epsilon^2)$ so that the perturbation grows slowly. The evolution of the instability is determined at $O(\epsilon^2)$ and $O(\epsilon^3)$.

At $O(\epsilon^2)$, the following scalings are introduced [*Stewartson and Stuart*, 1971; *Craik*, 1989]

$$\tau = \epsilon^2 t, \quad Y = \epsilon(y - c_g t) \quad (\text{IV.11})$$

where τ is a slow time, and Y is a stretched alongshore coordinate moving with the group velocity, c_g . The differential operators for time and the alongshore coordinate are replaced by

$$\partial_t \rightarrow \partial_t - \epsilon c_g \partial_Y + \epsilon^2 \partial_\tau, \quad \partial_y \rightarrow \partial_y + \epsilon \partial_Y. \quad (\text{IV.12})$$

Again the perturbation streamfunction ψ is expanded in powers of ϵ (IV.6), and ψ_1 , ψ_2 , and ψ_3 have the following forms

$$\psi_1 = A(\tau, Y) \phi_1(x) \exp[ik_c(y - ct)] + \text{c.c.} \quad (\text{IV.13})$$

$$\psi_2 = AA^*\phi_2^{(0)}(x) + A_Y\phi_2^{(1)}(x)\exp(ik_c(y-ct)) + A^2\phi_2^{(2)}(x)\exp[2ik_c(y-ct)] + \text{c.c.} \quad (\text{IV.14})$$

$$\psi_3 = |A|^2A\phi_3^{(1)}(x)\exp[ik_c(y-ct)] + \text{c.c.} + \dots \quad (\text{IV.15})$$

where k_c is the critical wavenumber, c is the phase speed of the neutral wave at (α_c, k_c) , and $A(\tau, Y)$ is the amplitude of the shear wave which may have slow variations in the alongshore and in time. The term proportional to $\phi_2^{(0)}(x)$ represents the correction to the mean transport, and that proportional to $\phi_2^{(2)}(x)$ the forced harmonic at twice the primary frequency (second harmonic).

Applying the scalings for time and alongshore coordinate (IV.12) to the full perturbation equation (IV.5) with $\alpha = \alpha_c(1 - \epsilon^2)$ and collecting terms of $O(\epsilon)$ and $O(\epsilon^2)$ gives

$$L_c[\psi_1] = 0,$$

and

$$\begin{aligned} L_c[\psi_2] &= \frac{\psi_{1y}}{x} (\nabla^2\psi_{1x} - 2\nabla^2\psi_1/x - \psi_{1xx}/x + 3\psi_{1x}/x^2) \\ &\quad - \frac{\psi_{1x}}{x} (\nabla^2\psi_{1y} - \psi_{1xy}/x) + c_g(\nabla^2\psi_1 - \psi_{1x}/x)_Y \\ &\quad - V(\psi_{1xx} + 3\psi_{1yy} - \psi_{1x}/x)_Y + xQ_x\psi_{1Y} \\ &\quad - 2\psi_{1yYt} - \frac{2\alpha_c}{x}\psi_{1yY} \end{aligned} \quad (\text{IV.16})$$

where the linear operator $L_c[\psi]$ is the operator $L[\psi]$ defined in (IV.7) with $\alpha = \alpha_c$. Substituting (IV.13) for ψ_1 and (IV.14) for ψ_2 into (IV.16) and collecting terms proportional to AA^* yields

$$\begin{aligned} L_0[\phi_2^{(0)}] &= \frac{\alpha_c}{x} \left(\phi_{2xx}^{(0)} - \frac{2\phi_{2x}^{(0)}}{x} \right) = \frac{ik_c}{x} (\phi_1\phi_{1xxx}^* - \phi_{1xxx}\phi_1^* + \phi_{1x}\phi_{1xx}^* - \phi_{1xx}\phi_{1x}^*) \\ &\quad + \frac{3ik_c}{x^2} (\phi_{1xx}\phi_1^* - \phi_1\phi_{1xx}^*) + \frac{3ik_c}{x^3} (\phi_1\phi_{1x}^* - \phi_{1x}\phi_1^*) \end{aligned} \quad (\text{IV.17})$$

with the boundary conditions $\phi_2^{(0)} = 0$ at $x = 0$ and $x = \infty$. The linear operator L_0 is L_n (with $n = 0$) where

$$L_n[\phi] = ink_c \left(V - \frac{i\alpha_c}{nk_c x} - c \right) (\phi_{xx} - \phi_x/x - (nk_c)^2 \phi) - ink_c x Q_x \phi - \frac{\alpha_c}{x^2} \phi_x \quad (\text{IV.18})$$

and n is an integer. The $O(\epsilon^2)$ terms proportional to $A_Y \exp[ik_c(y - ct)]$ give

$$L_1[\phi_2^{(1)}] = c_g(\phi_{1xx} - \phi_{1x}/x - k_c^2 \phi_1) - V(\phi_{1xx} - \phi_{1x}/x - 3k_c^2 \phi_1) + \left(xQ_x - 2k_c^2 c - \frac{2\alpha_c ik_c}{x} \right) \phi_1. \quad (\text{IV.19})$$

In general, $\phi_2^{(1)}$ is resonantly forced since the homogeneous problem, $L_1[\varphi] = 0$, is satisfied with the stated choice of α_c , k_c , and c . The solvability condition for $\phi_2^{(1)}$ requires that c_g satisfy

$$c_g = \frac{\int_0^\infty \phi_1^\dagger [V(\phi_{1xx} - \phi_{1x}/x - 3k_c^2 \phi_1) - (xQ_x - 2k_c^2 c - \frac{2\alpha_c ik_c}{x}) \phi_1] dx}{\int_0^\infty \phi_1^\dagger (\phi_{1xx} - \phi_{1x}/x - k_c^2 \phi_1) dx} \quad (\text{IV.20})$$

where $\phi_1^\dagger(x)$ is the adjoint function of $\phi_1(x)$ and is defined in Appendix A. The c_g found by (IV.20) should be equal to that found from the dispersion relationship (IV.10), providing a useful check of both the algebra and the numerical computations. With c_g (IV.19) can be solved for $\phi_2^{(1)}$ subject to boundary conditions $\phi_2^{(1)}(x) = 0$ at $x = 0$ and $x = \infty$. The $O(\epsilon^2)$ terms proportional to $A^2 \exp[2ik_c(y - ct)]$ are

$$L_2[\phi_2^{(2)}] = \frac{ik_c}{x} (\phi_1 \phi_{xxx} - \phi_{1x} \phi_{1xx}) + \frac{ik_c}{x^2} (-3\phi_1 \phi_{1xx} + 2k_c^2 \phi_1^2 + \phi_{1x}^2) + \frac{3ik_c}{x^3} (\phi_1 \phi_{1x}) \quad (\text{IV.21})$$

where L_2 is the operator L_n in (IV.18) with $n = 2$. With the boundary conditions, $\phi_2^{(2)} = 0$ at $x = 0$ and $x = \infty$, (IV.19) can be solved for $\phi_2^{(2)}(x)$.

The equation for the amplitude $A(\tau, Y)$ of the instability is determined from $O(\epsilon^3)$ terms in (IV.5) with $\alpha = \alpha_c(1 - \epsilon^2)$,

$$\begin{aligned}
L[\psi_3] = & -(\nabla^2\psi_1 - \frac{\psi_{1x}}{x})_\tau + \frac{\alpha_c}{x}(\nabla^2\psi_1 - \frac{2\psi_{1x}}{x}) - \frac{\alpha_c}{x}(\psi_{1YY} + 2\psi_{2yY}) \\
& - (\psi_{1YYt} + 2\psi_{2yYt}) + xQ_x\psi_{2Y} + c_g(2\psi_{1yYY} + \psi_{2xxY} + \psi_{2yyY} - \frac{\psi_{2xY}}{x}) \\
& - V(3\psi_{1yYY} + \psi_{2xxY} + 3\psi_{2yyY} - \frac{\psi_{2xY}}{x}) \\
& + \frac{\psi_{1y}}{x}(\nabla^2\psi_{2x} - \frac{3\psi_{2xx}}{x} - \frac{2\psi_{2yy}}{x} + \frac{3\psi_{2x}}{x^2}) \\
& + \frac{\psi_{2y}}{x}(\nabla^2\psi_{1x} - \frac{3\psi_{1xx}}{x} - \frac{2\psi_{1yy}}{x} + \frac{3\psi_{1x}}{x^2}) \\
& + \frac{\psi_{1Y}}{x}(\nabla^2\psi_{1x} - \frac{3\psi_{1xx}}{x} - \frac{2\psi_{1yy}}{x} + \frac{3\psi_{1x}}{x^2}) \\
& + \frac{\psi_{1y}}{x}(2\psi_{1xyY} - \frac{4\psi_{1yY}}{x}) - \frac{\psi_{2x}}{x}(\nabla^2\psi_{1y} - \frac{\psi_{1xy}}{x}) \\
& - \frac{\psi_{1x}}{x}(\nabla^2\psi_{2y} - \frac{\psi_{2xy}}{x}) - \frac{\psi_{1x}}{x}(\psi_{1xxY} + 3\psi_{1yyY} - \frac{\psi_{1xY}}{x}). \tag{IV.22}
\end{aligned}$$

The equation for $A(\tau, Y)$ is derived by substituting (IV.13) for ψ_1 and (IV.14) for ψ_2 , and invoking the solvability condition for ψ_3 . The terms in the right hand side of (IV.22) proportional to $\exp[ik_c(y - ct)]$ are multiplied by the adjoint function ϕ_1^\dagger and integrated in the cross-shore direction. The left hand side is identically zero (IV.38) and setting the right-hand side to zero yields a complex Ginzburg-Landau equation for the amplitude of the instability

$$A_\tau = \sigma A + \delta A_{YY} + \mu |A|^2 A \tag{IV.23}$$

where σ is the growth rate of the disturbance, δ is a dispersion term, and μ is the Landau coefficient which can limit the growth of the disturbance. These coefficients are all complex in general. First κ , which is given by the terms proportional to $A_\tau \exp[ik_c(y - ct)]$ on the right hand side of (IV.22), is defined

$$\kappa = \int_0^\infty \phi_1^\dagger (\phi_{1xx} - \phi_{1x}/x - \kappa_c^2 \phi_1) dx. \tag{IV.24}$$

The growth rate is given by the terms proportional to $A \exp[ik_c(y - ct)]$ on the right hand side of (IV.22),

$$\sigma \cdot \kappa = \int_0^\infty \phi_1^\dagger \frac{\alpha_c}{x} (\phi_{1xx} - 2\phi_{1x}/x - k_c^2 \phi_1) dx. \quad (\text{IV.25})$$

The terms proportional to $A_{YY} \exp[ik_c(y - ct)]$ on the right hand side of (IV.22) define δ ,

$$\delta \cdot \kappa = \int_0^\infty \phi_1^\dagger S dx. \quad (\text{IV.26})$$

where

$$\begin{aligned} S = & \left(-\frac{\alpha_c}{x} + ik_c(c + 2c_g - 3V) \right) \phi_1 + \left(xQ_x - 2ik_c \frac{\alpha_c}{x} - k_c^2(2c + c_g - 3V) \right) \phi_2^{(1)} \\ & + \frac{V - c_g}{x} \phi_{2x}^{(1)} + (c_g - V) \phi_{2xx}^{(1)}. \end{aligned}$$

The terms on the right hand side of (IV.22) proportional to $|A|^2 A \exp[ik_c(y - ct)]$ define the complex Landau constant μ ,

$$\mu \cdot \kappa = \int_0^\infty \phi_1^\dagger T dx, \quad (\text{IV.27})$$

where

$$\begin{aligned} T = & \frac{ik_c}{x} \left[2\phi_1 \phi_{2xxx}^{(0)} - \phi_1^* \phi_{2xxx}^{(2)} - 2\phi_{1x}^* \phi_{2xx}^{(2)} + 2\phi_{xxx}^* \phi_2^{(2)} - 2\phi_{1xx} \phi_{2x}^{(0)} + \phi_{1xx}^* \phi_{2x}^{(2)} \right. \\ & \left. + k_c^2 (3\phi_1^* \phi_{2x}^{(2)} + 6\phi_{1x}^* \phi_2^{(2)} + 2\phi_1 \phi_{2x}^{(0)}) \right] \\ & + \frac{ik_c}{x^2} \left(-6\phi_1 \phi_{2xx}^{(0)} + 3\phi_1^* \phi_{2xx}^{(2)} + \phi_{1x}^* \phi_{2x}^{(2)} - 6\phi_{1xx}^* \phi_2^{(2)} + 2\phi_{1x} \phi_{2x}^{(0)} - 4k_c^2 \phi_1^* \phi_2^{(2)} \right) \\ & + \frac{ik_c}{x^3} \left(6\phi_1 \phi_{2x}^{(0)} - 3\phi_1^* \phi_{2x}^{(2)} + 6\phi_{1x}^* \phi_2^{(2)} \right). \end{aligned}$$

The complex Ginzburg-Landau equation (IV.23) can exhibit a rich behavior of solutions depending on the values of its coefficients [Mannville, 1990]. When the real part of the Landau coefficient is negative, finite amplitude solutions can be found of the form

$$A(\tau, Y) = B \exp[i(\Lambda Y - \Omega \tau)] \quad (\text{IV.28})$$

where B is a complex constant. The simplest solution is when $\Lambda = 0$, and

$$|B|^2 = -\frac{\text{Re}(\sigma)}{\text{Re}(\mu)} \quad (\text{IV.29})$$

$$\Omega = -[\text{Im}(\sigma) + |B|^2 \text{Im}(\mu)]. \quad (\text{IV.30})$$

This solution is side-band stable [Benjamin and Feir, 1967; Stuart and DiPrima, 1978] if

$$\frac{\text{Im}(\mu)\text{Im}(\delta)}{\text{Re}(\mu)\text{Re}(\delta)} + 1 > 0. \quad (\text{IV.31})$$

IV.D Calculations for ANH96 base-state conditions

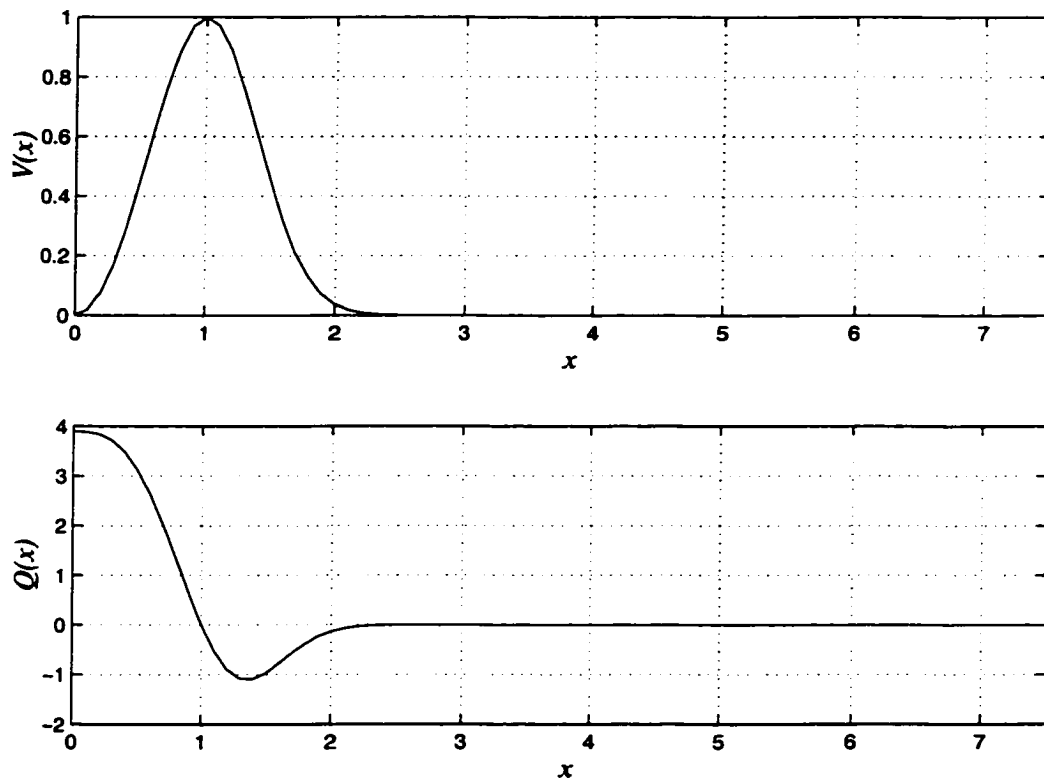


Figure IV.2: The base state nondimensional longshore current $V(x)$ (IV.33a) and potential vorticity $Q(x)$ (IV.33b).

The beach slope ($\beta = 0.05$) and forcing of ANH96 will be used for the weakly nonlinear calculations. The ANH96 base-state dimensional alongshore ve-

	a_2	a_1	a_0
$\omega(k)$	0.01286947973804	0.49060016442166	0.84216041525188
$\sigma(k)$	-0.08832279314348	0	1.89323×10^{-11}

Table IV.1: The quadratic coefficients for the growth rate and frequency, $\omega_c(k) + i\sigma_c(k) = a_2(k - k_c)^2 + a_1(k - k_c) + a_0$ where $k_c = 1.36326254916$

locity is

$$V(x) = C_o x^2 \exp\left(-\frac{x^3}{\delta^3}\right) \quad (\text{IV.32})$$

where

$$C_o = 2.4046099 \cdot 10^{-4} \frac{1}{\text{m} \cdot \text{s}}, \quad \delta = 103.02 \text{ m}$$

so that the maximum in V is 1 m/s and occurs at $x = 90$ m. Therefore the chosen velocity scale is $U = 1$ m/s. The length scale becomes $L = 90$ m. The ratio $L^3/\delta^3 = 2/3$, and the time scale is $T = 90$ s. The inverse Reynolds number for these scaling choices is $\alpha = 20\nu$. The maximum Froude number is $\text{Fr}_{\max} = 0.154$, close to the value of 0.14 found to satisfy the rigid-lid approximation for the linear stability problem [Falques and Iranzo, 1994]. The nondimensional base-state alongshore velocity $V(x)$ and potential vorticity $Q(x)$ become

$$V(x) = V_o x^2 \exp\left(-\frac{2x^3}{3}\right), \quad V_o = \frac{C_o L^2}{U} = \exp(2/3) \quad (\text{IV.33a})$$

$$Q(x) = 2V_o(1 - x^3) \exp\left(-\frac{2x^3}{3}\right), \quad (\text{IV.33b})$$

and are shown in Figure IV.2. The potential vorticity has a minimum, which satisfies the Rayleigh condition for inviscid instability.

ANH96 used a dimensional domain extending from $x = 0$ to $x = 1000$ m and from $y = 0$ to $y = 450$ m, corresponding to a nondimensional domain extending to $x = 11.1\bar{1}$ and $y = 5$. Because the solution is expected to decay exponentially offshore (Appendix B) a smaller nondimensional domain extending to $x = 7.5$ is

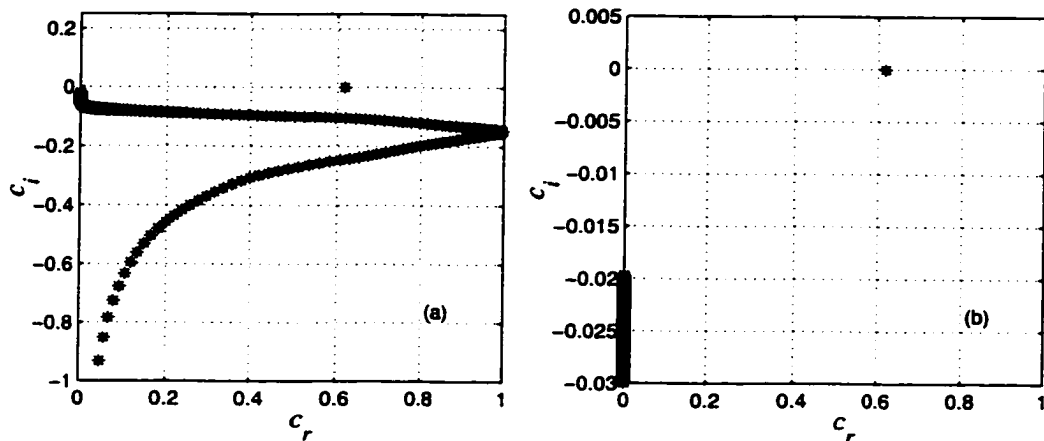


Figure IV.3: Real and imaginary parts of (a) the eigenvalues of (IV.8) at $\alpha_c = 0.201189$ and $k_c = 1.363262549$. (b) The spectrum enlarged to show the region $-0.030 < c_i < 0.005$.

used here. A second order finite difference scheme is used with $N - 1$ grid points so $\delta x = 7.5/N$. In order to accurately do the weakly nonlinear analysis, α_c , k_c , c , and the eigenfunctions must be precisely known. Therefore, c and ϕ_1 are extrapolated from calculations in extended precision (32 significant digits) on grids with $N - 1$, $2N - 1$, and $4N - 1$ points, giving an accuracy of $O(\delta x^6)$. To find α_c and the dispersion relationship, (IV.8) was solved on the three grids using $N = 2500$ ($\delta x = 0.003$) by inverse iteration, which is highly efficient for large tridiagonal systems [Golub and Van Loan, 1996]. From the solutions on the three grids, c and ϕ_1 are extrapolated giving errors of $O(\delta x^6) = 10^{-16}$. A search was performed in (α, k) space to find the pair of values (α_c, k_c) where one eigenvalue has a zero imaginary component, and all the others have negative imaginary components. For the given beach slope and background velocity, the critical values are $\alpha_c = 0.20118961242$ and $k_c = 1.36326254916$. The eigenvalue spectrum is shown in Figure IV.3a. The critical eigenvalue is well separated from the other eigenvalues (Figure IV.3b). The adjoint eigenvalue spectrum at α_c and k_c from (IV.39) is calculated in the same manner and, as expected, is identical to the eigenvalue spectrum of (IV.8).

The numerical value of the maximum nondimensional growth rate at α_c is very close to zero ($\sigma_c(k_c) = k_c c_i = 2 \times 10^{-11}$, corresponding to a dimensional growth time scale of 10^5 years). The points on the dispersion relation (IV.9) near k_c are well fit by a parabola (Figure IV.4, the coefficients of the parabola are given in Table IV.1) indicating that a Taylor series expansion of the dispersion relationship near k_c is valid. Based on the coefficients in Table IV.1, the phase speed at the critical wavenumber is $c = 0.6177536497$ and by (IV.10) the group velocity is $c_g = 0.4906001644$.

Once the critical frictional parameter and wavenumber are known, ϕ_1 is calculated from (IV.8) using α_c and k_c with the same numerical scheme on much denser grids where $N = 10000$ ($\delta x = 7.5 \times 10^{-4}$). Denser grids are used because third derivatives must be accurately calculated to find the coefficients of the complex Ginzburg-Landau equation. The real and imaginary parts of the normalized and extrapolated ϕ_1 are shown in Figure IV.5a. The adjoint function ϕ_1^\dagger , shown in Figure IV.5b, is calculated in a similar manner. The group velocity c_g calculated from (IV.20), where the derivatives of ϕ_1 and the integrals are extrapolated, yields a value of $c_g = 0.4906001572 - i0.35 \times 10^{-8}$. This agrees with the value from the dispersion relationship (IV.10) to 10^{-8} in both the real and imaginary parts, serving as a check of the numerical computations. The functions $\phi_2^{(0)}$ and $\phi_2^{(2)}$ (Figure IV.5c and Figure IV.5e) are calculated from (IV.17) and (IV.21) on grids identical to those used for ϕ_1 with a standard tridiagonal matrix solver, and extrapolated. The function $\phi_2^{(1)}$ is found by solving (IV.19) with a singular value decomposition of the L_1 matrix with $N = 999$ grid points. There is one well isolated zero (10^{-13}) singular value, and the forward and adjoint null vectors of the L_1 matrix are proportional to ϕ_1 and ϕ_1^\dagger . The solution for $\phi_2^{(1)}$ (Figure IV.5d) is constructed by suppressing the homogeneous solution to L_1 . The derivatives of ϕ_1 , $\phi_2^{(0)}$, $\phi_2^{(1)}$, $\phi_2^{(2)}$ and the integrals in (IV.24, IV.25, IV.27) are extrapolated to derive the coefficients of the complex Ginzburg-Landau equation (IV.23), summarized in Table IV.2. The value of δ can also be calculated [Stewartson and Stuart, 1971]

σ	0.123746 - i0.014047
δ	0.088330 + i0.012854
μ	-321.73054 + i407.93056
$ B $	0.019611
Ω	-0.142853

Table IV.2: Coefficients for the complex Ginzburg-Landau equation and solution values.

from the linear dispersion relationship (Figure IV.4 and the dispersion relation coefficients in Table IV.1) by

$$\delta = -\frac{1}{2} \frac{\partial^2 \sigma_c}{\partial k^2} + i \frac{1}{2} \frac{\partial^2 \omega_c}{\partial k^2}.$$

These two estimates of δ agree to three significant digits. The accuracy of the agreement between the two is much smaller than that between the two estimates of c_g (from (IV.10) and (IV.20)), because δ is calculated from (IV.26) where $\phi_2^{(1)}(x)$ is found on a much coarser grid than for example $\phi_1(x)$.

The real part of the Landau coefficient is negative so in this case the instability is supercritical, and finite amplitude equilibration is possible. A solution for the amplitude of the shear wave is sought that has the form (IV.28) with $\Lambda = 0$. The values of B (IV.29) and Ω (IV.30) are given in Table IV.2. The values of μ and δ are such that this solution for $A(\tau, Y)$ is side-band stable (IV.31) for the stated choice of beach slope and base-state alongshore current. For other choices of beach slope and base-state alongshore currents, the instability could be either subcritical or side-band unstable.

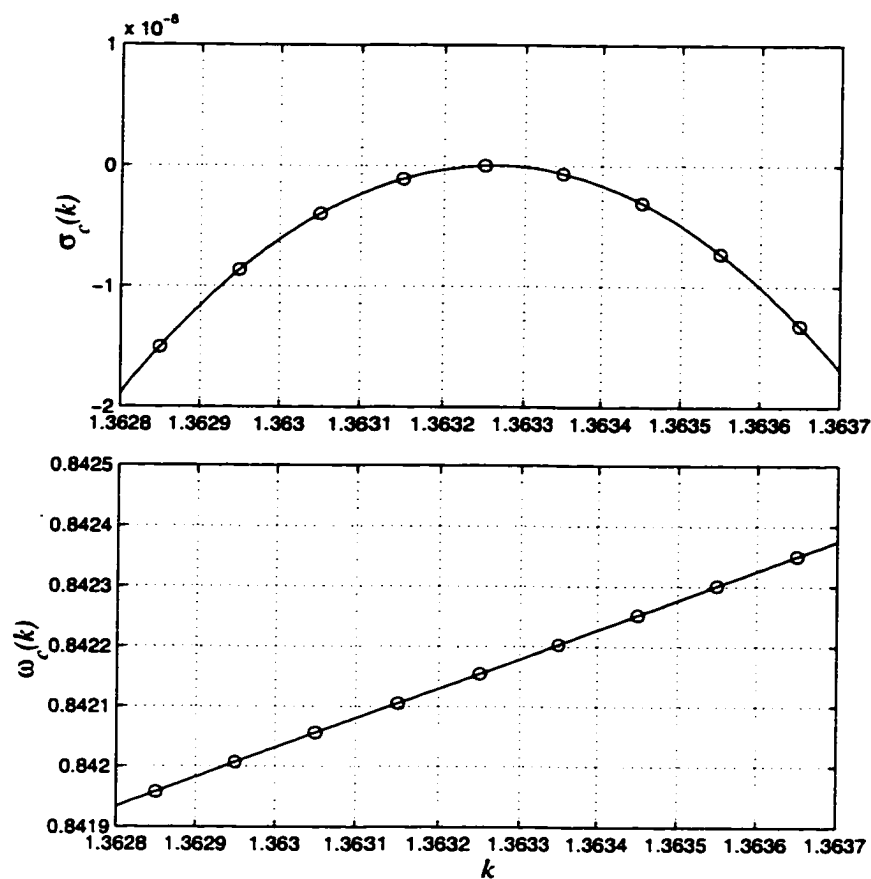


Figure IV.4: The critical dispersion curve for $\omega_c(k) + i\sigma_c(k) = kc$ near the critical wavenumber k . The circles represent calculated values. The solid lines are the best fit parabolas from the coefficients of Table IV.1. The upper panel and lower panel are the curves for $\sigma_c(k)$ and $\omega_c(k)$ respectively.

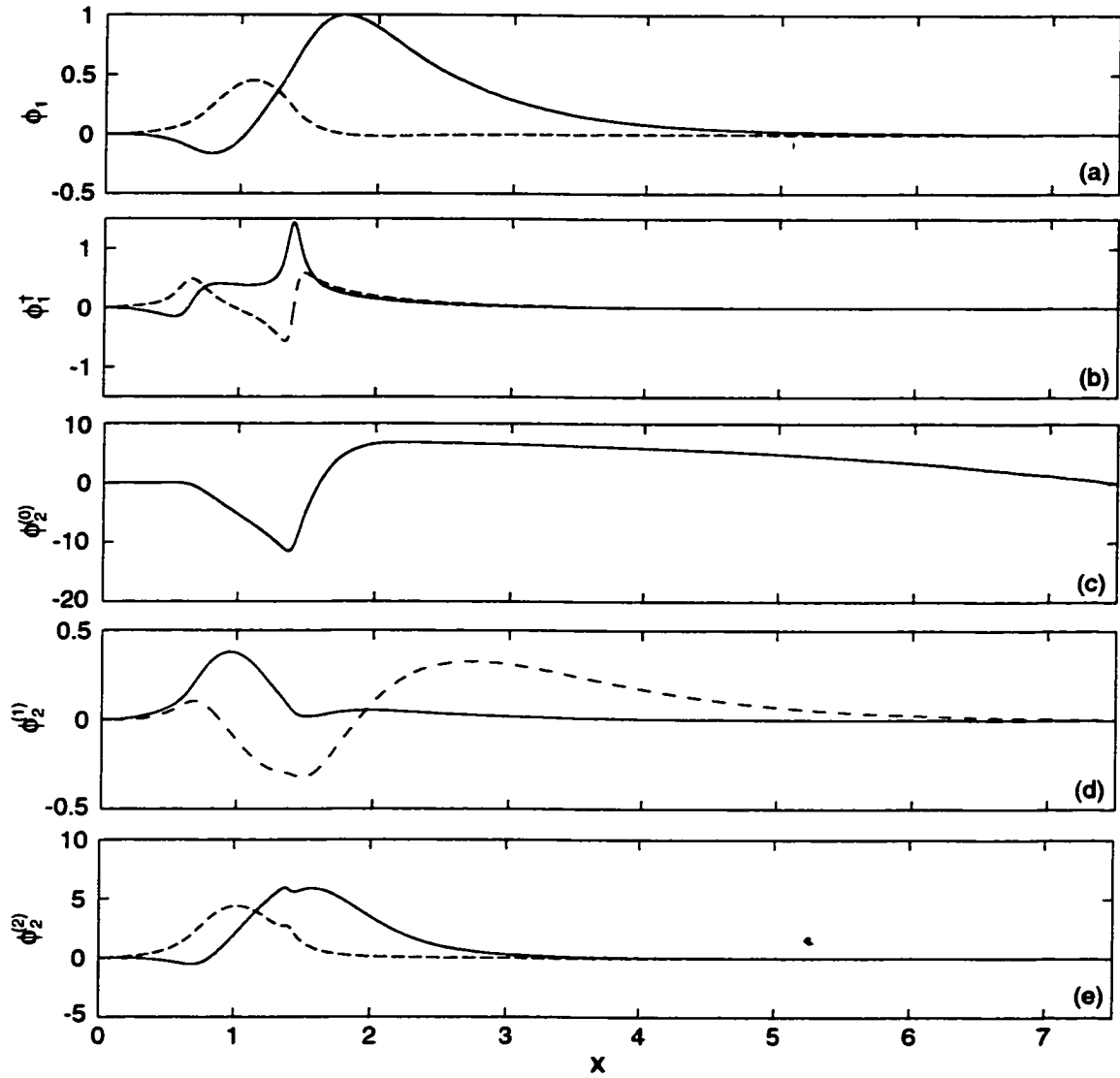


Figure IV.5: The real (solid) and imaginary (dashed) parts of (a) ϕ_1 , (b) ϕ_1^\dagger , (c) $\phi_2^{(0)}$, (d) $\phi_2^{(1)}$, and (e) $\phi_2^{(2)}$.

IV.E Analytic and numerical model comparison

Due to numerical limitations, the near critical behavior of the ANH96 may be distorted. Therefore, analytic and ANH96 numerical results will be compared for the same nondimensional beach profile ($h = x$) and base-state alongshore current (IV.33a) at two values of $\alpha = 0.18$ and 0.17 . There are differences between the two models. The ANH96 model is a second order finite-difference model of essentially the equations (IV.2), but also includes weak biharmonic friction ($-\nu_* \nabla^4 u$ and $-\nu_* \nabla^4 v$ added to the right hand side of (IV.2b) and (IV.2c)) to suppress numerical instabilities. Boundary conditions of no flow into the shoreline and offshore boundary are used. Additional boundary conditions ($u_{xx} = v_x = v_{xxx} = 0$) are required at the shoreline and offshore boundary in the ANH96 model due to the fourth order derivatives in the biharmonic friction terms. The finite difference representation for biharmonic friction and the associated boundary conditions may influence the development of the instability. ANH96 use a numerical resolution with $N = 200$ grid points in x , $M = 90$ points in y , and a nondimensional grid-spacing $\delta x = \delta y = 0.044$. The finite numerical resolution of ANH96 may also mask the near critical behavior [e.g. *Hyman et al.*, 1986].

Periodic boundary conditions are used in the alongshore, and the alongshore domain is slightly longer than the wavelength of the theoretical critical wave, leading to a smaller wavenumber ($k = 1.2566$ vs. $k_c = 1.3632$) for the ANH96 critical wave. Therefore the most unstable wave cannot grow, and an evolution of the instability to smaller wavenumbers is restricted. ANH96 also ran numerical experiments with a alongshore domain three times the wavelength of the most unstable mode and stronger nonlinearity ($\alpha \leq 0.12$ corresponding to $\epsilon > 0.6$), and reported a shift toward lower frequencies and wavenumbers as the instability evolved. For $\alpha = 0.15$ ($\epsilon \approx 0.45$), more strongly nonlinear than the values of α investigated here, steady equilibrated waves with the same frequencies and wavenumber as the experiments with the smaller domains were reported (Figure 7 of ANH96). How-

ever, even on the extended alongshore domain, a potential side-band instability of the shear wave is still suppressed. Due to these limitations of the ANH96 model, the near critical behavior of shear waves may be modeled incorrectly, and for these reasons, the α_c and hence ϵ for the ANH96 model are not accurately known.

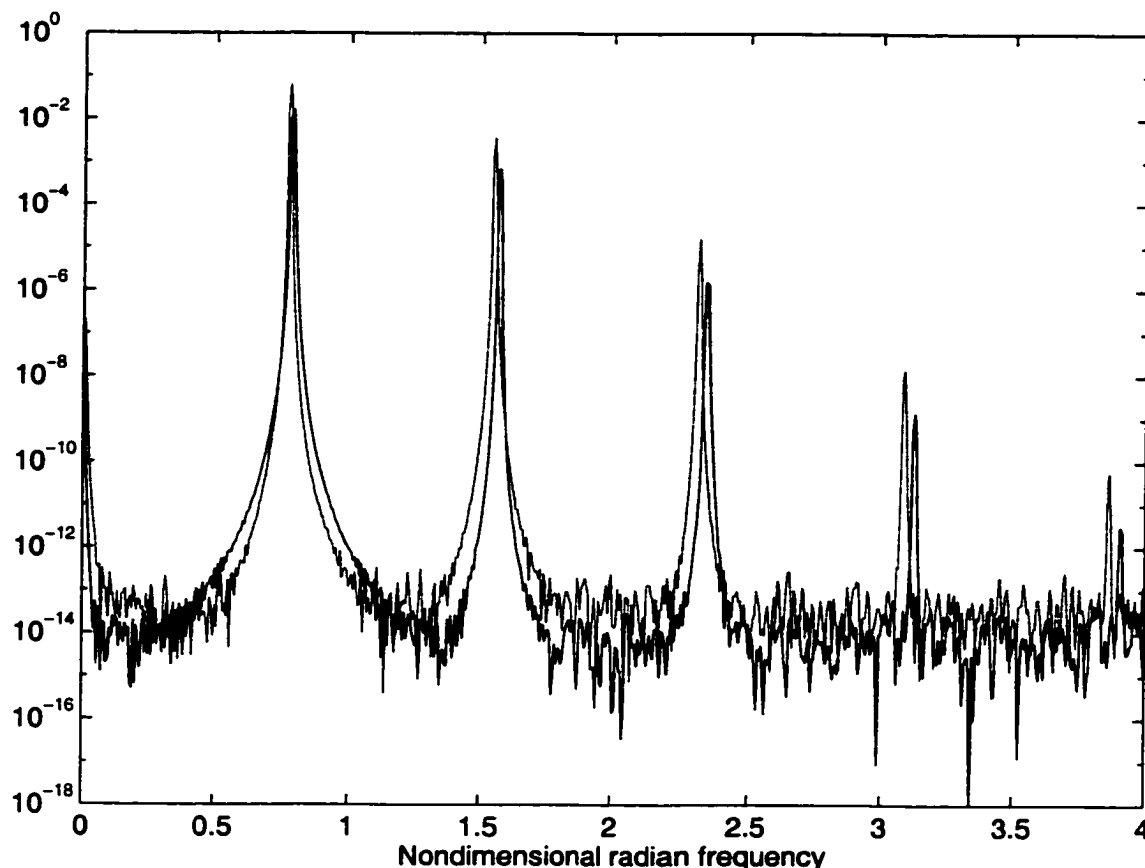


Figure IV.6: Nondimensional spectra of u at $x = 1$ from ANH96 model with $\alpha = 0.17$ (thin line) and 0.18 (bold line).

Before comparing the results of the ANH96 model with the analytic model, it is first verified that the ANH96 model at $\alpha_c = 0.17$ and $\alpha_c = 0.18$ is in a weakly nonlinear regime. For weakly nonlinear waves, the amplitude at the primary frequency a_1 depends linearly on ϵ and the amplitude at the second harmonic a_2 depends on ϵ^2 . Both amplitudes should vanish when $\epsilon = 0$. The α_c is found so that the line going through the (ϵ, a_1) and (ϵ^2, a_2) points have zero y-intercept

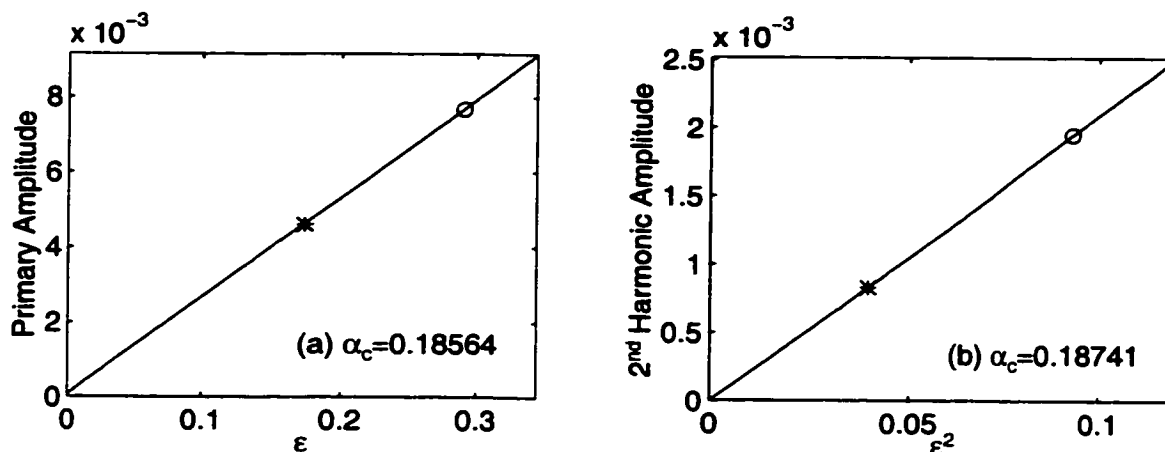


Figure IV.7: (a) The ANH96 model peak amplitude at the primary frequency at $x = 1$ versus ϵ for $\alpha = 0.18$ (*) and $\alpha = 0.17$ (o). The inferred $\alpha_c = 0.18564$. (b) The amplitude of the second harmonic versus ϵ^2 . The inferred $\alpha_c = 0.18741$.

(Figure IV.7). The resulting estimates of α_c are quite similar, $\alpha_c = 0.18564$ from the primary frequency and $\alpha_c = 0.18741$ from the second harmonic, confirming confirms the ANH96 model is in a weakly nonlinear regime. Using $\alpha_c = 0.18564$, $\epsilon = 0.174$ for $\alpha = 0.18$ and $\epsilon = 0.290$ for $\alpha = 0.17$.

The choice of α_c feeds back into the all parts of the solution to the weakly nonlinear problem, so it is not possible to use the ANH96 derived α_c to compare results from the ANH96 and analytic models. Therefore, the analytic $\alpha_c = 0.20119$ is used to calculate ϵ for comparison purposes, resulting in $\epsilon = 0.325$ for $\alpha = 0.18$ and $\epsilon = 0.394$ for $\alpha = 0.17$. As will be shown, this leads to reasonable agreement between analytic and ANH96 model amplitudes for the shear waves, and very good agreement for the cross-shore structure of the shear waves.

The spectrum of ANH96 cross-shore velocity at both values of α contains distinct peaks at integer multiples of the primary frequency (Figure IV.6). The primary peak in the spectrum at the weakest nonlinearity ($\alpha = 0.18$) has a dimensional period of 12 minutes. The ANH96 model nondimensional primary frequency $\omega_1 = 0.7822$ is close to the analytical model value $\omega = 0.8421$ at α_c and k_c from lin-

ear stability theory (IV.8). The difference in frequencies is largely attributable to the ANH96 alongshore domain being slightly longer than the critical wavelength. From (IV.8), the smaller wavenumber forced by the domain size corresponds to a frequency $\omega = 0.7899$, close to the ANH96 primary frequency $\omega_1 = 0.7822$.

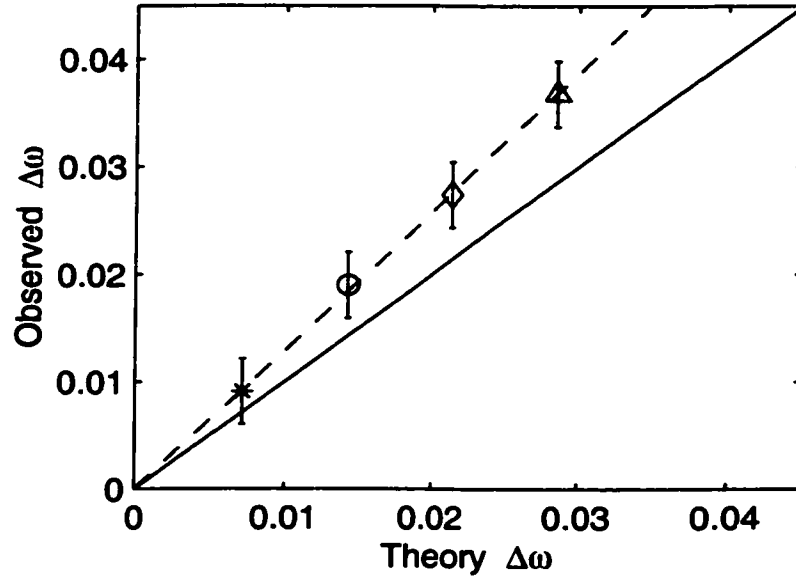


Figure IV.8: The ANH96 derived versus the theoretical change in peak frequency between $\alpha = 0.18$ and $\alpha = 0.17$. Results for the primary frequency (*), second (o), third (◊), and fourth (Δ) harmonic are shown with $\alpha_c = 0.20119$. The error bars (± 0.003) indicate the frequency resolution of the spectrum. The solid line represents perfect ANH96 model-theory agreement. The dashed line is the best fit through the symbols.

The shift to lower frequency in the spectral peaks with decreasing α (Figure IV.6) is consistent with amplitude dispersion. The equilibrated cross-shore velocity at the primary frequency and at a fixed alongshore position is

$$u = \frac{-\epsilon i k}{x} \left(B \phi_1(x) e^{-i(\omega_c + \epsilon^2 \Omega)t} - B^* \phi_1^*(x) e^{i(\omega_c + \epsilon^2 \Omega)t} \right) \quad (\text{IV.34})$$

indicating a finite-amplitude shift of $\epsilon^2 \Omega$ in the primary frequency, where Ω is

given by (IV.30). At the n^{th} harmonic (e.g. $n\omega_1$) the leading order frequency shift is given by $n\epsilon^2\Omega$. Therefore the difference in spectral peak frequencies at $\alpha = 0.18$ and $\alpha = 0.17$ is theoretically $n\Delta\epsilon^2\Omega$, where $\Delta\epsilon^2 = (0.18 - 0.17)/\alpha_c$. The ANH96 observed frequency shift for the first four harmonics at the n^{th} harmonic is n times the primary frequency shift (Figure IV.8), consistent with $O(\epsilon^2)$ amplitude dispersion. However, the magnitude of the ANH96 observed frequency shift is about 30% larger than the analytical model frequency shift.

The equilibrated cross-shore velocity of the ANH96 model at a fixed along-shore position is

$$u(x, t) = U_1(x)e^{i\omega_1 t} + U_2(x)e^{i2\omega_1 t} + c.c + \dots \quad (\text{IV.35})$$

where ω_1 is the primary wave frequency, and $U_1(x)$ and $U_2(x)$ are the Fourier transforms of the ANH96 cross-shore velocities at ω_1 and $2\omega_1$. $U_1(x)$ and $U_2(x)$ are related to the analytic model by

$$U_1(x) = \frac{-\epsilon B^* i k \phi_1^*(x)}{x} \quad (\text{IV.36a})$$

$$U_2(x) = \frac{-\epsilon^2 B^{*2} 2i k \phi_2^{(2)*}(x)}{x}. \quad (\text{IV.36b})$$

The functions $\phi_1(x)$ and $\phi_2^{(2)}(x)$ can therefore be inferred from the ANH96 cross-shore velocity for $\alpha = 0.18$ and $\alpha = 0.17$. The magnitudes of $|\phi_1(x)|$ and $|\phi_2^{(2)}(x)|$ are equal to the square root of the spectrum of u (e.g. Figure IV.6) summed over a small window of frequencies centred on the primary or secondary frequency (to account for spectral leakage) and multiplied by $x/(\epsilon|B|k)$ or $x/(2\epsilon^2|B|^2k)$ respectively. The phases of $\phi_1(x)$ and $\phi_2^{(2)}(x)$ are given within arbitrary constants from the phases of $U_1(x)$ or $U_2(x)$.

Analytic and ANH96 model solutions for $\phi_1(x)$ and for $\phi_2^{(2)}(x)$ are shown in Figures IV.9 and IV.10. The magnitudes of the ANH96 derived $\phi_1(x)$ are in approximate agreement with theory (Figure IV.9a) using the ϵ derived from the analytic α_c . However, when normalized to the same maximum magnitude,

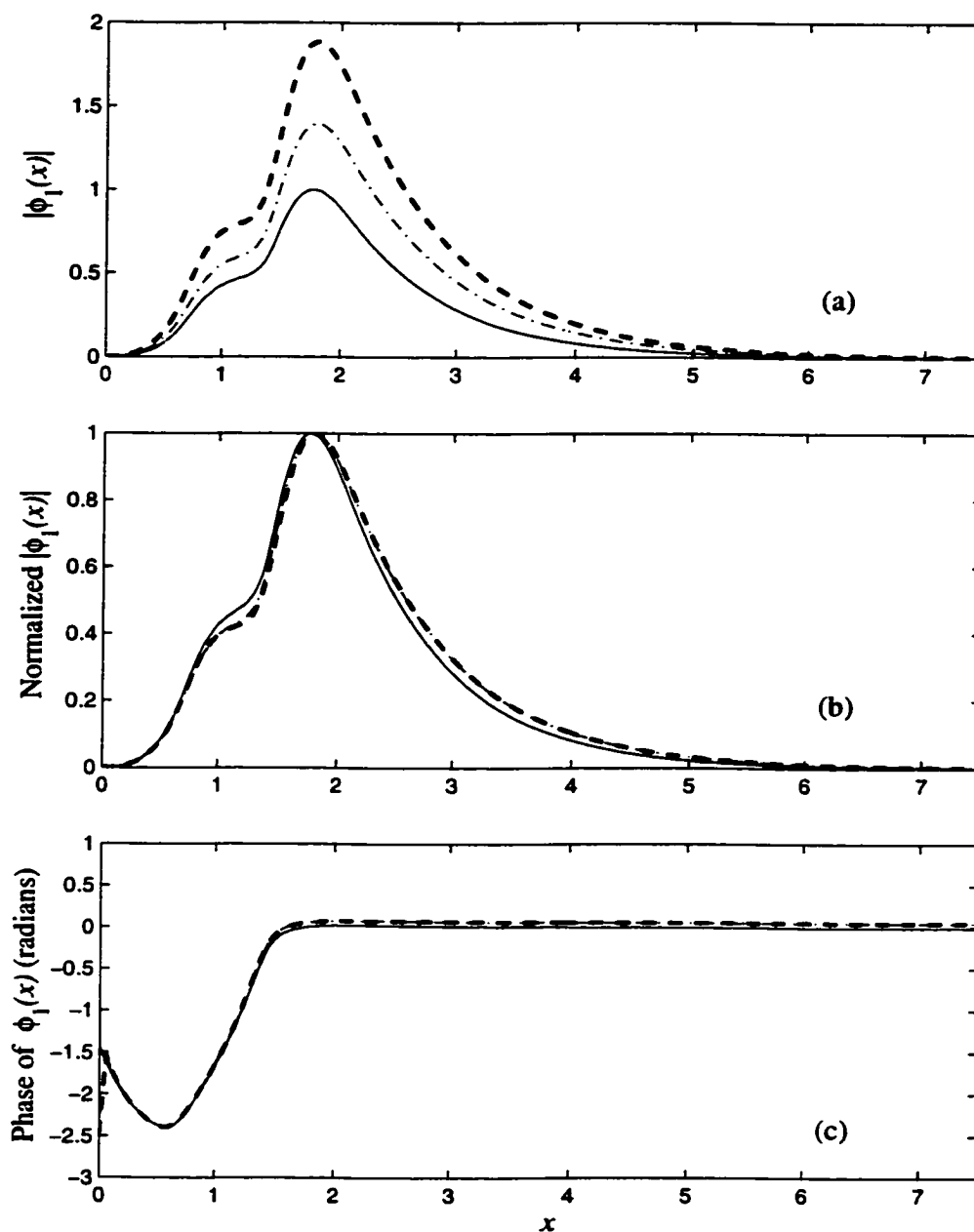


Figure IV.9: (a) $|\phi_1(x)|$ versus nondimensional cross-shore coordinate, x . (b) $|\phi_1(x)|$ normalized (to a maximum magnitude of 1.0) versus x . (c) The phase of $\phi_1(x)$ versus x . In each panel, theory is a solid line, and ANH96 model $\phi_1(x)$ are inferred with $\alpha_c = 0.20119$, and are shown with $\alpha = 0.18$ (dash-dot) and $\alpha = 0.17$ (dashed). The phases are offset so that they are equal at $x = 0.582$.

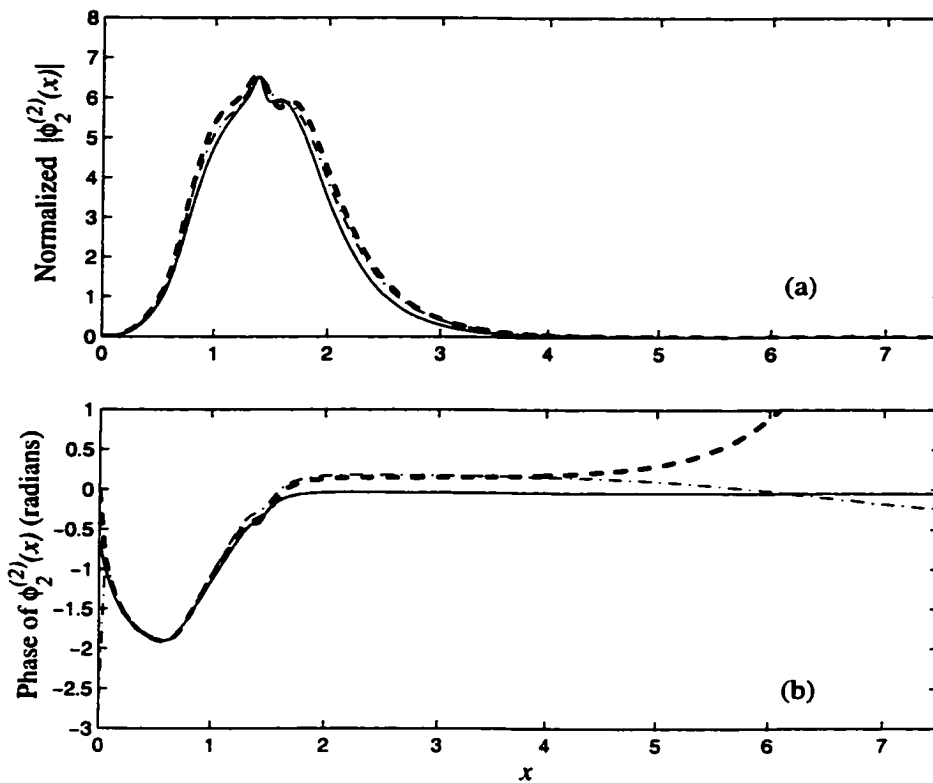


Figure IV.10: (a) $|\phi_2^{(2)}(x)|$ normalized (to the maximum theory magnitude) versus x . (b) The phase of $\phi_2^{(2)}(x)$ versus x . Shown in each panel: theory (solid) and ANH96 model for $\alpha = 0.18$ (dash-dot) and $\alpha = 0.17$ (dashed). The phases are offset so that they are equal at $x = 0.561$.

the cross-shore structure of both the ANH96 inferred and theoretical $|\phi_1(x)|$ and $|\phi_2^{(2)}(x)|$ are in very good agreement for both values of α (Figure IV.9b and IV.10a). The cross-shore phase structure is also in excellent agreement (Figure IV.9c and Figure IV.10b), except near the shoreline where the differences are evidently due to the additional boundary conditions applied to the ANH96 model at the shoreline and the resulting boundary layer from the biharmonic friction. Far offshore ($x > 4$), the phase for $\phi_2^{(2)}(x)$ is in error because the signal is so weak.

The analytic model predicts a mean second order correction $V_c(x)$ to the alongshore current

$$V_c(x) = \frac{\epsilon^2 |B|^2 \phi_{2x}^{(0)}}{x}. \quad (\text{IV.37})$$

The ANH96 correction, defined as the difference between the time mean from the base-state alongshore current $\bar{v}(x) - V(x)$, was calculated for both α . The ϵ^2 -normalized theoretical correction to the alongshore current, $V_c/\epsilon^2 = |B|^2 \phi_{2x}^{(0)}/x$ and the ANH96 correction $(\bar{v} - V)/\epsilon^2$ normalized to the same magnitude are also in very good agreement (Figure IV.11). The differences in the correction near the shoreline is again due to the additional boundary conditions applied there. The effect of the mean flow correction is to reduce the offshore velocity shear by decreasing the velocity at the maximum near $x = 1$ and increasing the velocity further offshore.

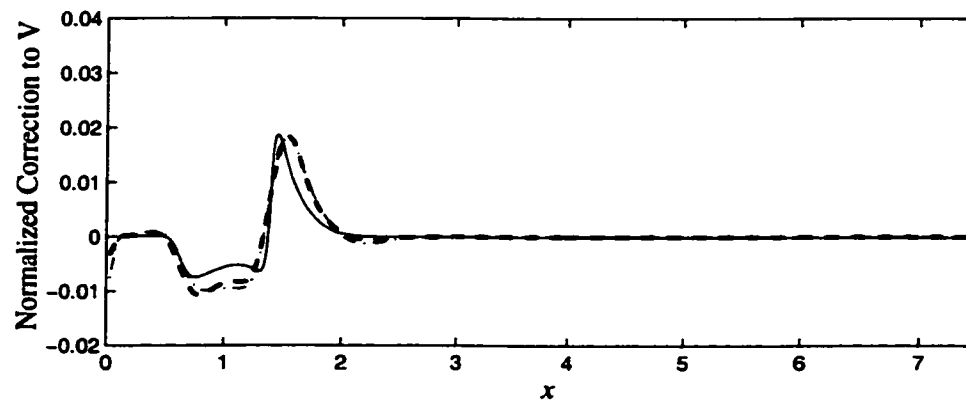


Figure IV.11: The normalized (to have the same maximum magnitude) correction to the mean alongshore current from theory (solid) and ANH96 model for $\alpha = 0.18$ (dash-dot) and $\alpha = 0.17$ (dashed).

IV.F Discussion and Conclusions

Weakly nonlinear shear waves are shown to have characteristics of many other weakly nonlinear wave systems. A standard perturbation expansion is used where the small parameter ϵ is the normalized departure of an inverse Reynolds number α from neutral stability. At $O(\epsilon)$ there is a primary wave with wavenumber k_c , frequency ω_c , and cross-shore structure $\phi_1(x)$ predicted from linear stability theory [e.g. *Bowen and Holman, 1989; Dodd et al. 1992*]. At $O(\epsilon^2)$, a forced wave at twice the frequency and wavenumber ($2\omega_c, 2k_c$) (second harmonic) and a correction to the mean alongshore current are found. At $O(\epsilon^3)$, a complex Ginzburg-Landau equation (IV.23) is derived for the amplitude of the shear wave. This derivation is applicable to a alongshore homogeneous planar beach with arbitrary slope and any prescribed alongshore forcing or base-state alongshore current. For the same base-state alongshore current (IV.33a) and beach slope used in the numerical study of ANH96, the instability is supercritical, and the analytic solution is a side-band stable equilibrated shear wave, with an amplitude-dependent dispersion relationship. Previous work [*Dodd et al., 1992; Putrevu and Svendsen, 1992; Slinn et al., 1998*] suggests that the shear instability is enhanced by a barred-beach profile. The weakly nonlinear analysis can be in principal extended to non-planar beach profiles, however, the character of the instability may be different than the case presented here.

The near critical behavior of shear waves in the ANH96 model may be distorted by numerical effects. Biharmonic friction terms added to prevent numerical instabilities and finite model resolution may alter the character of the instability. Waves longer than the primary wave number are suppressed due to finite domain lengths, therefore a potential sideband instability cannot develop. Numerical limitations also complicate comparison of the analytic to the ANH96 numerical model. However, the ANH96 model at $\alpha = 0.17$ and $\alpha = 0.18$ is shown to be in a weakly nonlinear regime, and the dominant variability is an equilibrated shear wave with

the frequency, wavenumber, and cross-shore structure predicted by linear stability theory. The variability at twice the primary frequency is the second harmonic with the same cross-shore structure as the analytical model. The cross-shore structure of the correction to the mean flow is also in good agreement. Using the analytic α_c , the ANH96 and analytic model shear wave amplitudes are in reasonable agreement, as is the amplitude dispersion. The agreement with the analytical model and ANH96 confirms that the ANH96 model correctly reproduces the qualitative behavior of the weakly nonlinear shear waves for this choice of beach slope and base-state alongshore current.

The numerical modeling of ANH96 and *Slinn et al.* (1998), and the observational work of *Dodd et al.* (1992) suggest a wide range of possible shear wave environments in natural surf zones, ranging from linearly stable, equilibrated shear waves, to strongly turbulent eddy-dominated regimes. Determining whether weakly nonlinear shear waves exist in natural surf zones is beyond the scope of this study. However, the ANH96 chosen base-state alongshore current (IV.32) and beach slope ($\beta = 0.05$) from section 3 are not completely unrealistic parameters for a natural surf zone. With these parameters, the critical inverse Reynolds number $\alpha_c = 0.20119$ leads to a dimensional critical drag coefficient of $\nu_c = 0.01$ m/s. In the idealized bottom stress representation used here, ν can be thought to represent $\nu = c_f \sigma_u$ where c_f is an empirical drag coefficient and σ_u^2 is the orbital wave velocity variance [*Dodd et al.*, 1992; *Slinn et al.*, 1998]. Using a cited range of c_f in the surf zone from 0.01 - 0.001 [e.g. *Garcez-Faria et al.*, 1998] and a significant wave height $H_{sig} = 1$ m in 2 m water depth with linear surface gravity wave theory which gives $\sigma_u \approx 0.8$ m/s, yields a plausible range of ν from 0.008 - 0.0008 m/s. Given the caveats that the bottom stress representations is crude and the forcing idealized, it appears that the value of $\nu_c = 0.01$ m/s required for stability in this hypothetical case is not entirely unrealistic for natural surf zones, and also suggests that a natural surf zone could possibly be in a linearly stable or in a weakly nonlinear regime.

Shear wave energy in field data [e.g. *Oltman-Shay et al.*, 1989]; *Dodd et al.*, 1992], appears as an approximately dispersionless band in frequency-wavenumber spectra. Beyond this, little is known about the characteristics of shear waves in natural surf zones. Future analyses and observations may better characterize surf zone shear wave environments. If shear waves are weakly nonlinear equilibrated linear modes, this might be elucidated with bispectral analysis [e.g. *Elgar and Guza*, 1985] because in the weakly nonlinear limit, the wave at 2ω and $2k$ is bound to the primary wave at ω and k . Future theoretical and observational study could include investigating possible resonances between modes, either leading to explosive instabilities [*Shira et al.*, 1997] or a coupled set of amplitude equations.

IV.G Appendix A: The Adjoint Operator

The adjoint operator, L_1^\dagger and the adjoint function ϕ_1^\dagger to the linear operator L_1 are defined as

$$\int_0^\infty \phi_1^\dagger L_1[\phi_1] dx = \int_0^\infty \phi_1 L_1^\dagger[\phi_1^\dagger] dx = 0 \quad (\text{IV.38})$$

with $L_1[\phi_1]$ given by (IV.18) with $n = 1$ and the boundary conditions, $\phi_1 = 0$ at $x = 0$ and $x = \infty$. Integrating by parts yields:

$$\begin{aligned} L^\dagger[\phi_1^\dagger] &= \left(V - \frac{i\alpha_c}{k_c x} - c \right) \phi_{1xx}^\dagger + \left(2V_x + \frac{V}{x} - \frac{c}{x} \right) \phi_{1x}^\dagger - \left(xQ_x - \frac{i\alpha_c}{k_c x} \left(k_c^2 + \frac{2}{x^2} \right) \right. \\ &\quad \left. + V \left(k_c^2 + \frac{1}{x^2} \right) - \frac{V_x}{x} - V_{xx} - c \left(k_c^2 + \frac{1}{x^2} \right) \right) \phi_1^\dagger = 0. \end{aligned} \quad (\text{IV.39})$$

with the boundary conditions $\phi_1^\dagger = 0$ at $x = 0$ and ∞ . The adjoint ϕ_1^\dagger is solved at the critical wavenumber, k_c and critical friction parameter, α_c . The adjoint operator L^\dagger must and does have the same eigenvalue spectrum as the linear operator L_1 .

IV.H Appendix B: Asymptotics

The asymptotic nature of the linear eigenvalue problem near the beach ($x = 0$) is examined where the dimensional water depth, $h \rightarrow 0$. The solution of linear eigenvalue problem should be analytic near the shoreline and match the prescribed boundary condition, $\phi_1 = 0$. The nondimensional velocity used by ANH96 (IV.33a) and resulting potential vorticity gradient are expanded around $x = 0$. The stability equation (IV.8) is rewritten

$$\begin{aligned} \phi_{1xx} - \frac{\phi_{1x}}{x} - k^2\phi_1 &= \frac{(Q_o x^3 \phi_1 - \frac{i\alpha}{kx^2} \phi_{1x})(V_o x^2 - c + \frac{i\alpha}{kx})}{(V_o x^2 - c - \frac{i\alpha}{kx})(V_o x^2 - c + \frac{i\alpha}{kx})} \\ &= \lambda_1(x)\phi_1 + i\lambda_2(x)\phi_{1x} + \phi_{1x}/x \end{aligned}$$

where $\lambda_1(x)$ and $\lambda_2(x)$ are analytic functions near $x = 0$. The origin is a regular singular point. Expanding in a Frobenius series, the indicial exponents are 0 and 3. The latter gives a nonsingular solution that satisfies the boundary condition, $\phi_1(0) = 0$.

The asymptotic behavior as $x \rightarrow \infty$ is also of interest because the solution for ϕ_1 should match the boundary condition of $\phi_1(\infty) = 0$, in checking the numerical solution for ϕ_1 and helping to choose the proper numerical domain. As $x \rightarrow \infty$, terms that are proportional to V and Q_x can be ignored since both have leading order behavior $\exp(-2x^3/3)$. The equation becomes

$$\left(c + \frac{i\alpha}{kx}\right) \phi_{1xx} - \left(c + \frac{2i\alpha}{kx}\right) \frac{\phi_{1x}}{x} - \left(c + \frac{i\alpha}{kx}\right) k^2 \phi_1 = 0,$$

which has an irregular singular point at $x = \infty$. Substituting $\phi_1 = e^{S(x)}$, standard asymptotic methods are used to determine that to leading order $S \sim -kx + 1/2 \ln x$ thus

$$\phi_1 \sim x^{1/2} \exp(-kx).$$

Note that this leading order result is independent of both the eigenvalue c and α .

Acknowledgments

Funding for this study was provided by ONR Coastal Sciences and AASert programs, and California Sea Grant. The author appreciates the help of John Allen and Priscilla Newberger in providing output from their model. Glenn Ierley and Bob Guza provided sage advice on many occasions, and Paola Cessi taught the class that inspired this work.

This chapter, in full, is a reprint of Feddersen, F., Weakly nonlinear shear waves, *J. Fluid Mech.*, **372**, 71–91, 1998.

IV.I References

- Allen, J.S., Newberger P. A., and Holman R. A. , Nonlinear shear instabilities of alongshore currents on plane beaches, *J. Fluid Mech.*, **310**, 181–213, 1996.
- Benjamin, T. B., and Feir, J. E., The disintegration of wave trains on deep water, *J. Fluid Mech.*, **27**, 417–430, 1967.
- Bowen, A. J., and Holman, R. A., Shear instabilities of the mean longshore current, 1. Theory, *J. Geophys. Res.*, **94**, 18,023–18,030, 1989.
- Craik, A. D. D., *Wave Interactions and Fluid Flows*, Cambridge University Press, 322+xii pp., 1989.
- Dodd, N., Oltman-Shay, J., and Thornton, E. B., Shear instabilities in the longshore current: a comparison of observation and theory, *J. Phys. Oceanogr.*, **22**, 62–82, 1992.
- Dodd, N., and Thornton, E. B., Longshore current instabilities: growth to finite amplitude, *Proc. 23rd Intl. Conf. Coastal Eng.*, pp. 2644–2668, ASCE, 1992.
- Elgar, S., and Guza, R. T., Observations of bispectra of shoaling surface gravity waves, *J. Fluid Mech.*, **161**, 425–448, 1985.
- Falques, A., and Iranzo, V., Numerical simulation of vorticity waves in the nearshore, *J. Geophys. Res.*, **99**, 825–841, 1994.
- Garcez Faria, A. F., Thornton, E. B., Stanton, T. P., Soares, C. M., and Lippmann, T. C., Vertical profiles of longshore currents and related bed shear stress and bottom roughness, *J. Geophys. Res.*, **103**, 3217–3232, 1998.
- Golub, G. H., and Van Loan, C. F., *Matrix Computations, 3rd ed.* John Hopkins University Press, 1996.
- Hyman, J. M., Nicolaenko, B., and Zaleski S., Order and complexity in the Kuramoto-Sivashinsky model of weakly turbulent interfaces, *Physica D*, **23**, 265–292, 1986.
- Manneville, P., *Dissipative Structures and Weak Turbulence.* Academic Press, 1990.
- Oltman-Shay, J., Howd, P. A., and Birkemeier, W. A., Shear instabilities of the mean longshore current, 2. Field data, *J. Geophys. Res.*, **94**, 18,031–18042, 1992.

- Özkan, H. T., and Kirby, J. T., Finite amplitude shear wave instabilities, *Proc. Coastal Dynamics 1995*, pp. 465–476, ASCE, 1995.
- Putrevu, U., and Svendsen, I. A., Shear instability of longshore currents: A numerical study, *J. Geophys. Res.*, **97**, 7283–7302, 1992.
- Shrira, V. I., Voronovich, V. V., and Kozhelupova, N. G., Explosive instability of vorticity waves, *J. Phys. Oceanogr.*, **27**, 542–554, 1997.
- Slinn, D. N., Allen, J. S., Newberger, P. A., and Holman, R. A., Nonlinear shear instabilities of alongshore currents over barred beaches, *J. Geophys. Res.*, **103**, 18,357–18,379, 1998.
- Stewartson, K., and Stuart, J. T., A non-linear instability theory for a wave system in plane Poiseuille flow, *J. Fluid Mech.*, **48**, 529–545, 1971.
- Stuart, J. T., and DiPrima, R. C., The Eckhaus and Benjamin-Feir resonance mechanisms, *Proc. R. Soc. Lond. A.*, **362**, 27–41, 1978
- Thornton, E. B., and Guza, R. T., Surf zone longshore currents and random waves: field data and models, *J. Phys. Oceanogr.*, **16**, 1165–1178, 1986

Chapter V

Numerical Models for Nearshore Circulation: A progress report

V.A Introduction

Nearshore circulation dynamics can be elucidated by numerical models. For example, characteristics of finite amplitude shear waves have been studied with a 2-D nearshore circulation model [e.g. *Allen et al.*, 1996 - hereafter ANH96], and these model results have been verified by comparison to theory *Feddersen* [1998 - Chapter 4]. My future work will involve a 2-D nearshore circulation model. Instead of using a model developed elsewhere, I began development of my own model, for reasons utilitarian, pedagogical, and selfish. While further work is required to make it suitable for general use, the rigid-lid shallow water model is now suitable for study of shear-instabilities (similar to ANH96). The modeling techniques are standard for ocean and coastal modeling (e.g. the POM model, *Mellor et al.* [1996], ANH96) and are closely related to techniques used for incompressible 2-D flow [*Harlow and Welch*, 1965; *Gresho and Sani*, 1987]. Here, the model implementation and validation are described.

V.B Governing Equations

The rigid-lid, forced, and dissipative shallow water equations (continuity, cross- and alongshore momentum) that form the basis of the model are (ANH96),

$$(hu)_x + (hv)_y = 0 \quad (\text{V.1a})$$

$$u_t + uu_x + vv_y = -g\eta_x + F^{(x)}/h - \mu u/h - \nu \nabla^4 u \quad (\text{V.1b})$$

$$v_t + uv_x + vv_y = -g\eta_y + F^{(y)}/h - \mu v/h - \nu \nabla^4 v \quad (\text{V.1c})$$

where h is the water depth, x and y are cross- and alongshore coordinates, u and v are cross- and alongshore depth- and time-averaged velocities, η is the time-averaged free surface elevation, and μ is a Rayleigh drag coefficient. Since the flow is assumed hydrostatic, η and pressure are used interchangeably here. Biharmonic friction (i.e. $\nu \nabla^4 u$) is included to provide damping at high wavenumbers in order to prevent nonlinear instability, and ν is the hyperviscosity.

V.C The Staggered C-Grid and discretization

These equations (V.1) are discretized on a staggered C-Grid [Harlow and Welch, 1965] with grid spacing Δx and Δy (Figure V.1), and cross- and alongshore model domain sizes $L^{(x)}$ and $L^{(y)}$. On a C-grid u is defined at $(i\Delta x, j\Delta y)$ (which includes the shoreline and offshore boundaries) where $i = 0, 1, \dots, N^{(x)} - 1$, and $j = 0, 1, \dots, N^{(y)} - 1$, with $N^{(x)} = L^{(x)}/\Delta x + 1$ and $N^{(y)} = L^{(y)}/\Delta y$. The depth and η are defined at the same alongshore locations as u , but staggered half a cross-shore grid step, that is at $(i\Delta x + 1/2, j\Delta y)$, where $i = 0, 1, \dots, N^{(x)} - 2$ and $j = 0, 1, \dots, N^{(y)} - 1$. The alongshore velocity v is staggered alongshore and cross-shore from u , and defined at $(i\Delta x - 1/2, j\Delta y + 1/2)$ where $i = 0, 1, \dots, N^{(x)}$ and $j = 0, \dots, N^{(y)} - 1$. There are a total of $N^{(x)}N^{(y)}$ grid points for u , $(N^{(x)} - 1)N^{(y)}$ grid points for η and h , and $(N^{(x)} + 1)N^{(y)}$ grid points for v .

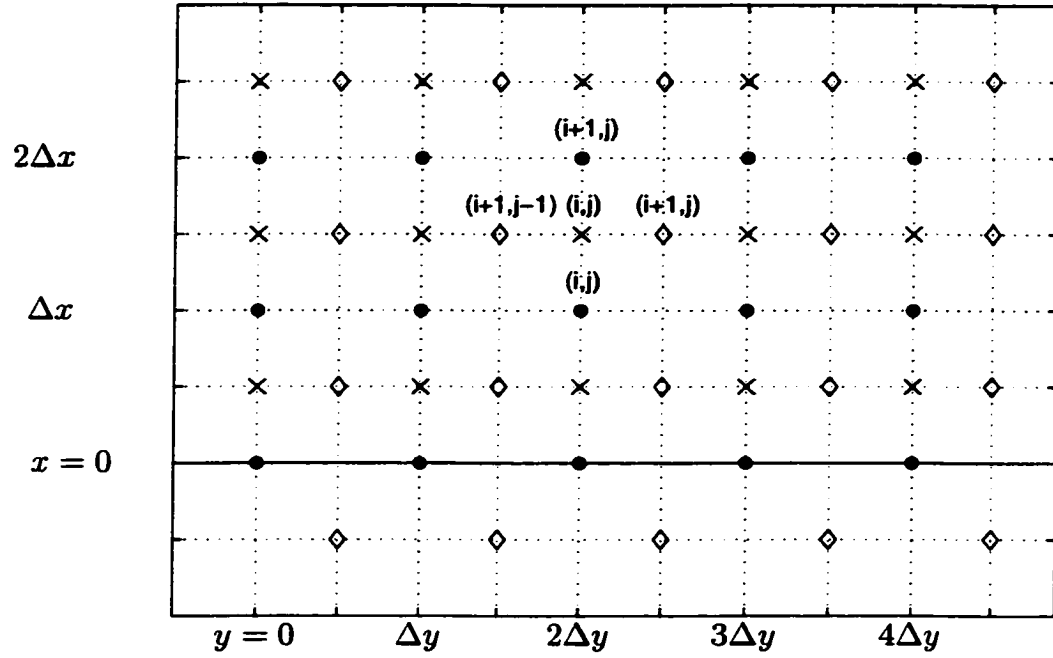


Figure V.1: The locations of u (\bullet), v (\diamond), and η (\times) on the C-grid. The depth and η points are collocated. The solid line represents a boundary to cross-shore flow. The relative indexing scheme used is shown.

The following C-grid finite difference operators are defined:

$$\delta_x \phi = \left[\phi(x + \frac{1}{2}\Delta x) - \phi(x - \frac{1}{2}\Delta x) \right] / \Delta x$$

$$\bar{\phi}^x = \frac{1}{2} \left[\phi(x + \frac{1}{2}\Delta x) + \phi(x - \frac{1}{2}\Delta x) \right]$$

and $\nabla^2 \phi = (\delta_x^2 + \delta_y^2)\phi$.

After multiplication of (V.1b) and (V.1c) by h , the discretized versions of (V.1) are,

$$\delta_x[\bar{h}^x u] + \delta_y[\bar{h}^y v] = 0 \quad (\text{V.2a})$$

$$(\bar{h}^x u)_t + \delta_x[h(\bar{u}^x)^2] + \delta_y[\bar{h}^{xy}(\bar{u}^y \bar{v}^x)] = -g\bar{h}^x \delta_x \eta + F^{(x)} - \mu u - \nu \bar{h}^x \nabla^4 u \quad (\text{V.2b})$$

$$(\bar{h}^y v)_t + \delta_x[\bar{h}^{xy}(\bar{u}^y \bar{v}^x)] + \delta_y[h(\bar{v}^y)^2] = -g\bar{h}^y \delta_y \eta + F^{(y)} - \mu v - \nu \bar{h}^y \nabla^4 v. \quad (\text{V.2c})$$

Note that $\nabla^4 u = \nabla^2(\nabla^2 u)$ in finite-difference form as well. Rotation has been included as a model option by adding

$$-f\bar{h}^x \bar{v}^{xy}, \quad f\bar{h}^y \bar{u}^{xy}$$

to the left-hand side of (V.2b) and (V.2c) respectively.

V.D Velocity Boundary Conditions

Alongshore boundary conditions are periodic. The cross-shore velocity boundary conditions used by ANH96 are

$$u = u_{xx} = v_x = v_{xxx} = 0 \text{ at } x = 0, L^{(x)}.$$

Where do these come from? No flow ($u = 0$) into the cross-shore boundaries is clearly physically motivated, however the others seem arbitrary. ANH96 describe the others as free-slip boundary conditions for biharmonic friction. I believe that this can be interpreted as follows. Writing the biharmonic friction as a divergence of a stress tensor (or equivalently a momentum flux)

$$\nabla^4 \vec{u} = \nabla \cdot \begin{bmatrix} \frac{\partial^3 u}{\partial x^3} + \frac{\partial^3 u}{\partial x \partial y^2} & \frac{\partial^3 u}{\partial y \partial x^2} + \frac{\partial^3 u}{\partial y^3} \\ \frac{\partial^3 v}{\partial x^3} + \frac{\partial^3 v}{\partial x \partial y^2} & \frac{\partial^3 v}{\partial y \partial x^2} + \frac{\partial^3 v}{\partial y^3} \end{bmatrix}.$$

shows that the boundary conditions require that the off-diagonal terms vanish, thus imposing zero shear stress (or zero cross-shore flux of alongshore momentum) at the boundaries. Note that biharmonic friction is not obviously a divergence of a symmetric stress tensor. Is this problem mathematically well posed? These issues will be addressed in the future.

The use of the velocity boundary conditions to a C-grid is rather slick, and may have been a motivation for choosing these boundary conditions. Evaluating the fourth-order derivatives in the biharmonic operator at i typically requires values at $i - 2$, so evaluation at $i = 1$ would require values at $i = -1$ that do not exist. However, the biharmonic term in (V.2b) is $\nabla^2(\nabla^2 u)$, and since $\nabla^2 u$ and u are

known at the boundary ($i = 0$), $\nabla^4 u$ can be evaluated at $i = 1$ using $u = 0$ (which gives $\delta_y^2 u = 0$) and $\nabla^2 u = \delta_x^2 u = 0$ at $i = 0$. The $v_{xxx} = 0$ boundary condition is similarly used to evaluate $\nabla^4 v$ in (V.2c). A nonlinear term in the y -momentum equations

$$\overline{h^{xy} \bar{u}^y \bar{v}^x}$$

must be evaluated at the boundaries. However, since $u = 0$ at the boundaries the depth at the exterior points doesn't need to be evaluated.

V.E Time Stepping and Numerical Stability

A second-order Adams-Bashforth (hereafter AB2) time stepping scheme is implemented,

$$u^{n+1} = u^n + \frac{1}{2} \Delta t (3u_t^n - u_t^{n-1}).$$

The initial time step is just a simple Euler forward step, *i.e.*

$$u^1 = u^0 + \Delta t u_t^0.$$

Since AB2 is a second order scheme for a first derivative, it has both a physical and a computational mode. For the simple wave equation

$$\frac{\partial u}{\partial t} + c \frac{\partial u}{\partial x} = 0 \quad (\text{V.3})$$

the AB2 scheme gives physical and computational mode amplification factors [Messinger and Arakawa, 1976]

$$\begin{aligned} |\lambda_1| &= 1 + \frac{1}{4} p^4 + \dots \\ |\lambda_2| &= \frac{1}{2} p + \dots, \end{aligned}$$

respectively, where $p = c\Delta t/\Delta x$, is a CFL number. The physical mode is therefore unstable for the wave equation but is apparently tolerable (according to Messinger and Arakawa [1976]) when a small p is used. For the friction equation

$$\frac{\partial u}{\partial t} = -\kappa u, \quad (\text{V.4})$$

AB2 is stable and the computational mode is damped for small values of $\kappa\Delta t$. The dissipative shallow water equations are a mix of both wave and friction equations.

A third-order Adams-Bashforth (hereafter AB3) time stepping scheme,

$$u^{n+1} = u^n + \frac{1}{12}\Delta t(23u_t^n - 16u_t^{n-1} + 5u_t^{n-2}),$$

was also implemented. *Durrant* [1991] shows that the physical mode of the wave equation (V.3) is damped and that the two computation modes are damped at $p < 0.676$. At $p \ll 1$, both computation modes are strongly damped and the amplification of the physical mode is

$$|\lambda_1| = 1 - \frac{3}{8}p^4 + O(p^6).$$

For the friction equation (V.4), AB3 requires $\kappa\Delta t < 0.359$ to damp computational modes.

In addition to computational modes for both time-stepping techniques, there are also Von-Neumann stability limits on the sizes of both the CFL ($U\Delta t/\Delta x$) number and $S_\mu = \mu\Delta t/h$ in integrating the momentum equations (U is a characteristic velocity scale).

Biharmonic Friction and Stability

Biharmonic friction is included in the model equations to prevent nonlinear generation of motions at wavelengths less than twice the grid spacing (i.e. the Nyquist wavelength) that are aliased and lead to nonlinear instability. Biharmonic friction performs scale selective damping [*Holland*, 1978], dissipating the shortest scales preferentially, while hopefully not affecting the larger scales (L) of interest. Therefore, the biharmonic Reynolds number should be large at the scales of interest ($R_{bi} = UL^3/\nu \gg 1$), but small at grid scales $R_{bi} = U(\Delta x)^3/\nu \ll 1$ so that sufficient hyper-viscous damping occurs. For each modeling situation, stability is obtained by adjusting ν depending on the U , L , and Δx .

A Von-Neumann stability condition is associated with biharmonic friction.

For the simple equation

$$\frac{\partial u}{\partial t} = -\nu \frac{\partial^4 u}{\partial x^4}$$

that is 2nd order discretized and with a Euler forward time step, conditional stability requires that

$$S_{bi} = \frac{\nu \Delta t}{(\Delta x)^4} < \frac{1}{8}.$$

For the 2-D equation

$$\frac{\partial u}{\partial t} = -\nu \nabla^4 u$$

the condition is much more stringent, $S_{bi} < 1/128$. The biharmonic friction stability constraints on S_{bi} for AB2 and AB3 are not certain, but similar restrictions for both schemes are expected.

V.F The Pressure Equation

The pressure (equivilently η) adjusts to satisfy the continuity equation (*Gresho and Sani, 1987*). An elliptic equation for the pressure follows from requiring that the time derivative of the continuity equation is zero,

$$\frac{\partial}{\partial t} \nabla \cdot (h\mathbf{u}) = 0 \quad (\text{V.5})$$

which, with an initial condition \mathbf{u}_0 satisfying $\nabla \cdot (h\mathbf{u}_0) = 0$, guarantees that continuity is satisfied for all $t > 0$. The enforcement of (V.5) is ensured by taking the divergence of the momentum equations, and using (V.5) to obtain a Poisson pressure equation:

$$\nabla \cdot (h\nabla\eta) = f(x, y) = \nabla \cdot s(x, y), \quad (\text{V.6})$$

which is solved at each time step to update η . This technique is common for shallow water, primitive equation, and incompressible flow modeling. The discretized

version of the Poisson pressure equation (V.6) is derived from the discretized SWE (not directly from the continuous equation - otherwise mass is not conserved) by using the discrete analogy of the divergence, δ_x (V.2b) + δ_y (V.2c),

$$g[\delta_x(\bar{h}^x \delta_x \eta) + \delta_y(\bar{h}^y \delta_y \eta)] = -\delta_x^2[h(\bar{u}^x)^2] - 2\delta_x \delta_y[\bar{h}^{xy}(\bar{u}^y \bar{v}^x)] - \delta_y^2[h(\bar{v}^y)^2] \\ -\mu[\delta_x u + \delta_y v] + [\delta_x F^{(x)} + \delta_y F^{(y)}] - \nu[\delta_x(\bar{h}_x \delta^4 u) + \delta_y(\bar{h}_y \delta^4 v)] \quad (V.7)$$

Before deriving the discrete boundary conditions for η required to solve (V.7), the boundary conditions required for solution in the continuous problem are discussed.

Pressure Equation Boundary Conditions

Boundary conditions for (V.6) must be chosen to allow a solution. Integrating both sides of (V.6) over the domain R and using the divergence theorem yields

$$\int_R \nabla \cdot (h \nabla \eta) dA = \oint_{\partial R} h \nabla \eta \cdot \hat{\mathbf{n}} dl$$

and

$$\int_R f(x, y) dA = \oint_{\partial R} s \cdot \hat{\mathbf{n}} dl$$

where $\hat{\mathbf{n}}$ is the outward normal on ∂R , the boundary of R . For a solution to (V.6) to exist the Neumann boundary conditions (e.g. conditions on the gradient) must be of the form

$$\oint_{\partial R} h \nabla \eta \cdot \hat{\mathbf{n}} dl = \oint_{\partial R} s \cdot \hat{\mathbf{n}} dl$$

on ∂R . A satisfactory condition is

$$h \nabla \eta \cdot \hat{\mathbf{n}} = s(x, y) \cdot \hat{\mathbf{n}} \quad (V.8)$$

everywhere on ∂R , where $s(x, y)$ is the boundary normal component of the momentum equation.

The boundary conditions in the alongshore direction (y) are periodic and give no contribution to the boundary integral. The continuous cross-shore momentum equation and the velocity boundary conditions $u = u_{xx} = 0$ at $x = 0, L^x$ yield

$$gh\eta_x = F^{(x)} - h\nu u_{xxxx}. \quad (\text{V.9})$$

This boundary condition (V.9) allows for a solution to (V.6), but does not lead to a unique solution (no Neumann boundary condition will) since η equal to a constant satisfies the homogeneous part of (V.7).

Finite Difference BC Application

Application of the continuous boundary conditions (V.9) to the C-grid is not possible since neither η_x nor u_{xxxx} are defined on the C-grid boundary. The boundary condition can be applied one grid point in the interior. Applying the same idea (V.8) for the solvability condition gives the boundary condition,

$$g\bar{h}^x \delta_x \eta = -(\bar{h}^x u)_t - \delta_x [h(\bar{u}^x)^2] + -\delta_y [\bar{h}^{xy} (\bar{u}^y \bar{v}^x)] + F^{(x)} - \mu u - \nu \bar{h}^x \nabla^4 u$$

to be evaluated at time step $n + 1$. All the terms on the RHS of the above equation can be evaluated *except* u_t , and while is technically correct, it is useless without knowledge of u_t . If u_t is ignored, the continuity equation is violated (as I discovered). A usable discrete pressure boundary condition thus cannot be obtained by analogy to the continuous case.

The appropriate discrete pressure boundary condition is instead derived by enforcing mass conservation at the first interior pressure grid points [*Gresho and Sani, 1987*]. If the velocity initial condition is divergence free, then ensuring that $\nabla \cdot (hu_t) = 0$ near the boundary guarantees mass conservation. Written out at the near-shoreline boundary (overdot indicates a time derivative, and for notational convenience $\Delta = \Delta x = \Delta y$)

$$\frac{\bar{h}^x \dot{u}_{1,j} - \bar{h}^x \dot{u}_{0,j}}{\Delta} + \frac{\bar{h}^y \dot{v}_{1/2,j+1/2} - \bar{h}^y \dot{v}_{1/2,j-1/2}}{\Delta} = 0. \quad (\text{V.10})$$

The individual terms in (V.10) are (without writing the nonlinear terms)

$$\begin{aligned}\bar{h}^x \dot{u}_{1,j} &= -g\bar{h}^x \frac{\eta_{3/2,j} - \eta_{1/2,j}}{\Delta} - \mu u_{i,j} - \nu \bar{h}^x \nabla^4 u_{i,j} + F_{1,j}^{(x)} \\ \bar{h}^x \dot{u}_{0,j} &= 0 \\ \bar{h}^y \dot{v}_{1/2,j+1/2} &= -g\bar{h}^y \frac{\eta_{1/2,j+1} - \eta_{1/2,j}}{\Delta} - \mu v_{1/2,j+1/2} - \nu \bar{h}^y \nabla^4 v_{1/2,j+1/2} + F_{1/2,j+1/2}^{(y)} \\ \bar{h}^y \dot{v}_{1/2,j-1/2} &= -g\bar{h}^y \frac{\eta_{1/2,j} - \eta_{1/2,j-1}}{\Delta} - \mu v_{1/2,j-1/2} - \nu \bar{h}^y \nabla^4 v_{1/2,j-1/2} + F_{1/2,j-1/2}^{(y)},\end{aligned}$$

and (V.10) gives

$$g\bar{h}^x \frac{\eta_{3/2,j} - \eta_{1/2,j}}{\Delta^2} + g\delta_y(\bar{h}^y \delta_y \eta_{1/2,j}) = B_j(u, v) \quad (\text{V.11})$$

at the shoreline and

$$g\bar{h}^x \frac{\eta_{N-3/2,j} - \eta_{N-1/2,j}}{\Delta^2} + g\delta_y(\bar{h}^y \delta_y \eta_{N-1/2,j}) = C_j(u, v) \quad (\text{V.12})$$

at the offshore boundary ($N = N^{(x)} - 1$, the number of cross-shore η grid points) where B_j and C_j represent all the terms not a function of η . These pressure boundary conditions insure mass conservation and guarantee a solution.

Pressure Equation Discretization

The discrete version of the Poisson pressure equation (V.7) is

$$\begin{aligned}& \frac{g}{2\Delta^2} [-(4h_{ij} + h_{i+1,j} + h_{i-1,j} + h_{i,j-1} + h_{i,j+1})\eta_{i,j} \\ & + (h_{i+1,j} + h_{ij})\eta_{i+1,j} + (h_{ij} + h_{i-1,j})\eta_{i-1,j} \\ & + (h_{i,j+1} + h_{ij})\eta_{i,j+1} + (h_{ij} + h_{i,j-1})\eta_{i,j-1}] \\ & = R_{ij}\end{aligned} \quad (\text{V.13})$$

where $i = 3/2, \dots, N - 3/2$, and R_{ij} is given by the RHS of (V.7). The boundary conditions (V.11) and (V.12), and (V.13) yield a matrix equation

$$A\eta = b$$

where A is block diagonal. There are two difficulties solving this matrix problem:

1) The size of the matrix A is HUGE! If the model domain is $N \times M$ points then the matrix A is roughly $NM \times NM$. For a modest domain size of $N = M = 100$, A is $10^4 \times 10^4$ which in double precision requires roughly 800 Mb of storage, beyond anything but a supercomputer. There are two classes of algorithms to solve the matrix equation, direct methods that take advantage of the special structure of A (FACR), and iterative methods which exploit the sparse structure of A (Conjugate-Gradient and Multigrid algorithms).

2) The matrix A is singular with one zero eigenvalue. The boundary conditions specify η_x and not η , because only pressure gradients matter in the momentum equations. Therefore, the pressure is indeterminate up to a constant. A unique solution is chosen by assigning a value of zero to an anchor point (a single point in the domain or an entire Fourier coefficient). The matrix is reduced in size by one, and becomes block diagonal with full rank, which can be solved as described below.

FACR

With FACR (Fourier Transform, Cyclic Reduction), (V.7) and the boundary conditions are Fourier transformed in the alongshore direction. This is only possible if (V.7) and the boundary conditions are constant coefficient in the alongshore direction. The resulting tri-diagonal equation at each wavenumber can be rapidly solved with minimal storage.

The Fourier series of η is

$$\eta_{ij} = \frac{1}{NY} \sum_{k=0}^{NY-1} \hat{\eta}_{ik} \exp\left(i \frac{2\pi}{NY} jk\right)$$

where $\hat{\eta}_{ik}$ is the Fourier coefficients, and $i = \sqrt{-1}$. The Fourier representation of the pressure equation (V.13) is

$$\begin{aligned} \frac{g}{2\Delta^2} [(h_i + h_{i-1})\hat{\eta}_{i-1,k} + [(4 \cos(2\pi k/NY) - 6)h_i - (h_{i-1} + h_{i+1})]\hat{\eta}_{ik} \\ + (h_i + h_{i+1})\hat{\eta}_{i+1,k}] = \hat{R}_{ik} \end{aligned} \quad (\text{V.14})$$

where the grid spacing in x and y are assumed equal, $h_{ij} = h_i$ (since $h = h(x)$), and \hat{R}_{ik} is the Fourier transform of the right hand side of (V.13). The indexing for η and h is redefined from $i = 1, \dots, N$ for convenience. The above equation is applied on points $i = 2, \dots, N - 1$.

The near-shoreline pressure boundary condition (V.11) is

$$g \frac{h_1 + h_2}{2\Delta^2} (\eta_{2,j} - \eta_{1,j}) + g \frac{h_1}{\Delta^2} (\eta_{1,j+1} - 2\eta_{1,j} + \eta_{1,j-1}) = B_j,$$

and Fourier transformed yields

$$\frac{h_1 + h_2}{2} \hat{\eta}_{2,k} + \left[2h_1 (\cos(2\pi k/NY) - 1) - \frac{h_1 + h_2}{2} \right] \hat{\eta}_{1,k} = \Delta^2 \hat{B}_k / g. \quad (\text{V.15})$$

The offshore boundary condition is similarly Fourier transformed. At $i = 2$ and $i = N - 1$, (V.15) is substituted into (V.14) to eliminate $\hat{\eta}_{1,k}$ and $\hat{\eta}_{N,k}$ from the equations.

The equations at $i = 2$ and $i = N - 1$ along with (V.14) at $i = 3, \dots, N - 2$ give a tri-diagonal system for each k that can be solved rapidly. There are $N - 2$ equations in $N - 2$ unknowns. The $k = 0$ matrix is still rank deficient, because any constant can be added to the solution, and in this case the $N - 3$ by $N - 3$ submatrix is solved by setting the anchor point $\hat{\eta}_{N-1,0} = 0$. The constraint $\int \eta dx dy = 0$ is satisfied by adjusting $\hat{\eta}_{i,0}$ so that $\int \hat{\eta}_{i,0} dx = 0$. Inverse Fourier transforming gives η_{ik} .

Summary of Pressure Solving Algorithm

I found that solving (V.7) for η was the most challenging part of the developing the model. A summary sketch of the algorithm I used is:

- Set up the rhs of (V.7) and boundary conditions (V.11) and (V.12)
- Fourier transform these in the alongshore direction
- Loop over wavenumber k , from $k = 0$ to the Nyquist
- generate the $N - 2$ by $N - 2$ tri-diagonal matrix for each k

- At $k = 0$, solve the $N - 3$ by $N - 3$ submatrix by setting $\hat{\eta}_{N-1,0} = 0$. At other wavenumbers solve the $N - 2$ by $N - 2$ system.
- Inverse FFT. Use BC to solve for $\eta_{1,j}$ and $\eta_{N,j}$
- Remove any mean from η .

Methods for Arbitrary Bathymetry

When the depth is a function of both the cross- and alongshore coordinate, the FACR method cannot be used. Although the matrix problem is very large, it is block diagonal, very sparse, and symmetric. Iterative methods can be used to solve for η , in particular conjugate gradient (CG) methods. CG methods can be combined with multigrid methods [Wesseling, 1992] for increased speed, but are slower than FACR. For weak alongshore perturbations in bathymetry, iterative FACR methods can be used [e.g. Slinn *et al.*, 1999]. These are not yet implemented.

V.G Relaxing the Rigid Lid

Infragravity and swash processes where $\partial\eta/\partial t$ is order one are of interest in the nearshore. Such processes are filtered out with the rigid-lid approximation. A future project may be to remove the rigid-lid constraint and time-step the mass conservation equation

$$\frac{\partial\eta}{\partial t} + \delta_x[(\bar{h}^x + \bar{\eta}^x)u] + \delta_y[(\bar{h}^y + \bar{\eta}^y)v] = 0.$$

The onshore and offshore boundary conditions become rather complicated, and care must be taken not to generate and/or reflect waves at the boundaries. There are also a host of other numerical instabilities to consider.

V.H Future Model Development

- Allow for Arbitrary Topography with CG/Multigrid solver.

- **Curvilinear Coordinates:** The model only works now on rectangular domains. I would like generalize the coordinate system to curvilinear coordinates so that the model can be applied to curving shoreline.
- **Implement various nonlinear bottom stress parameterizations** [*Feddersen et al.*, 1999 - Chapter 3]
- **Allow for wave-current interaction.** The wave forcing is now given by a separate module that does not include refraction due to currents. The wave module should take into account current refraction and feedback into the circulation model. There are likely lots of interesting rip-current dynamics that could be investigated.

V.I Model Tests

Tests of the numerical model are described. The tests range from simple rotating channel flow, to reproducing numerical studies of shear waves on planar [ANH96] and barred beaches [*Slinn et al.*, 1999].

V.I.1 Rotating Channel Flow

Numerical and analytic solutions are compared for f -plane rotating channel flow with constant forcing and depth. The model parameters are $L^{(x)} = 1000$ km, $L^{(y)} = 2000$ km, $\Delta x = \Delta y = 100$ km. The Coriolis parameter $f = 10^{-4}\text{s}^{-1}$, the depth $h = 5000$ m, and $\mu = 0.3$ m/s. The alongchannel forcing $F^{(y)} = 10^{-4}$ m²/s² is spatially homogeneous everywhere, and the cross-channel forcing is zero. The model is spun up from rest. Linear alongchannel and cross-channel momentum balances are

$$hv_t = F^{(y)} - \mu v$$

and

$$fv = g\eta_x$$

with $u = 0$. The solution for v is

$$v = \frac{F^{(y)}}{\mu} [1 - e^{-\mu t/h}]$$

and the e -folding time-scale $h/\mu = 15,000$ s. The final steady solution is $v = 3.33 \times 10^{-4}$ m/s and $\eta_x = fv/g = 3.3979 \times 10^{-9}$.

Model Tests: AB2 time-stepping is used with $\Delta t = 1200$ s, and model runs were 3000 hours. The final equilibrated solutions ($v = 3.33 \times 10^{-4}$ m/s and $\eta_x = 3.3979 \times 10^{-9}$) agree very well with the analytic solutions, as does the spin-up rate, and the area integrated kinetic and potential energies.

Stability characteristics are investigated by varying both the forcing $F^{(y)}$ and friction μ . There are four nondimensional parameters that govern the stability of the numerical scheme. Since there are no analytic expressions for the maximum value of the stability parameters, they must be found via numerical experiment. The results for AB2 time-stepping are

$$\text{CFL} = \frac{\Delta t v}{\Delta x} < 0.24 \quad S_\mu = \mu \Delta t / h < 0.96$$

$$S_{bi} = \frac{\Delta t \nu}{(\Delta x)^4} < 1.2 \times 10^{-2} \quad R_{bi} = \frac{v(\Delta x)^3}{\nu} < 13.$$

These restrictions are not exact, but are general for use as guidelines for other modeling situations. The limits are slightly more restrictive with AB3 time-stepping,

$$\text{CFL} < 0.2 \quad S_{bi} < 0.8 \times 10^{-2}.$$

For nearshore modeling, the CFL and S_{bi} numbers are generally the most restrictive in limiting the size of the time step.

V.I.2 ANH96 Shear Waves Tests

Numerical results of ANH96 are reproduced to verify the model. ANH96 use a cross-shore domain $L^{(x)} = 1000$ m and alongshore domains of $L^{(y)} = 450$ m

and $L^{(y)} = 1350$ m, with $\Delta x = \Delta y = 5$ m, and $\nu = 10$ m⁴/s. The cross-shore bathymetry is planar with slope $\beta = 0.05$. The same parameters are used here except for a shorter cross-shore domain $L^{(x)} = 750$ m. The alongshore forcing is such that the base-state alongshore current has the form [ANH96]

$$V(x) = V_0 x^2 \exp(-x^3/\delta^3)$$

where V_0 and δ are set so that the maximum of $V = 1$ m/s at $x = 90$ m regardless of the value of μ . The model is run with $\Delta t = 0.5$ s to give a maximum CFL = 0.1. The requirement for $S_\mu = \mu \Delta t / h < 0.96$ is easily satisfied even near the shoreline where h is a minimum since μ is small. The biharmonic stability parameter $S_{bi} = 0.008$ which is very close to the maximum value for stability inferred from the earlier tests ($S_{bi} < 0.012$). The grid Reynolds number $R_{bi} = 12.5$. The model runs use both AB2 and AB3. The initial-condition is perturbed (as in ANH96) proportional to the most unstable shear wave streamfunction with maximum magnitude of 1 cm/s.

Single wavelength domain tests: Time series at various values of μ (Figure V.2) at a fixed cross-shore location are very similar to ANH96. The cross-shore variation of shear wave velocities (for $\mu = 0.0085$) are also very similar (not shown)

Multiple wavelength domain tests: The alongshore wavelength is extended to $L^{(y)} = 1350$ m, three times the wavelength of the most unstable mode (450 m). ANH96 observed transitions to longer wavelengths and lower frequencies as the shear waves evolved. Instead of applying an initial perturbation to the flow field, following ANH96 the forcing is perturbed by multiplying $F^{(y)}$ by

$$1 + \epsilon \sum_{j=1}^J b_j \cos(2\pi j y / L^{(y)})$$

where $\epsilon = 0.01$, $b_j = 1$, and $J = 3$. The perturbation in forcing is not proportional to the most unstable streamfunction, and other modes are excited in this case.

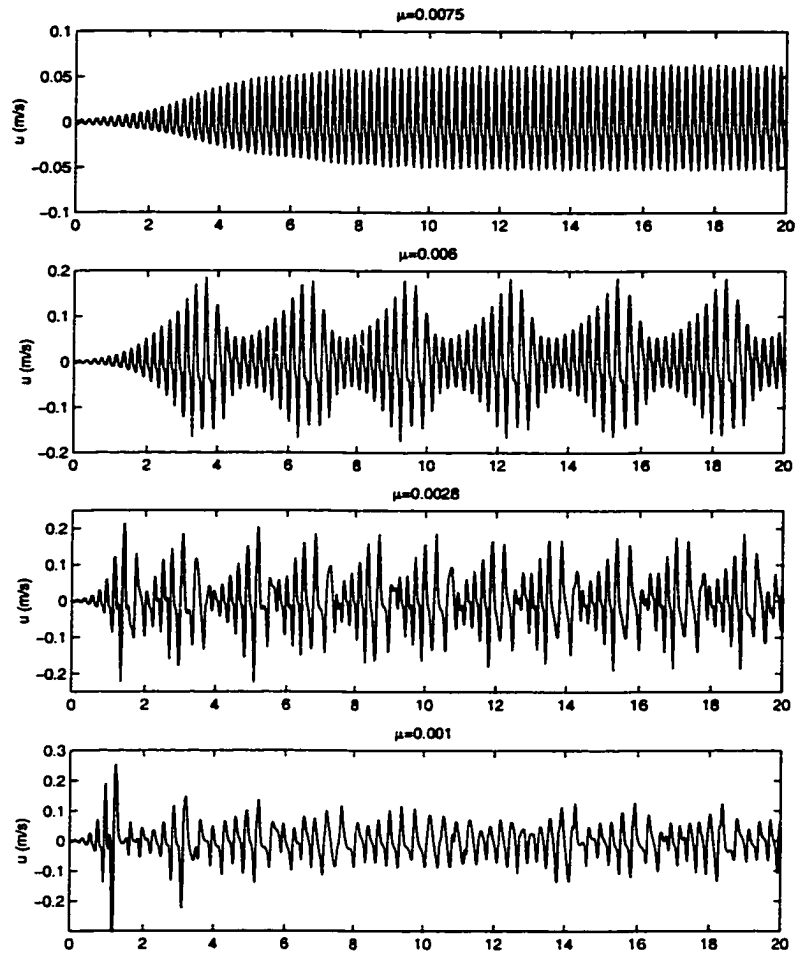


Figure V.2: Time series of cross-shore velocities at $x = 90$ m at different values of μ . Compare this with Figure 3 of ANH96.

The time series (Figure V.3) does show the transition to lower frequencies and wave numbers as observed by ANH96. This is also evident in the evolution of the vorticity field (Figure V.4).

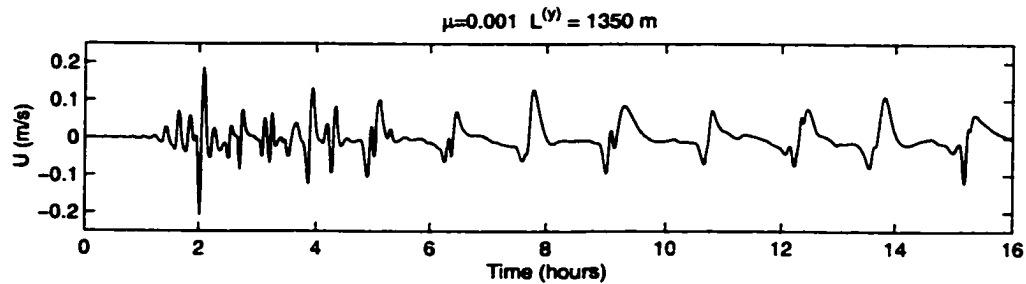


Figure V.3: Time series of u at $x = 90$ m, $\mu = 0.001$, and $L^{(y)} = 1350$ m. Compare to Figure 7, bottom panel of ANH96.

V.I.3 Slinn Tests

A barred beach result of *Slinn et al.* [1999] is reproduced. The grid size is $\Delta x = 2$ m, the domain size is $L^{(x)} = 512$ m and $L^{(y)} = 768$ m, $\Delta t = 0.1$ s, $\nu = 1.25$ m²/s giving $S_{bi} = 7.8 \times 10^{-3}$, and $\mu = 0.00546$ giving $S_{\mu} = 0.0088$ (easily stable). The maximum $v = 0.7$ m/s, giving $CFL = 0.035$ and $R_{bi} = 0.11$, both also easily stable. For this small grid size, S_{bi} is factor limiting the size of the time-step. The model run on the barred beach bathymetry reproduces the equilibrated shear wave case by *Slinn et al.* [1999] (Figure V.5). A 8-hour model run, took 22 hours of CPU time on a Sun Ultra 60.

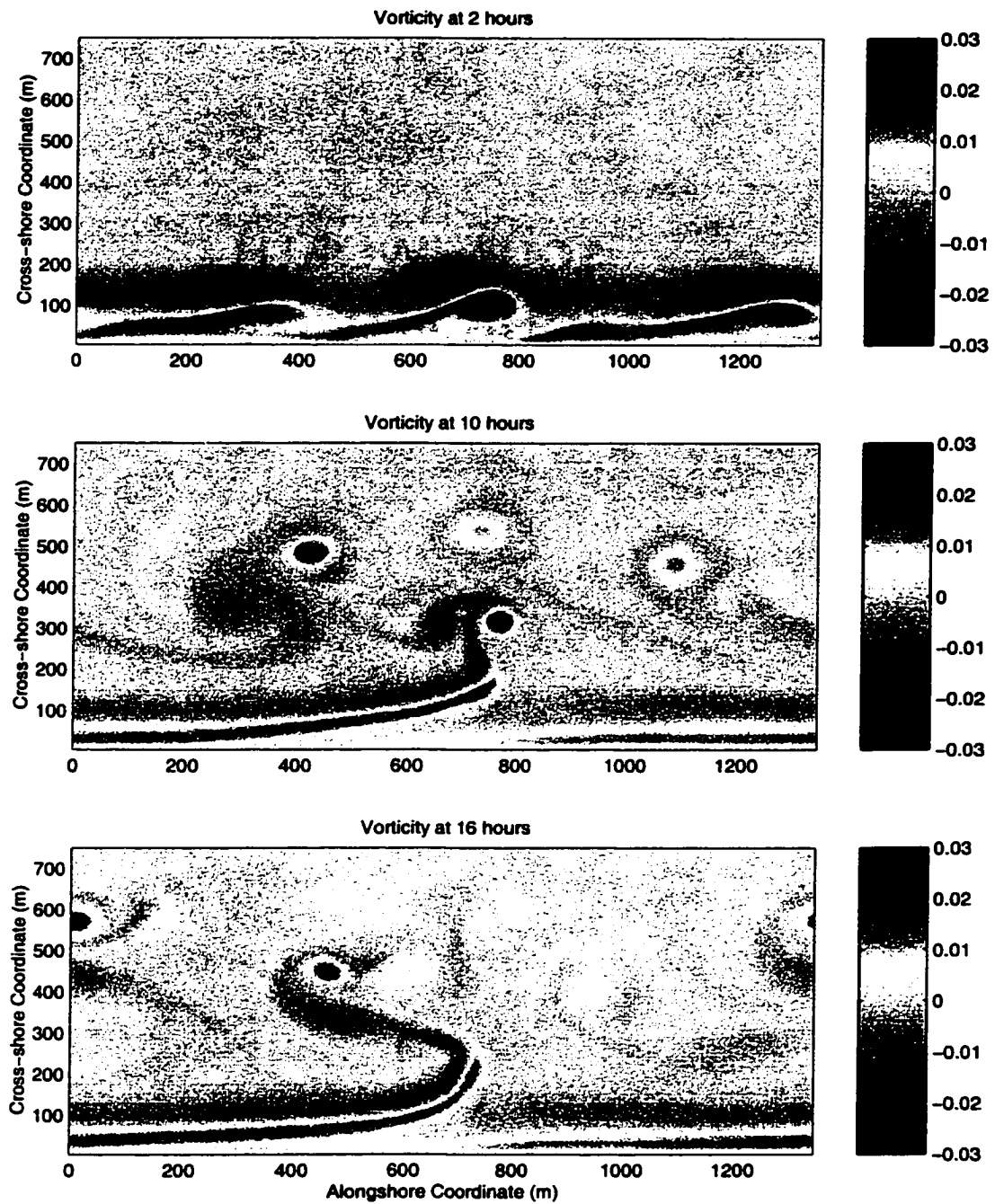


Figure V.4: Contour plots of vorticity at $t = 2$, $t = 10$, and $t = 16$ hours. The shoreline is at the bottom of each panel, and the alongshore current is maximum at approximately cross-shore coordinate 90 m.

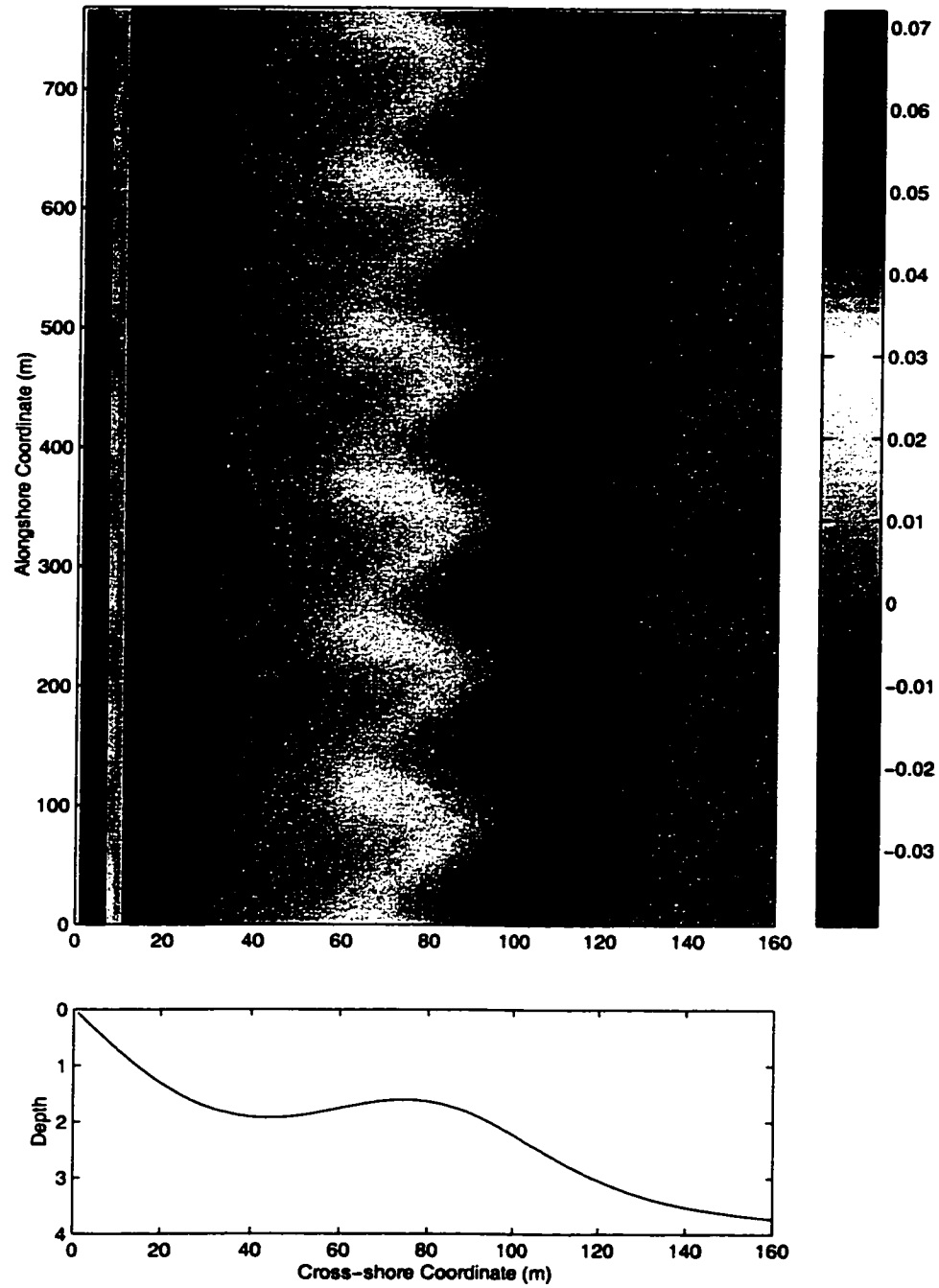


Figure V.5: Vorticity after 8 hours for barred beach bathymetry for the equilibrated shear wave case $\mu = 0.00546$. The region offshore of 160 m is not shown. Compare to Figure 7 first panel of *Slinn et al.* [1999].

V.J References

- Allen, J.S., P. A. Newberger, and R. A. Holman Nonlinear shear instabilities of alongshore currents on plane beaches. *J. Fluid Mech.* **310**, 181-213, 1996.
- Durrant, D.R., The 3rd-order Adams-Bashforth method - An attractive alternative to leapfrog time differencing. *Monthly Weather Rev.*, **119**, 702-720, 1991.
- Fedderson, F., Weakly nonlinear shear waves. *J. Fluid Mech.*, **372**, 71-91, 1998.
- Fedderson, F., R. T. Guza, S. Elgar, T. H. C. Herbers, Alongshore Bottom Stress Parameterizations., (in prep), 1999.
- Gresho, P. M. and R. L. Sani, On pressure boundary conditions for the incompressible Navier-Stokes equations, *Int. J. Num. Meth. Fluids*, **7**, 1111-1145, 1987.
- Harlow, F. and J. Welch, Numerical calculation of time-dependent viscous incompressible flow of fluid with free surfaces, *Phys. Fluids*, **8**, 2181-2189, 1965.
- Holland, W. R., The stability of ocean currents in eddy-resolving general circulation models, *J. Phys. Oceanogr.*, **8**, 363-392, 1978.
- Lilly, D. K., On the computational stability of numerical solutions of time dependent nonlinear geophysical fluid dynamics problems. *Mon. Wea. Rev.*, **93**, 11-26, 1965.
- Mellor, G. L., Users guide for a three-dimensional, primitive equation, numerical ocean model (June 1996 version), 38 pp., Prog. in Atmos. and Ocean. Sci, Princeton University, 1996.
- Mesinger, F., and A. Arakawa, *Numerical Methods Used in Atmospheric Models*, Vol 1, GARP Publ Ser. 17. World Meteorological Organization, 64 pp., 1976.
- Slinn, D. N., Allen, J. S., Newberger, P. A. and Holman, R. A., Nonlinear shear instabilities of alongshore currents over barred beaches, *J. Geophys. Res.*, **103**, 18,357-18,379, 1998.
- Slinn, D. N., Allen, J. S., Newberger, P. A. and Holman, R. A., Alongshore currents over variable beach topography, *J. Geophys. Res.*, (submitted), 1999.
- Wesseling, P., *An Introduction to Multigrid Methods*, Wiley, NY 284 pp., 1992.